A MULTI-WAVELENGTH STUDY OF DWARF GALAXIES WITH ACTIVE MASSIVE BLACK HOLES

by

Seth Jordan Kimbrell

A dissertation submitted in partial fulfillment
of the requirements for the degree

of

Doctor of Philosophy

in

Physics

MONTANA STATE UNIVERSITY
Bozeman, Montana

June 2023

DEDICATION

I dedicate this to Toothless, my feline companion who spent many a late night curled near me while I worked.

ACKNOWLEDGEMENTS

There are far too many people to thank for me to name them all, but I present a subset here.

My adviser, Dr. Amy Reines, for all of her support and guidance throughout graduate school, and for teaching me how to become an astronomer. My parents, James and Adrianne, for being wonderfully supportive of me and loving at all times. My wife, Faith, who has been by my side through the whole journey, and whose love I cherish. Jason and Dawn Geer, who made me feel at home in Montana. Paul Geer and Mia Van Vlack, for constant encouragement and friendship. Eric Adams, for teaching me that curiosity is its own reward. Judy Smith, for her excitement about science that set me on the road to becoming a scientist. And a tremendous group of friends who always celebrate every little step along the way with me. The work in this dissertation was financially supported by NASA through EPSCoR grant number 80NSSC20M0231 and by a fellowship from the Montana Space Grant Consortium. Support for Program number HST-GO-14251.004A was provided by NASA through a grant from the Space Telescope Science Institute, which is operated by the Association of Universities for Research in Astronomy, Incorporated, under NASA contract NAS5-26555.

TABLE OF CONTENTS

TABLE OF CONTENTS – CONTINUED

LIST OF TABLES

Table Page

LIST OF FIGURES

LIST OF FIGURES – CONTINUED

Figure Page

LIST OF FIGURES – CONTINUED

Figure Page

LIST OF FIGURES – CONTINUED

Figure Page

LIST OF FIGURES – CONTINUED

Figure Page

LIST OF FIGURES – CONTINUED

Figure Page

LIST OF FIGURES – CONTINUED

Figure Page

LIST OF FIGURES – CONTINUED

Figure Page

NOMENCLATURE

$M_\odot$	Solar Mass: 1.989×10^{30} kg
$L_\odot$	Solar Luminosity: 3.83×10^{33} erg/s

ABSTRACT

Dwarf galaxies which host massive black holes with $M \lesssim 10^6 M_\odot$ give us an opportunity to better understand the formation mechanism behind the supermassive black holes that live in the center of galaxies. Studying how common massive black holes in dwarfs are is an important step in constraining the channels that led to those supermassive black holes. An important part of that study is understanding in what types of dwarf galaxies we can expect to find massive black holes. I present a multi-wavelength study of dwarf galaxies which attempts to find any trends in the morphologies of the hosts of active massive black holes. I begin by modeling the structures of a sample of galaxies which have been identified as black hole hosts; I then perform an identical modeling on a sample of galaxies which show no signs of hosting a massive black hole. I finish by describing an X-ray search for massive black holes among irregular/disturbed galaxies, including the discovery of a very bright X-ray source which is extremely likely to be a massive black hole in a dwarf-dwarf merger. This is one of the first active massive black holes discovered in such a late-stage merger, and it is also notable for radiating at nearly its upper limit.

1

INTRODUCTION

It is well known that supermassive black holes (SMBHs) with masses $\geq 10^6 M_\odot$ live in the center of massive galaxies in our universe (Kormendy & Ho, 2013; Kormendy & Richstone, 1995). In recent years, it has become an established fact that dwarf galaxies with stellar masses $\lesssim 3 \times 10^9 M_\odot$ also host black holes (BHs) of proportionally lower mass. Dwarf hosts of active massive BHs - which I use to mean BHs which occupy the mass range between stellar mass BHs and SMBHs - are important to study, as they give us a chance to study BHs which have not grown much compared to SMBHs; in turn, this can help us better understand the formation mechanism behind the SMBHs we see in massive galaxies.

SMBHs are seen in the very early universe. For example, a quasar has been identified at a redshift of 7.085 with a luminosity of $6.3 \times 10^{13} L_\odot$; this corresponds to a BH with a mass of $\sim 2 \times 10^9 M_\odot$ merely 0.77 GYr after the Big Bang. How did such a massive black hole grow to that size so quickly? While stellar mass black holes (black holes with masses comparable to the mass of a star) are understood to be the result of stellar death in massive stars, SMBHs cannot have their formation explained so simply.

The birth mechanisms of SMBHs are an active area of research. Three of the most commonly discussed possible formation channels are presented in a simplified summary below and in Figure 1.1, but see Volonteri (2010); Volonteri et al. (2008) for more detailed reviews.

- A "direct collapse" model, in which pre-galactic discs of metal-poor gas (meaning gas made nearly exclusively of hydrogen and helium) experience conditions that prevent fragmentation of the gas. In this case, star formation can be quenched, and the cloud can ultimately collapse into high-mass (up to $10^5 M_\odot$) black hole seeds (Greene, 2012). This will be referred to as a "heavy seed" model.

- Population III stars - hypothesized stars which are nearly metal-free and have masses up to hundreds of solar masses - experience stellar death and form seed black holes of mass $\lesssim 100 M_{\odot}$.

- Stellar mass BHs form from the death of stars in high-redshift dense clusters. Seeds then form via mergers in these areas of high BH density (Antonini et al., 2019). This and the Population III star model will be referred to as a "light seed" model.

In any of the proposed formation mechanisms, SMBHs still must grow hierarchically via mergers and accretion - none of the proposed channels lead to the direct formation of BHs at the masses of observed SMBHs. Ideally, we would look into the very early universe and directly observe the "seeds" that grew into SMBHs in order to differentiate between these formation channels, but current technology does not allow us to do that (Volonteri & Reines, 2016; Vito et al., 2017). Instead, we turn to dwarf galaxies in the Local Universe.

Dwarf galaxies are often classified as galaxies with stellar masses roughly equal to or less than $10^{9.5} M_{\odot}$, a threshold which comes from the stellar mass of the Large Magellanic Cloud (LMC), one of the Milky Way's satellites (Reines et al., 2013; van der Marel et al., 2002). Dwarfs make up the majority of galaxies in the universe, and they come in a wide variety of morphologies (Kormendy, 2015; McConnachie, 2012). Until somewhat recently, only a small handful of dwarf galaxies were known to host massive BHs: Pox 52 (Barth et al., 2004), NGC 4395 (Filippenko & Ho, 2003) and Henize 2-10 (Reines et al., 2011). It was only in 2013 that Reines et al. (2013) conducted the very first systematic search for dwarfs hosting active massive black holes and identified 136 candidates using optical diagnostics, launching a new era of studies of dwarf galaxies hosting massive BHs.

Since structures in the universe are expected to have formed hierarchically through interactions and mergers (Conselice et al., 2009), these dwarfs are likely to have a quiet merger history, giving us the chance to study lower mass central BHs and their hosts which

have not been disrupted much compared to their more massive counterparts. Studies of BH scaling relations (e.g. Reines & Volonteri (2015)) suggest that dwarf galaxies, which occupy the low end of the galaxy mass range, host the lowest mass BHs. The occupation fraction of massive BHs in dwarf galaxies (i.e., the percentage of dwarf galaxies which host a massive BH) is expected to be a tracer of the dominant formation mechanism of SMBHs in the early universe (Volonteri et al., 2008). "Heavy" seed BHs are expected to be less common and lead to a lower BH population fraction in dwarf galaxies, while "light" seeds are expected to lead to a higher BH population fraction in dwarf galaxies.

One difficulty in searching for these massive BHs comes when trying to detect and observe them in the first place. Because massive BHs (and BHs in general) are not luminous objects, direct observation is incredibly difficult, and we must observe them by their effects on their surrounding environments. Instead of directly observing the BH, we most commonly observe an Active Galactic Nucleus (AGN), which is the luminous object at the center of galaxies. The AGN is a combination of the BH and its environment, and I show a simplified model of an AGN in Figure 1.2, pointing out where the emissions studied in this dissertation originate.

Any attempt to constrain the BH occupation fraction in dwarf galaxies must be cognizant of the morphologies and structures of its sample. For instance, Miller et al. (2015) performed an X-ray survey of early type dwarf galaxies and found a lower limit of $\sim 20\%$ on the BH occupation fraction. However, as this was only a study of one structural type of dwarf galaxy, we must be very careful when extrapolating to the general population of dwarfs. Dwarf galaxies have a wide range of morphologies, and it is very poorly understood what (if any) structural trends appear in AGN hosts. Do massive black holes appear preferentially in any particular type of dwarf galaxy? Without an answer to that question, the BH occupation fraction in dwarfs (and so the formation channels responsible for today's SMBHs) cannot be well constrained.

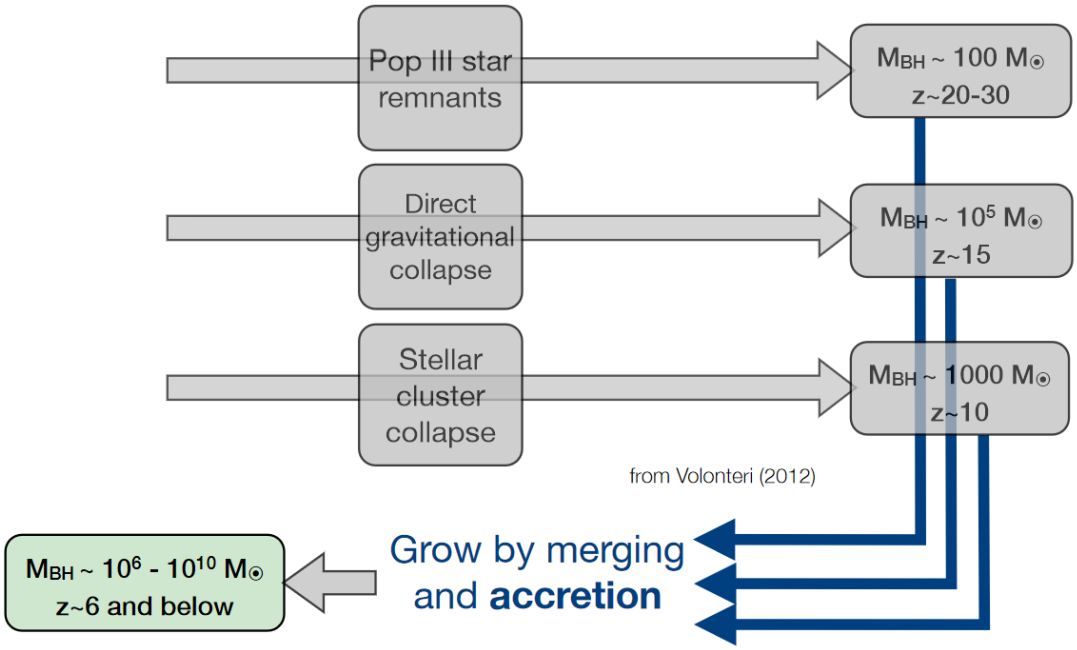

Figure 1.1: A simplified diagram of SMBH formation mechanisms. The formation channels are shown on the left, with the masses of the resulting "seed" black holes in the boxes on the right.
Credit: (Aird et al., 2015; Volonteri, 2012)

The primary focus of this dissertation is to use infrared imaging to study dwarfs which host active massive BHs and compare them to a sample of dwarfs which do not, in an effort to understand structural preferences in dwarf hosts of AGNs. I also show the results of an X-ray search for active massive BHs in a subsample of dwarf galaxies. In Chapter 2, I present Hubble Space Telescope (*HST*) imaging of a sample of dwarf galaxies which were selected as candidate AGN hosts by Reines et al. (2013). In that work, we performed a 2-dimensional bulge-disk decomposition of the galaxies and looked for trends in the parameters of the various structural components of each galaxy. We also placed a point source of light, which likely represents infrared emission from the AGN, in the center of each of the galaxies and measured the luminosities of each. This work was published in the Astrophysical Journal (Kimbrell et al., 2021).

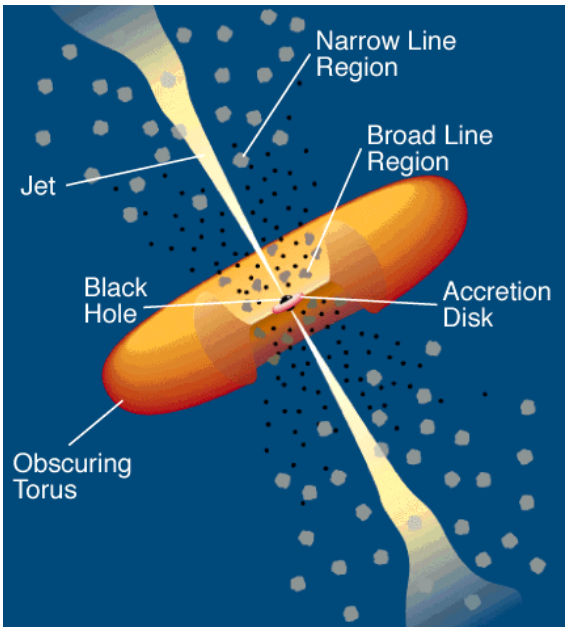

Figure 1.2: A simplified diagram of an AGN (not necessarily to scale). The accretion disk is the hot, bright disk of infalling matter. Infrared radiation mostly comes from the obscuring torus, which is the layer of dust and hot gas in a doughnut shape around the BH. X-ray emission comes from very close to the central BH. The broad and narrow line regions contain gas being ionized by the central BH and producing emission line spectra; the narrow lines are the lines used for optical diagnostics to select the sample in Chapter 2. The orbital velocity of the gas differentiates the broad line region (faster orbital velocity) from the narrow line region (slower orbital velocity).
Credit: C.M. Urry and P. Padovani
https://heasarc.gsfc.nasa.gov/docs/objects/agn/agn_model.html

In Chapter 3, I present a comparison between the Kimbrell et al. (2021) sample of dwarf AGN hosts and a sample of dwarf galaxies which do not show signs of hosting an AGN. In that work, we constructed a sample out of dwarf galaxies which are representative of the general population of dwarfs, and which span the same range of color, mass, and physical resolution as the Kimbrell et al. (2021) sample. We performed an identical bulge-disk decomposition on this sample in order to make a one-to-one comparison to the AGN hosts. This work has been submitted to the Astrophysical Journal and is currently under review.

In Chapter 4, I present X-ray imaging using the Chandra X-ray Observatory of a subset of the irregular/disturbed AGN hosts which could not be studied in Kimbrell et al. (2021). X-rays can help confirm/deny the presence of an AGN in a galaxy; this is especially useful for these irregular/disturbed galaxies, which can have star formation rates which overpower AGN emission in optical wavelengths. In this work, I present the detection of an AGN radiating at an Eddington ratio of ~ 0.81 in the dwarf-dwarf merger RGG66 - one of the first detections of its kind. This work is in the final stages of preparation and will be submitted to the Astrophysical Journal Letters.

Finally, in Chapter 5, I give a summary of the work done in this dissertation and give a look forward at the potential for further research in this area.

THE DIVERSE MORPHOLOGIES AND STRUCTURES OF DWARF GALAXIES HOSTING OPTICALLY-SELECTED ACTIVE MASSIVE BLACK HOLES

Contribution of Authors and Co-Authors

Manuscript in following chapter

Author: Seth Kimbrell

Contributions: Analyzed the data, wrote the first draft of the manuscript.

Author: Amy Reines

Contributions: Provided edits and comments on the manuscript, proposed for the data, advised on performing scientific analysis.

Author: Zachary Schutte

Contributions: Provided advice and guidance on using GALFIT on infrared data.

Author: Jenny Greene

Contributions: Provided scientific comments and edits on the manuscript.

Author: Marla Geha

Contributions: Provided scientific comments and edits on the manuscript. Provided data on the environment of a set of the galaxies.

Manuscript Information

Seth Kimbrell, Amy Reines, Zachary Schutte, Jenny Greene and Marla Geha

The Astrophysical Journal

Status of Manuscript:
____ Prepared for submission to a peer-reviewed journal
____ Officially submitted to a peer-reviewed journal
____ Accepted by a peer-reviewed journal
_X_ Published in a peer-reviewed journal

The Astrophysical Journal, Volume 911, Issue 2
DOI 10.3847/1538-4357/abec40

Introduction

It is well established that massive galaxies host supermassive black holes (BHs) with masses of $M_{\rm BH} \sim 10^6 - 10^{10} M_\odot$ at their centers (Kormendy & Ho 2013; Kormendy & Richstone 1995). Our own Milky Way hosts Sagittarius A*, a BH with a mass of $4 \times 10^6 M_\odot$ (Ghez et al., 2008). Much work has gone into studying structural properties, scaling relations, and the possible coevolution of massive galaxies and the BHs they host (see e.g., the review by Kormendy & Ho 2013). The presence and properties of dwarf galaxies ($M_\star \lesssim 10^{9.5} M_\odot$) hosting massive BHs is not nearly as well studied (see Reines & Comastri 2016; Greene et al. 2019 for reviews), with the first systematic search for these objects performed by Reines et al. (2013).

Lower mass BHs in dwarf galaxies provide a chance to put constraints on BH "seed" masses and probe their possible formation channels (see e.g., Volonteri 2010 and Greene 2012). Mortlock et al. (2011) report observations of a luminous ($6.3 \times 10^{13} L_\odot$) quasar, hosting a $\sim 2 \times 10^9 M_\odot$ BH at a redshift of z=7.085 (corresponding to 0.77 Gyr after the Big Bang). This suggests that the first BH seeds were born in the very early Universe and at least some grew to enormous masses extremely fast. Since we cannot directly observe the small BH seeds at high redshift with current telescopes (Volonteri & Reines 2016; Vito et al. 2017), dwarf galaxies in the low-redshift Universe are our best chance to study BHs that have not grown much compared to the BHs in today's massive galaxies (Habouzit et al. 2017; Anglés-Alcázar et al. 2017).

In most cases, BHs in dwarf galaxies must be detected as active galactic nuclei (AGN) through radiative signatures, rather than through stellar or gas dynamics (although see Nguyen et al. 2019) since the gravitational sphere of influence of a low-mass BH in a dwarf galaxy is too small to be resolved at distances greater than 4-5 Mpc with current facilities. The first systematic search for AGNs in dwarf galaxies was performed by Reines et al. (2013)

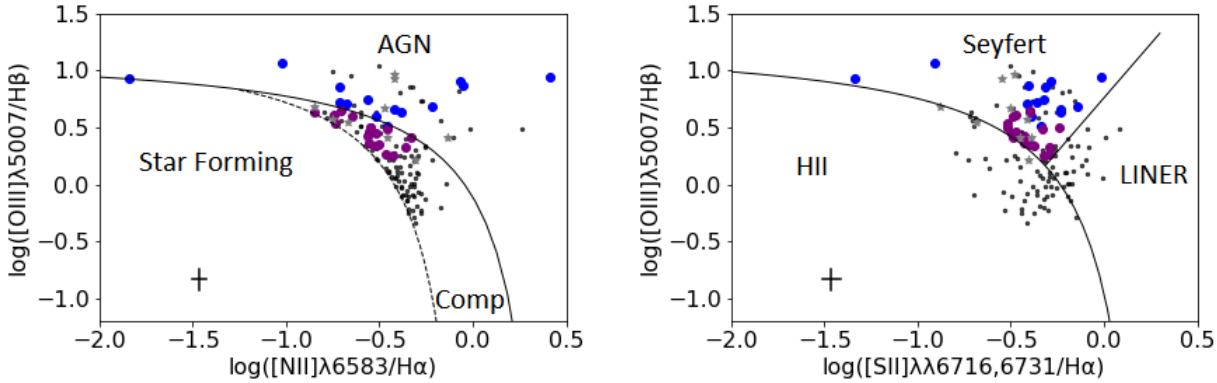

Figure 2.1: Narrow emission line diagnostic diagrams showing the location of our sample of dwarf galaxies, which exhibit optical signatures of active massive BHs (Reines et al., 2013). Blue and purple points indicate AGNs and Composites, respectively, with new *HST* observations presented here. Grey stars indicate additional galaxies we include in this work from the Reines et al. (2013) sample with *HST* imaging previously presented in Schutte et al. (2019), Baldassare et al. (2017) and Jiang et al. (2011). Black dots indicate the remaining galaxies in the Reines et al. (2013) sample. Left: [OIII]/Hβ vs. [NII]/Hα diagnostic diagram. The solid line shows the "maximum starburst" line from stellar photoionization models (Kewley et al., 2001). The dashed line is an empirical separation between galaxies that show some contribution from AGN and galaxies dominated by star formation (Kauffmann et al., 2003). Composite galaxies fall between the dashed and solid lines, and likely indicate contributions from both an AGN and star formation. Right: [OIII]/Hβ vs. [SII]/Hα diagnostic diagram, using the classifications from Kewley et al. (2006). Typical errors are shown in the lower left corners.

using optical spectroscopy from the Sloan Digital Sky Survey (SDSS). They identified 136 dwarf galaxies with narrow emission line ratios indicating the presence of an AGN, some of which also had broad Hα emission that was used to estimate BH masses by employing standard viral techniques (e.g., Greene & Ho, 2005). However, as dwarf galaxies have relatively small sizes, very little is known about the detailed morphologies and structures of the host galaxies from ground-based imaging.

In this work, we present *Hubble Space Telescope (HST)* imaging of a subset of the Reines et al. (2013) sample. We aim to characterize the structural components of dwarf galaxies hosting active massive BHs and better understand what galactic properties (if any)

contribute to or influence the presence of AGNs in dwarf galaxies. We describe our sample of dwarf galaxies and *HST* observations in Sections 2 and 3, respectively. Our structural analysis of the galaxy images is presented in Section 4 and our results are given in Section 5. We present a discussion in Section 6, and end with concluding remarks in Section 7. We adopt a Hubble constant of $H_0 = 73$ km s^{-1} Mpc^{-1} throughout this work, and we report magnitudes in the ST system.

Sample of Dwarf Galaxies

The dwarf galaxies with optically-selected AGNs studied here are a subset of objects identified by Reines et al. (2013). Starting with a sample of $\sim 25,000$ emission line galaxies with stellar masses $M_\star \leq 3 \times 10^9 M_\odot$ in the NASA-Sloan Atlas (NSA), Reines et al. (2013) analyzed Sloan Digital Sky Survey (SDSS) spectra of these objects and found 136 dwarf galaxies exhibiting optical signatures of accreting massive BHs. These galaxies fall in either the AGN or Composite region of the [OIII]/Hβ vs. [NII]/Hα narrow emission line diagnostic diagram (i.e., the BPT diagram; Baldwin et al. (1981); Kewley et al. (2001)). Our target galaxies were also selected to be in the Seyfert region of the [OIII]/Hβ vs. [SII]/Hα narrow emission line diagnostic diagram, making them among the strongest cases of dwarf galaxies hosting massive BHs. However, it is worth noting that low-metallicity AGNs and low-metallicity starbursts both fall in the upper left region of the BPT diagram and are therefore difficult to distinguish (i.e., RGG 5, the leftmost point in Figure 2.1; also see the discussion in Section 6.3).

We proposed for *HST* SNAP observations of 61 dwarf galaxies meeting the criteria above and 33 were ultimately observed for this program. Of these, 13 galaxies were classified as AGNs by Reines et al. (2013) and 20 were classified as Composites. Two of these galaxies, RGG 20 and RGG 118, are broad-line AGNs with virial BH masses of $M_{\rm BH} \sim 10^{6.1} M_\odot$ (Reines et al., 2013) and $M_{\rm BH} \sim 10^{4.7} M_\odot$ (Baldassare et al., 2015), respectively.

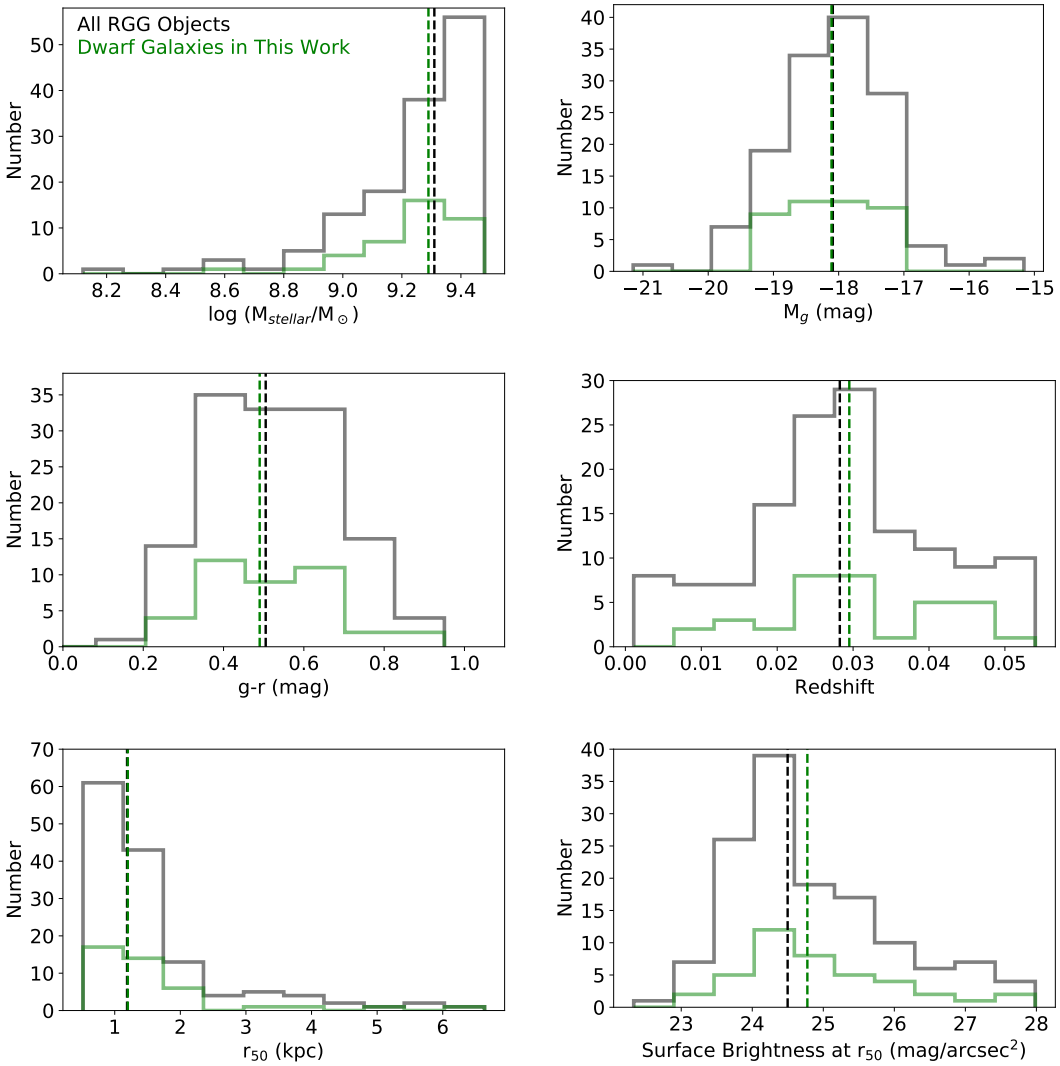

Figure 2.2: Distribution of stellar mass, absolute g-band magnitude, $g-r$ color, redshift, Petrosian half-light radius and interpolated g-band surface brightness at the Petrosian half-light radius for the galaxies in this work (green histograms). Properties of the entire Reines et al. (2013) (RGG) sample are shown as gray histograms. Dashed lines indicate median values.

BH mass estimates for the narrow-line objects are in the range of $M_{\rm BH} \sim 10^{4.9} - 10^{5.8} M_\odot$ based on the AGN scaling relation between BH mass and total galaxy stellar mass from Reines & Volonteri (2015). Total stellar masses from the NSA are in the range $M_\star \sim$

$10^{8.5} - 10^{9.5} M_{\odot}$, and come from the `kcorrect` code of Blanton & Roweis (2007).

We also include 7 additional dwarf galaxies with broad-line AGNs and Composites from Reines et al. (2013) that have *HST* observations from another program (PI: Reines, Proposal ID 13943). Virial BH masses for these objects are in the range $M_{\rm BH} \sim 10^{4.9} - 10^{6.1} M_{\odot}$ (Reines et al., 2013) and these AGNs have been confirmed with *Chandra* X-ray observations (Baldassare et al., 2017). The *HST* near-IR data are analyzed by Schutte et al. (2019), who also give an updated BH-bulge mass relation including dwarf galaxies. Here we include the galaxy structural information presented in Schutte et al. (2019). We also include 1 additional broad-line object (RGG 123) from Reines et al. (2013) that has *HST* observations and structural analysis presented in Jiang et al. (2011), bringing our total sample to 41 BH-hosting dwarf galaxies with high quality *HST* images.

Figure 2.1 shows narrow-line diagnostic diagrams with locations of our sample galaxies using the line measurements in Reines et al. (2013). Figure 2.2 shows the stellar masses, absolute magnitudes, colors, redshifts, half-light radii and g-band surface brightnesses of our galaxies compared to the entire Reines et al. (2013) sample, which illustrates that we have a representative sample of the RGG galaxies in this work. In order to have uniform surface brightness measurements, we use data from the NSA giving surface brightnesses at discrete radii and use a spline interpolation to estimate the surface brightness at the Petrosian half-light radius for all the galaxies in the RGG sample, including the ones analyzed in this work. Table 2.1 lists our sample of dwarf galaxies and their properties.

Table 2.1. Sample of 41 Dwarf Galaxies Hosting Optically-Selected AGNs with *HST* Observations

RGG ID	NSAID	SDSS Name	z	$g-r$ color	M_g	log M_*
(1)	(2)	(3)	(4)	(5)	(6)	(7)
AGNs						
RGG 1[a]	62996	J024656.39−003304.8	0.0462	0.81	−17.99	9.5
RGG 2	7480	J024825.26−002541.4	0.0247	0.58	−17.32	9.1
RGG 4	64339	J081145.29+232825.7	0.0157	0.36	−17.98	9.0
RGG 5	46677	J082334.84+031315.6	0.0098	−0.29	−18.85	8.5
RGG 6	105376	J084025.54+181858.9	0.0150	0.59	−17.61	9.3
RGG 7	30020	J084204.92+403934.5	0.0293	0.62	−17.45	9.3
RGG 9[a]	10779	J090613.75+561015.5	0.0469	0.40	−18.98	9.3
RGG 10	106134	J092129.98+213139.3	0.0313	0.58	−18.20	9.3
RGG 11[a]	125318	J095418.15+471725.1	0.0328	0.44	−18.73	9.2
RGG 15	27397	J110912.37+612347.0	0.0068	0.36	−17.33	8.9
RGG 16	30370	J111319.23+044425.1	0.0265	0.49	−17.98	9.3
RGG 20	52675	J122342.82+581446.4	0.0144	0.66	−18.11	9.5
RGG 22	77431	J130434.92+075505.0	0.0480	0.45	−18.77	9.0
RGG 26	54572	J134939.36+420241.4	0.0411	0.47	−18.55	9.3
RGG 28	70907	J140510.39+114616.9	0.0174	0.42	−18.13	9.4
RGG 29	71023	J141208.47+102953.8	0.0326	0.42	−17.74	9.1
RGG 32[a]	15235	J144012.70+024743.5	0.0295	0.31	−19.18	9.3

Table 2.1 (cont'd)

RGG ID (1)	NSAID (2)	SDSS Name (3)	z (4)	$g-r$ color (5)	M_g (6)	log M_* (7)
Composites						
RGG 37	6059	J010005.93−011058.8	0.0514	0.59	−18.76	9.3
RGG 40	82616	J074829.21+510052.4	0.0190	0.38	−17.89	9.1
RGG 48[a]	47066	J085125.81+393541.7	0.0411	0.28	−19.19	9.1
RGG 50	47918	J090737.05+352828.4	0.0276	0.53	−18.53	9.4
RGG 53	105953	J091720.88+191018.9	0.0285	0.87	−17.17	9.3
RGG 56	26850	J093239.45+511542.9	0.0473	0.38	−18.99	9.2
RGG 58	39968	J093821.54+063130.8	0.0224	0.48	−18.05	9.4
RGG 59	39954	J094705.72+050159.8	0.0242	0.47	−17.73	9.2
RGG 64	106991	J100423.33+231323.4	0.0266	0.49	−17.53	9.1
RGG 66	55081	J101747.09+393207.7	0.0540	0.51	−18.92	9.0
RGG 67	12623	J102149.12+635206.8	0.0211	0.62	−16.99	9.0
RGG 69	117416	J102833.33+184513.9	0.0274	0.58	−17.98	9.5
RGG 79	19138	J112957.62+653804.8	0.0439	0.56	−18.21	9.5
RGG 81	93958	J113129.20+350958.9	0.0337	0.95	−17.24	9.3
RGG 86	66343	J115359.06+130853.6	0.0226	0.67	−17.59	9.3
RGG 88	52494	J115812.53+575322.1	0.0415	0.50	−18.18	9.3
RGG 89	32762	J115922.33+511809.2	0.0297	0.78	−17.32	9.3
RGG 94	161692	J122505.40+051945.9	0.0066	0.67	−17.27	9.3
RGG 118[b]	166155	J152303.80+114546.0	0.0243	0.37	−18.38	9.4
RGG 119[a]	79874	J152637.36+065941.6	0.0382	0.25	−18.65	9.4
RGG 123[c]	18913	J153425.58+040806.6	0.0395	0.35	−18.16	9.1
RGG 127[a]	99052	J160531.84+174826.1	0.0317	0.61	−17.46	9.4

Table 2.1 (cont'd)

RGG ID	NSAID	SDSS Name	z	$g-r$ color	M_g	log M_*
(1)	(2)	(3)	(4)	(5)	(6)	(7)
RGG 135	4308	J173202.96+595855.0	0.0291	0.39	−18.91	9.4
RGG 136	5563	J235609.14−002428.6	0.0256	0.31	−18.68	9.2

Note. — Column 1: identification number given in Reines et al. (2013). Column 2: NSA identification number. Column 3: SDSS name. Column 4: redshift. Column 5: $g-r$ color from the NSA. Column 6: Absolute g-band magnitude from the NSA. Column 7: Log total stellar mass from the NSA in units of $M_\odot$. Italicized RGG IDs indicate broad-line AGNs, for which the virial mass has been determined using broad Hα emission (Reines et al. 2013; Baldassare et al. 2015 for RGG 118).

[a]Structural analysis adopted from Schutte et al. (2019). [b]Structural analysis adopted from Baldassare et al. (2017). [c]Structural analysis adopted from Jiang et al. (2011).

Hubble Space Telescope Observations

HST near-infrared images of the 33 dwarf galaxies observed for our SNAP program were obtained with the Wide Field Camera 3 (WFC3) between 2015 October 11 and 2017 June 18 (PI Reines; Proposal ID 14251). The observations were taken in the IR/F110W filter (wide YJ-band) with a central wavelength of 1.15 μm.

Snapshot observations of each galaxy were taken with a total on-source exposure time of $\sim$ 16 minutes. We utilized a four-point sub-pixel dither pattern and used a 512×512 pixel subarray to avoid buffer dumps. The subarray has a field of view of $65.5'' \times 65.5''$ and all of our galaxies fall well within the array.

The images were processed by the STScI data reduction pipeline using the AstroDrizzle routine. The final cleaned, combined and calibrated images have an angular resolution of $\sim 0\farcs13$ (FWHM), corresponding to a range in physical scales of $\sim 17 - 131$ pc, and a scale of ~ 70 pc at the median distance of our sample (111 Mpc).

Analysis

The primary goal of this work is to characterize the structures of dwarf galaxies hosting optically-selected AGNs. For galaxies with regular morphologies, our general approach is to model each galaxy with a PSF plus either one or two Sérsic components for the galaxy light. For the galaxies requiring two Sérsic components, these structures can be ascribed to an inner bulge/pseudobulge component plus an outer disk component. In general, we do not attempt to model more complex structures, such as spiral arms or tidal features, although we include bars in a few cases. In dwarf galaxies, these features tend to be very faint and difficult to model, despite being fairly obvious to the eye. In the subsections below, we describe the details of our modeling and analysis.

Six of our galaxies are irregular in shape and fitting these galaxy images with

axisymmetric models proved impractical. We present the dwarf irregular galaxies in Section 5.

PSF Construction

It is important to use an accurate PSF to model the detector response to a point source, given that these galaxies are selected as AGN hosts. A PSF which does not properly capture that response can lead to inaccurate modeling of the galaxy as a whole.

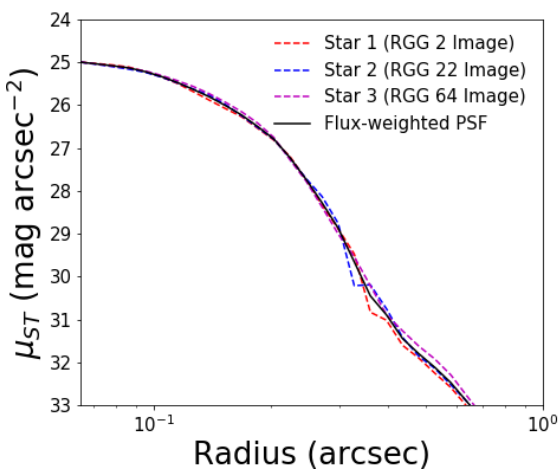

Figure 2.3: Radial intensity profiles for the bright central stars in RGG 2, RGG 22 and RGG 64, as well as the flux weighted average PSF.

We used stars in our images to create PSFs. Since the response of a detector to a point source is dependent on location on the detector, we selected images with a bright star within 100 pixels of the center of the galaxy. Three stars met this criterion (one each in the images of RGG 2, RGG 22 and RGG 64).

We took a cutout of these stars and performed a flux-weighted average to create one image. We then made a model of the resulting image, giving us a PSF that is the result of averaging individual stars, while having the high signal-to-noise ratio required of PSFs. The

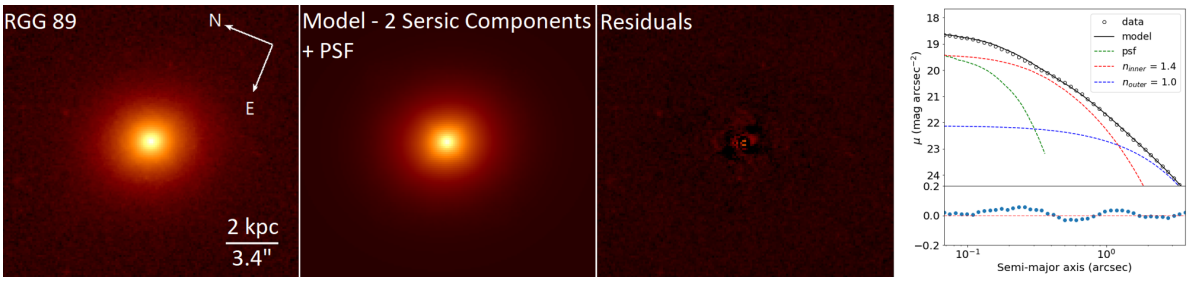

Figure 2.4: Left three panels: *HST*/WFC3 F110W image of RGG 89, GALFIT model, and the residuals after subtracting the model from the image. Images are shown on a stretched log scale to show faint details in the residuals. Right: Surface brightness profiles. The data are shown as black circles and the model is shown as a black line. The individual model components are shown as colored dashed lines. The residuals are shown in the bottom panel.

PSF we created, as well as the profiles of each of the three stars, can be seen in Figure 2.3. We used this PSF for all of our modeling.

Galaxy Modeling

We fit two-dimensional surface brightness models to our images using the galaxy fitting software GALFIT (Peng et al., 2010). GALFIT has many analytical models which can be used to fit galaxies. For this work, we used the very general Sérsic profile, which takes the form (Sérsic, 1963):

$$\Sigma(r) = \Sigma_e \times \exp\left[-\kappa\left(\left(\frac{r}{r_e}\right)^{\frac{1}{n}} - 1\right)\right] \tag{2.1}$$

where r_e is the effective radius defined such that half of the flux lies within r_e, and Σ_e is the surface brightness at r_e. The parameter n, which is coupled to κ, is the Sérsic index; a higher Sérsic index indicates a steep inner brightness profile and more extended wings, while a lower index indicates a shallower profile at small radius and less extended wings. κ is a free parameter defined as $\kappa = \Gamma(2n)/2$, where Γ is the complete gamma function. The case of $n = 4$ is the de Vaucouleurs profile, often used to model classical bulges (de

Vaucouleurs, 1948). Values of $n = 1$ and $n = 0.5$ describe exponential disks and Gaussian profiles, respectively.

Our galaxy fitting process followed that recommended by Peng et al. (2010). Before running GALFIT, we first created mask files containing the pixel coordinates of prominent foreground and background objects we wished to ignore during the modeling process. We then began by using a single Sérsic component only.

We found that, in every case, a single Sérsic component was a poor fit and left very bright residuals. However, this gave us a rough estimate for some basic properties such as size and axis ratio of a given galaxy. We then added a central PSF to the single Sérsic model, using the results of the previous fit as our starting parameters. This PSF could represent the AGN and/or an unresolved nuclear star cluster (see §6).

We then attempted to model each galaxy with two Sérsic components without a central point source. We let the Sérsic component of the inner component vary, while holding the Sérsic index of the outer component fixed at the canonical value for an exponential disk of $n = 1$. This again gave us some basic information about the bulge/disk model (e.g., relative sizes) but it rarely resulted in a good fit. We then added a point source to the two-Sérsic model.

For three of the galaxies in our SNAP program, RGG 7, RGG 29 and RGG 37, a bar was necessary. This was determined through visual inspection of the data, in which the residuals showed a bright bar through the center of the galaxy that was missed by our basic model. RGG 127 also required a bar (Schutte et al., 2019).

In general, when GALFIT found a best-fit model, we re-fit the galaxy several times while varying the starting parameters to ensure that the software was not just falling into a local minimum of goodness of fit.

Model Selection

Next we determined whether each galaxy was best fit by one Sérsic component or two Sérsic components (with one being an exponential disk), plus a PSF. To decide this, we followed the example of Oh et al. (2017) and used a three-step model selection process. First, we eliminated the two Sérsic model if the effective radius of the exponential disk was smaller than the effective radius of the inner component. Next, we eliminated the two Sérsic model if the disk was subdominant everywhere in the radial profile. Finally, we used the Akaike Information Criterion (AIC) (Akaike, 1974). Assuming normally distributed noise, the AIC is calculated from χ^2 as:

$$\mathrm{AIC} = \chi^2 + 2k \tag{2.2}$$

where k is the number of free parameters in a model. Following Oh et al. (2017), we eliminated the two Sérsic model if adding more parameters did not reduce the AIC by ≥ 10. We report the results in §5.

We note that the faintest features we modeled reach a surface brightness of ~ 25 mag/arcsec^2. It is possible that, for some of the least luminous galaxies in our sample, *HST* could fail to detect features fainter than this in the diffuse outer regions of the galaxy. This could have an impact on the modeling procedure and model selection described above.

Testing PSF Necessity

We also tested whether the point sources are necessary components in our models, given that some are subdominant to the galactic components (e.g. RGG 69). We used the AIC as our first criterion; as in §4, we rejected the model including a PSF if it does not reduce the AIC by ≥ 10. Using this criterion, all of the galaxies we modeled prefered the inclusion of a PSF.

As additional checks on the necessity of the PSFs, we also examined the Sérsic indices

of the inner components and the residuals. Kormendy & Ho (2013) set an upper bound for the Sérsic index of dwarf ellipticals at n $\lesssim$ 4, and bounds for pseudobulges and classical bulges at n $\lesssim$ 2 and n $\gtrsim$ 2, respectively. Other studies performing *HST* photometry of dwarf galaxies and low-mass AGN hosts (e.g. Jiang et al. 2011; Schutte et al. 2019; Graham & Guzmán 2003) find (pseudo)bulges and dwarf ellipticals with n $\leq$ 4. Therefore, we were skeptical of models without a PSF if they led to an inner Sérsic index much larger than this (i.e., n $\geq$ 5).

Finally, we visually examined the residuals after subtracting the GALFIT model from the data. A Sérsic component attempting to account for a missing PSF leads to telltale rings in the residuals, alternating bright and dark, in the center of the galaxy. Therefore, we also rejected models without PSFs if they led to these rings.

To summarize, of the 26 regular galaxies modeled in our SNAP sample, all 26 preferred the model which includes a PSF based on the AIC. In addition, 9 have Sérsic indices n $\geq$ 5 when a PSF is not included, and 21 have rings in the residuals when a PSF is not included (some have both a high Sérsic index and rings in the residuals). Only 3 out of the 26 galaxies (RGG 2, RGG 59 and RGG 88) preferred the PSF model solely based on the AIC. While the presence of a point source is less certain in these three galaxies, we nevertheless adopted the PSF model for consistency with the rest of the sample.

Uncertainty Calculation

Uncertainties in the GALFIT parameters were found following the example of Baldassare et al. (2017). Magnitudes are most sensitive to changes in the sky background, while effective radii and Sérsic indices are most sensitive to the point spread function. Using sigma clipping, we iteratively subtracted points that were 3σ above the median of each full image to estimate a sky background and, once GALFIT converged on fit parameters for a model, we replaced the fit sky background with the estimated one. We used the change in magnitudes

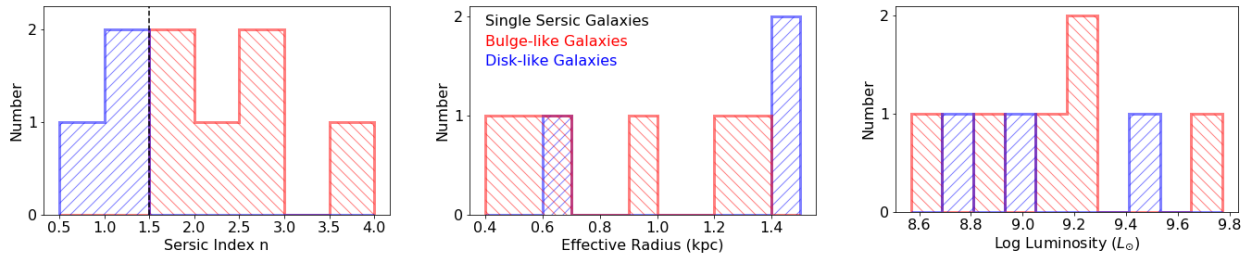

Figure 2.5: Left: Distribution of the Sérsic indices for the one-Sérsic galaxies in our sample. A vertical dashed line shows the cutoff between disk-like galaxies and (pseudo)bulge-like galaxies. Disk-like galaxies are shown in blue histograms, while (pseudo)bulge-like galaxies are shown in red histograms. Middle: Distribution of the effective radii (in kpc), with the same color scheme as the left. Right: Distribution of the luminosities (in WFC3/IR F110W; 1.15μm), with the same color scheme as the left.

as our error. To determine the uncertainty in effective radii and Sérsic index, we replaced the PSF constructed from averaging three central stars with one constructed from a single bright central star. The changes in effective radius and Sérsic index were used as our error.

Surface Brightness Profiles

Using the *isophote* Python package, we fit elliptical isophotes to the data and our GALFIT models. With these isophotes, we constructed 1-D surface brightness profiles. We used these 1-D profiles as additional checks on our models. Figure 2.4 shows an example of a GALFIT model and surface brightness profile for the dwarf galaxy RGG 89. Similar plots for the other galaxies in our sample are shown in the Appendix. The images are stretched on a log scale to show very faint details. While there are features in the residuals for some of the galaxies, they are quite dim and will not significantly affect our results. Typically, the residuals are $\lesssim 0.1$ mag arcsec^{-2}.

Results

Of the 41 AGN-hosting dwarf galaxies in our sample, the vast majority (35/41 = 85%) have fairly regular morphologies and can be adequately modeled in GALFIT using one or two Sérsic components plus a PSF, and sometimes a bar (§5). A smaller, but non-negligible, fraction of the dwarf galaxies in our sample (6/41 = 15%) have irregular/disturbed morphologies and were not successfully modeled in GALFIT. These galaxies are presented in §5.

Dwarf Galaxies With Regular Morphologies

We have determined whether a single Sérsic or two Sérsic model is a better fit for the regular galaxies in our sample (including the galaxies taken from the literature as described in §2 and noted in Table 1). A PSF component is required in all cases to account for the central AGN light and possibly an unresolved nuclear star cluster. The GALFIT results are summarized in the Appendix in Table 2.2. An example *HST* image, model fit and surface brightness profile is shown in Figure 2.4. Corresponding figures for the other galaxies with regular morphologies can be found in the Appendix here (or see Schutte et al. 2019, Baldassare et al. 2017, Jiang et al. 2011.)

We find that 74% (26/35) of the regular galaxies in our sample are best fit by a two-component Sérsic model where we ascribe the outer component to a disk with fixed $n = 1$. The other 26% (9/35) of the regular galaxies in our sample are best fit with a single Sérsic model.

For these single Sérsic galaxies, we distinguish between (pseudo)bulge/elliptical galaxies and disk-like galaxies using the Sérsic index; galaxies with $n \geq 1.5$ are designated (pseudo)bulges/ellipticals, while galaxies with $n < 1.5$ are disk-like (see Figure 2.5).

Disk Properties The galaxies in our sample tend to be disk-dominated. For the galaxies best fit with two Sérsic components, the median bulge-to-total (B/T) ratio (with PSF subtracted) is $< B/T >= 0.21$ with a range of $B/T \sim 0.04 - 0.88$. Figure 2.6 shows the distribution of B/T ratios. Galaxies modeled with a single Sérsic component consistent with a (pseudo)bulge are shown in Figure 2.6 as having a B/T ratio of 1, and single Sérsic galaxies consistent with a disk have $B/T = 0$. Luminosities of individual components were calculated from the apparent magnitudes reported by GALFIT and the distance to each galaxy. The half-light radii of the disks in our sample span a range of $r_{\rm e,disk} \sim 0.7 - 6.5$ kpc, with a median of $r_{\rm e,disk} \sim 2.2$ kpc. The left column of Figure 2.7 shows the distributions of $r_{\rm e,disk}$ and $L_{\rm disk}$.

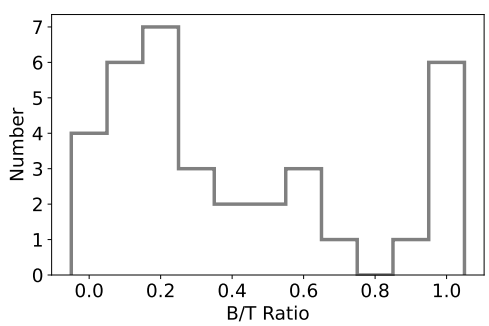

Figure 2.6: Distribution of bulge-to-total light ratios for all the galaxies in our sample (one-Sérsic and two-Sérsic galaxies). A B/T of 0 indicates a disk-like single-Sérsic galaxy, while a B/T ratio of 1.0 indicates a (pseudo)bulge single-Sérsic galaxy.

In addition to the 26 galaxies which have a disk and a (pseudo)bulge, 3 additional galaxies (RGG 7, 29 and 123) are best modeled with a single Sérsic component and appear to be disks without detectable (pseudo)bulges. However, it should be noted that RGG 7 and RGG 29 each have a bar in addition to the disk component, and RGG 7 also has spiral structure in the disk, which we do not model. There is also a bright point source at the center of these galaxies and it is possible we could have missed a very small bulge component

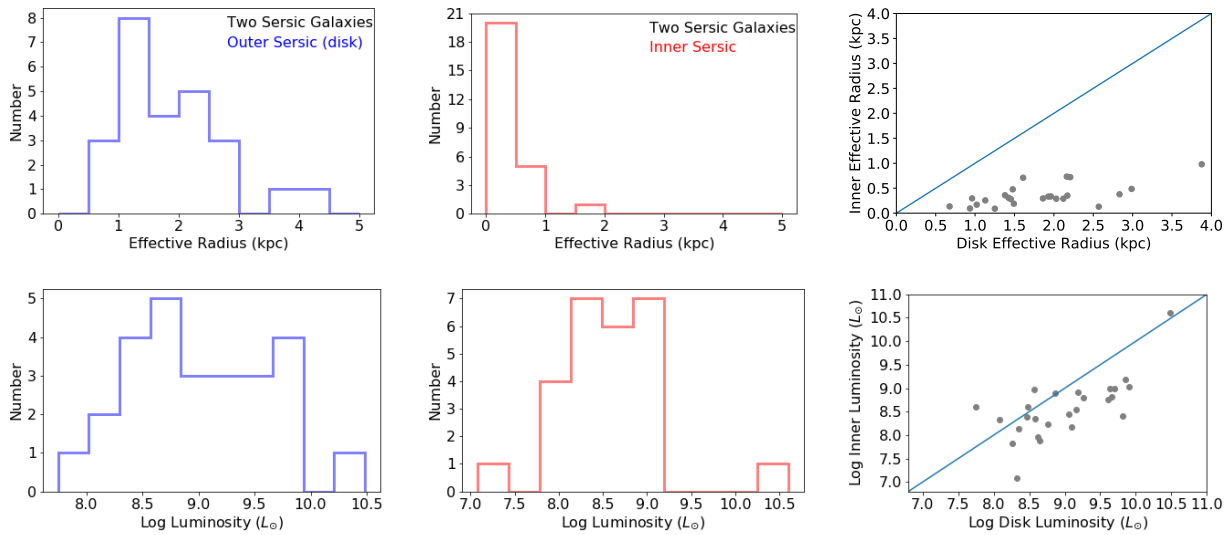

Figure 2.7: Disk and (pseudo)bulge properties determined from GALFIT, for galaxies best fit with two Sérsic components. Left column from top to bottom: Disk effective radii (in kpc) and luminosities (in WFC3/IR F110W; 1.15μm). RGG 118, which has a disk effective radius of 6.5 kpc, is not shown in the left top panel. RGG 118 and RGG 123 are not included in the luminosity distribution in the lower left panel as the *HST* observations were taken in the WFC3/IR F160W and WFPC2 F814W filters, respectively. Middle column: Same as left column but for the inner Sérsic. Right column: (Pseudo)bulge versus disk properties for individual galaxies, along with the one-to-one line for comparison. Typical errors in the radii and luminosities are smaller than the points (see §2 for discussion of error calculation and Table 2.2 for reported errors).

(or nuclear star cluster), even with *HST* resolution.

Additionally, RGG 15 is notable for being completely dominated by the disk at all radii except for the central PSF (see Figure 2.14 in Appendix), although we do detect a small and faint inner Sérsic component with $n = 0.5$. The half-light radius of the inner component is only $\sim$ 0.3 kpc, compared to $\sim$ 2 kpc for the disk. The inner component is also 3.5 magnitudes fainter than the disk of this galaxy.

<u>(Pseudo)bulge Properties</u> Given the importance of BH-to-bulge scaling relations (see, e.g., Kormendy & Ho 2013), it is vital to determine if our galaxies possess some kind of

(pseudo)bulge component. In our sample of dwarf galaxies, we aim to distinguish between pseudobulges and classical bulges. Structurally, pseudobulges have more of an exponential profile than classical bulges, somewhat resembling an inner disk. The Sérsic index acts as an effective selector of pseudobulges versus classical bulges - pseudobulges have Sérsic indices $n \lesssim 2$ (see e.g., Fisher & Drory 2008; Kormendy & Kennicutt 2004 for more on the differences between pseudobulges and classical bulges).

Based on above criterion, 21 of the 26 regular galaxies best fit with two Sérsic components have an inner component consistent with a (pseudo)bulge, while 5 host a more classical bulge.

When including the 6 single Sérsic galaxies that are consistent with being bulge-like, the total number of galaxies hosting a (pseudo)bulge comes to 32/41 (78%). Despite most of our galaxies hosting some kind of (pseudo)bulge component, Figure 2.6 shows that they tend to be disk-dominated (§5).

The Sérsic indices of the inner/(pseudo)bulge components for the two-Sérsic galaxies are in the range of $n_{\rm bulge} \sim 0.3 - 4.0$, with a median of $< n_{\rm bulge} >= 1.3$ (see Figure 2.8). The single Sérsic galaxies that are bulge-like have relatively large Sérsic indices compared to the inner components of galaxies best fit by a (pseudo)bulge–disk decomposition.

The inner/(pseudo)bulge components in our dwarf galaxy sample tend to be quite compact. The half-light radii are in the range $r_{\rm e,bulge} \sim 0.1 - 1.6$ kpc, with a median of $< r_{\rm e,bulge} >\sim 0.3$ kpc. The most compact galaxy overall in our sample is RGG 29, a galaxy best fit with a single Sérsic component with $n = 1.4$ and $r_{\rm e} \sim 0.5$ kpc.

The middle column of Figure 2.7 shows the distributions of $r_{\rm e,bulge}$ and $L_{\rm bulge}$.

The angular diameters ($2r_{\rm e,bulge}$) of the (pseudo)bulges in our sample are shown in Figure 2.8. The median value is $1\farcs2$ and the range in angular diameter is $0\farcs1$ - $6\farcs5$. This illustrates that *HST* resolution is essential to disentangle and detect small (pseudo)bulges in dwarf galaxies even at low redshift ($z \lesssim 0.05$).

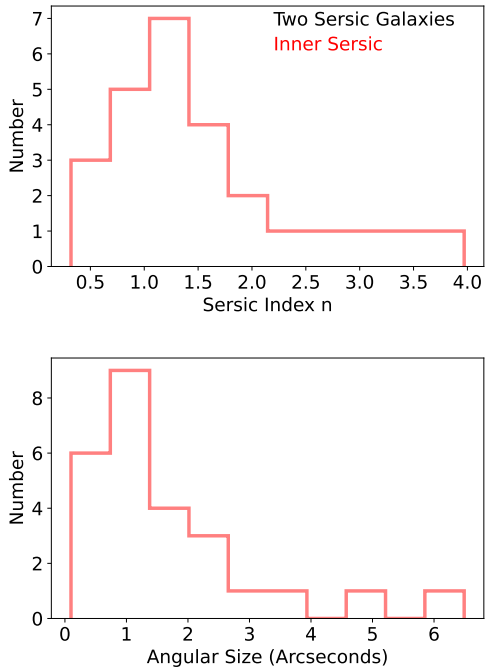

Figure 2.8: Top: distribution of the Sérsic indices for the (pseudo)bulge components of our two-Sérsic galaxies. Bottom: distribution of the angular diameters of (pseudo)bulge components. We do not show the distribution of disk Sérsic indices since they are fixed to $n = 1$.

Irregular/Disturbed Dwarf Galaxies

Of the 41 dwarf galaxies in our sample, 6 (15%) have irregular/disturbed morphologies and were not successfully modeled in GALFIT (RGG 5, 40, 53, 66, 135 and 136). The *HST* galaxy images are shown in Figure 2.9. RGG 5, 40 and 136 do not have obvious photometric centers and resemble Magellanic-type dwarf irregulars. RGG 66 and 135 show signs of interactions/mergers, with RGG 135 displaying very elongated tidal tails. The remaining galaxy, RGG 53, looks more regular at first glance. However, a spiraled interior appears in the residuals when attempting to model the system in GALFIT. These galaxies are reminiscent of the dwarf galaxies found to host radio-selected AGNs by Reines et al. (2020), some of which host "wandering" (i.e., non-nuclear) BHs.

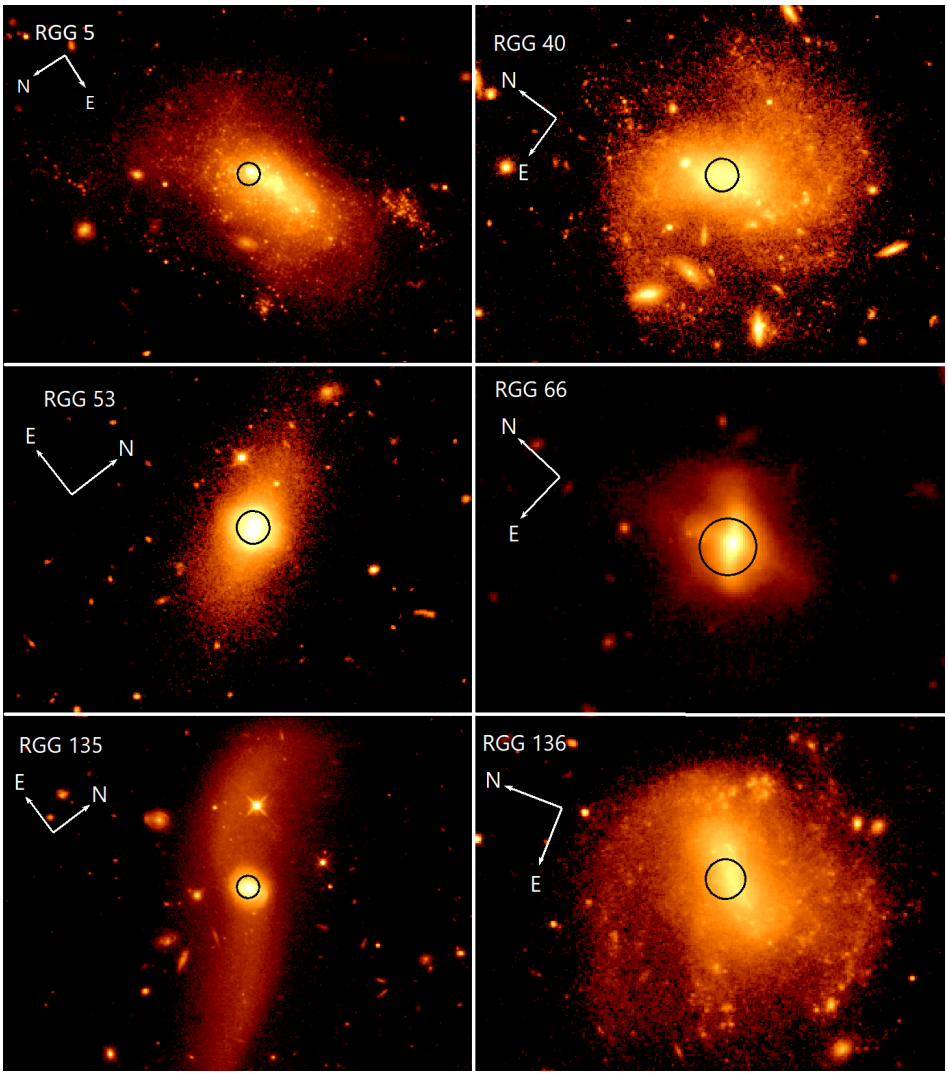

Figure 2.9: *HST* observations of the dwarf irregular galaxies in our sample shown on a log scale. Black circles indicate the locations of the SDSS spectroscopic fibers, which are 3″ in diameter. Fiber positions were retrieved from the NASA Sloan Atlas (NSA). While no astrometric corrections have been applied to the *HST* images, we checked that our astrometry is consistent with the Hubble Legacy Archive.

With the exception of RGG 5, the irregular/disturbed dwarf galaxies all fall in the composite region of the [OIII]/Hβ vs. [NII]/Hα narrow-line diagnostic diagram. RGG 5 falls in the AGN part of the diagram just above the maximum starburst line; however, it is difficult to reliably distinguish between AGN and star-formation in this low-metallicity

region of the diagram (Groves et al., 2006). All of the galaxies were also selected to fall in the Seyfert region of the [OIII]/Hβ vs. [SII]/Hα diagram (see §2). Follow-up X-ray observations would help confirm if these irregular/disturbed dwarf galaxies do indeed host AGNs.

Figure 2.10 shows the distribution of physical resolutions probed at the distances of our galaxies. The irregulars tend to be relatively nearby. It is possible that AGNs in dwarf irregular galaxies are particularly difficult to identify at greater distances through optical selection since more star-formation related emission can be included in the spectroscopic aperture. Indeed, Dickey et al. (2019) obtained Keck data of dwarf galaxies in the SDSS and found some to be classified as AGN with higher resolution data.

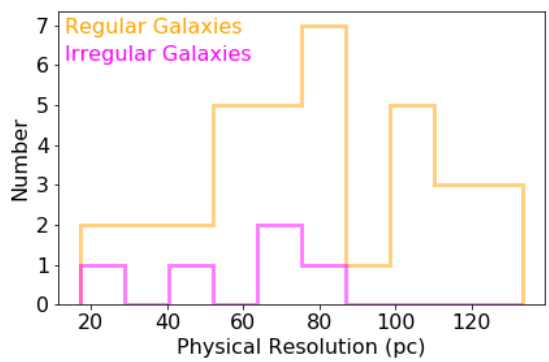

Figure 2.10: Distribution of the physical resolution at the various distances of the galaxies in this work, with *HST* angular resolution (FWHM) of 0.″13. Regular galaxies are shown in orange histograms, while irregular galaxies are shown in magenta histograms.

Discussion

Comparison to Jiang et al. (2011)

Using *HST* observations, Jiang et al. (2011) studied the structures of 147 galaxies hosting low-mass BHs from the sample of Greene & Ho (2007). The objects in the Greene & Ho (2007) sample were selected as broad-line AGNs in the SDSS with virial BH masses

$M_{\rm BH} \lesssim 2 \times 10^6\ M_\odot$. The hosts are sub-$L_\star$ galaxies, yet they are more luminous and massive than the dwarfs studied here.

In some ways, our results are similar to those of Jiang et al. (2011). For example, most of their sample is dominated by disk galaxies with small bulge components. Our median B/T ratio of 0.21 ± 0.03 is comparable to the median B/T ratio of 0.18 reported by Jiang et al. (2011). They also found that the vast majority of these bulges were likely to be pseudobulges, rather than classical bulges, which is in agreement with our results. Jiang et al. (2011) report 70% of their modeled (pseudo)bulge components have a Sérsic index $n < 2$, and we find $\sim 81\%$ of our modeled (pseudo)bulges have a Sérsic index $n < 2$.

There are also notable differences between our sample of dwarf galaxies and the sample studied by Jiang et al. (2011). First, we see a very small fraction ($\sim 11\%$) of galaxies with bars. In contrast, Jiang et al. (2011) report a bar in $\sim 39\%$ of their sample. It has been postulated (e.g., Shlosman et al., 1989) that bars play a role in funneling gas to the centers of galaxies and feeding AGN. Our sample suggests there must be more at play than just bars. This same conclusion was reached by Jiang et al. (2011); despite their sample having a significant bar fraction, the fraction was still too low to suggest that bars alone feed AGN. Finally, in contrast with Jiang et al. (2011), we find dwarf irregular galaxies in our sample (§5).

Nature of the Point Sources: Nuclear Star Clusters and/or AGNs?

Here we consider the physical origin of the PSFs used in our models. Are the unresolved point sources dominated by the AGNs in the galaxies, or nuclear star clusters (NSCs)? The dwarf galaxies in our sample were selected to have optical signatures of AGNs (Reines et al., 2013), and $\sim 80\%$ of galaxies in this stellar mass range ($M_\star \sim 10^{8.5} - 10^{9.5} M_\odot$) are known to host NSCs (e.g., see Figure 3 in the review by Neumayer et al. 2020). Indeed, AGNs and NSCs are known to co-exist in many galaxies (Seth et al., 2008).

Both types of objects would appear as point sources in our *HST* WFC3 F110W images. The angular resolution is $0\farcs13$, corresponding to a physical resolution of $\sim$ 70 pc at the median distance of our sample. Even in the nearest modeled galaxy in our sample (RGG 94, with a redshift of 0.0066), a point source corresponds to a physical size of $\lesssim$ 17 pc. NSCs tend to have radii $\lesssim$ 10-15 pc (Geha et al., 2002; Neumayer et al., 2020), and therefore an NSC would likely appear as an unresolved source of light for all galaxies in our sample. Of course, continuum emission from AGNs would also be unresolved on these scales.

The F110W luminosities of the PSFs in our SNAP sample range from $10^{39.6}$ to $10^{42.1}$ erg s^{-1}, with a median of $< L_{\rm PSF} >= 10^{41.1}$ erg s^{-1}. We estimate the expected NSC luminosity in each galaxy using the scaling between galaxy stellar mass and NSC mass given by Neumayer et al. (2020):

$$\log\ M_{\rm NSC} = 0.48 \times \log\left(\frac{M_*}{10^9 M_\odot}\right) + 6.51 \tag{2.3}$$

Galaxy stellar masses are adopted from the NSA and given in Table 1. We estimate the F110W luminosity given the predicted NSC mass with Starbust99 models for the continuum (Leitherer et al., 1999), assuming an instantaneous burst and a metallicity of 0.008 as appropriate for these dwarfs (Reines et al., 2013).

We show the measured PSF luminosities in our galaxies versus the predicted luminosities for stellar populations (i.e., NSCs) of three different ages in Figure 2.11. The two older ages, 900 Myr and 100 Myr, are typical of NSCs (Neumayer et al., 2020), while 10 Myr would be an abnormally young age for an NSC. However, we include the 10 Myr model because the most luminous observed PSFs are $\sim 10 - 100\times$ the predicted NSC luminosity unless we assume such a young cluster. This may suggest these simple stellar population models do not adequately represent NSCs, or that there is another contribution to the unresolved source of light (such as the AGN), at least for the most luminous PSFs. It is also possible

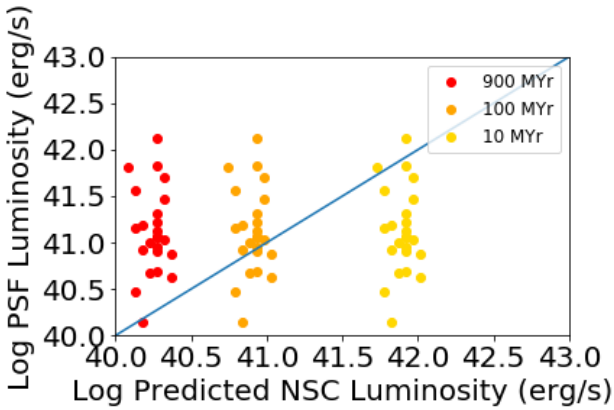

Figure 2.11: Central PSF luminosity for dwarf galaxies in our SNAP sample versus predicted NSC luminosity for various stellar population ages (see §6). The blue line shows the one-to-one relation.

that the scaling relation between NSC mass and stellar mass may be bimodal (as discussed in Ordenes-Briceño et al. 2018), rather than the relation in Equation 2.3.

Naively, we would not expect to detect continuum emission from the narrow-line AGNs in our SNAP sample, since the lack of detectable broad-line emission suggests that the nuclei are obscured. However, a nucleus could be unobscured, with the broad-line emission falling below the detection limit in the Reines et al. (2013) study. This scenario is exemplified by RGG 118, in which broad Hα emission was not firmly detected in the SDSS spectrum, but was detected in follow up data with higher sensitivity and spectral resolution (Baldassare et al., 2015). It is also possible that the obscuring material is clumpy, keeping some sight lines to the nucleus open that could contribute to the continuum we are observing. Additionally, continuum emission via scattered light has been observed from obscured nuclei (Zakamska et al., 2005), which could be contributing to our point sources. There could also be some contribution at 1.1 μm from very hot dust.

Selection Effects

We note that our sample of AGN-hosting dwarf galaxies is not complete. The dwarf galaxies studied here were selected to have optical spectroscopic indications of an AGN (Reines et al., 2013). There are other ways to identify active BHs in dwarf galaxies - e.g., radio (Reines et al., 2011, 2014, 2020), X-ray (Lemons et al., 2015; Birchall et al., 2020), AGN variability (Baldassare et al., 2020), and the host properties can be quite different depending on the BH selection method (e.g., Reines et al., 2020).

As discussed in Reines et al. (2013), optical diagnostics are only sensitive to actively accreting BHs in galaxies with relatively low star formation. Even if accreting at the Eddington limit, lower-mass BHs are not very luminous, leading to a selection bias towards dwarf galaxies hosting highly accreting BHs and/or more massive BHs. Emission lines from an AGN can also be hidden by host galaxy light even without significant star formation (Moran et al., 2002). Moreover, low-metallicity AGNs overlap with low-metallicity starbursts in the upper-left region of the BPT diagram (e.g., Groves et al., 2006; Yang et al., 2017). This will lead to a bias against actively star-forming dwarf galaxies, despite possibly hosting a massive BH (Reines et al., 2011; Riffel, 2020; Birchall et al., 2020; Baldassare et al., 2020). The $3''$- diameter SDSS fibers are three times the median angular effective diameter of the (pseudo)bulge components of our galaxies (median $2r_{e,\mathrm{bulge}} = 1''$); therefore only galaxies which are AGN dominant and have bright, well-defined centers will be selected via SDSS spectroscopy (Reines et al., 2013).

In addition, many dwarf galaxies are simply too faint to be targeted for spectroscopy in the SDSS and even if they are, there is no guarantee the fiber placement coincides with a potential AGN. Instead, the spectroscopic fiber may be centered on a bright star forming region, and/or the BH may not reside in the nucleus (Reines et al., 2020). Therefore, while the Reines et al. (2013) sample is likely highly incomplete, the galaxies studied here are representative of that optically-selected sample of AGNs in dwarf galaxies (Figure 2.2).

Environmental Effects on Galaxy Morphologies

It has been observed that the environment around a galaxy plays a role in the morphology of the galaxy. Galaxies which are in less dense environments tend to be diskier, while galaxies in a more tightly packed environment tend to be rounder and more bulge-like (see, e.g. Rong et al. 2020).

For 28 of the dwarf galaxies in this work, the distance to the nearest massive host galaxy has been measured using the 2MASS Extended Source Catalog and taking redshifts from SDSS spectroscopy and several other sources (Geha et al., 2012). The remaining galaxies fall within one degree of the edge of the SDSS footprint, and so the environment was not analyzed. The nearest massive host galaxy was chosen to be the nearest galaxy with $M_{K_s} < -23$, and dwarfs were considered to be "isolated" by Geha et al. (2012) if the nearest massive host is more than 1.5 Mpc away. This is a conservative estimate of whether a galaxy is isolated or not; many galaxies less than 1.5 Mpc away from a more massive galaxy are still isolated, as they are often separated by many virial radii.

We show the B/T ratio plotted against the distance to the nearest host (DHOST) for the galaxies with environment data in Figure 2.12. We find that the majority of dwarfs in our sample do not meet the criterion to be considered isolated, but we do not find a correlation between whether the bulge or disk dominates and the isolation of the galaxy. For our sample, it may be difficult to disentangle the effects of hosting an AGN from the effects of the environment.

Conclusions

We have presented a study of 41 dwarf galaxies hosting optically-selected massive BHs (Reines et al., 2013) using *HST* near-infrared observations. In this first paper, we examine the morphologies and structural components of the host galaxies using the galaxy image fitting

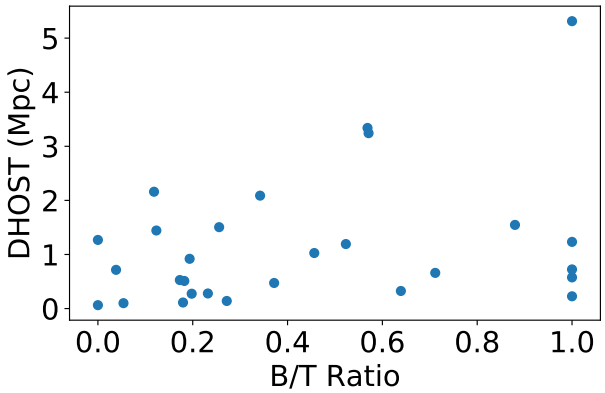

Figure 2.12: Distance from the dwarf galaxy to the nearest massive host versus the measured bulge to total light ratio.

software GALFIT (Peng et al., 2010). We will compare these AGN-hosting dwarf galaxies to the general population of dwarf galaxies in a forthcoming paper. The main results of this work are summarized below:

1. The majority of the dwarf galaxies in our sample (85%) have regular morphologies, although there is a non-negligible fraction (15%) of irregular/disturbed galaxies in our sample (see Figure 2.9).

2. We perform 2D bulge-disk decompositions for the regular galaxies and find that the majority are disk-dominated with small pseudobulges. The median bulge-to-total light ratio is $< B/T >= 0.21$.

3. Our sample also includes three dwarf disk galaxies without detectable bulges and six pure bulge/elliptical galaxies.

4. The best-fit models for the regular dwarf galaxies include a central point source of light. The point sources are consistent with originating from nuclear star clusters and/or AGNs.

5. Of the irregular/disturbed galaxies, three appear to be Magellanic-type dwarf irregulars and two exhibit obvious tidal features indicative of interactions/mergers.

We have shown that optically-selected BH-hosting dwarf galaxies exhibit a variety of morphologies and structures. This has important implications for constraining the BH occupation fraction at low mass, which is a key diagnostic for discriminating between BH seeding mechanisms (e.g., Volonteri, 2010; Greene et al., 2019). While there have been valiant efforts to constrain the BH occupation fraction in low mass galaxies (Miller et al., 2015), studies that only focus on a particular type of dwarf galaxy (e.g., early-types) may well miss the bulk of the population.

Appendix

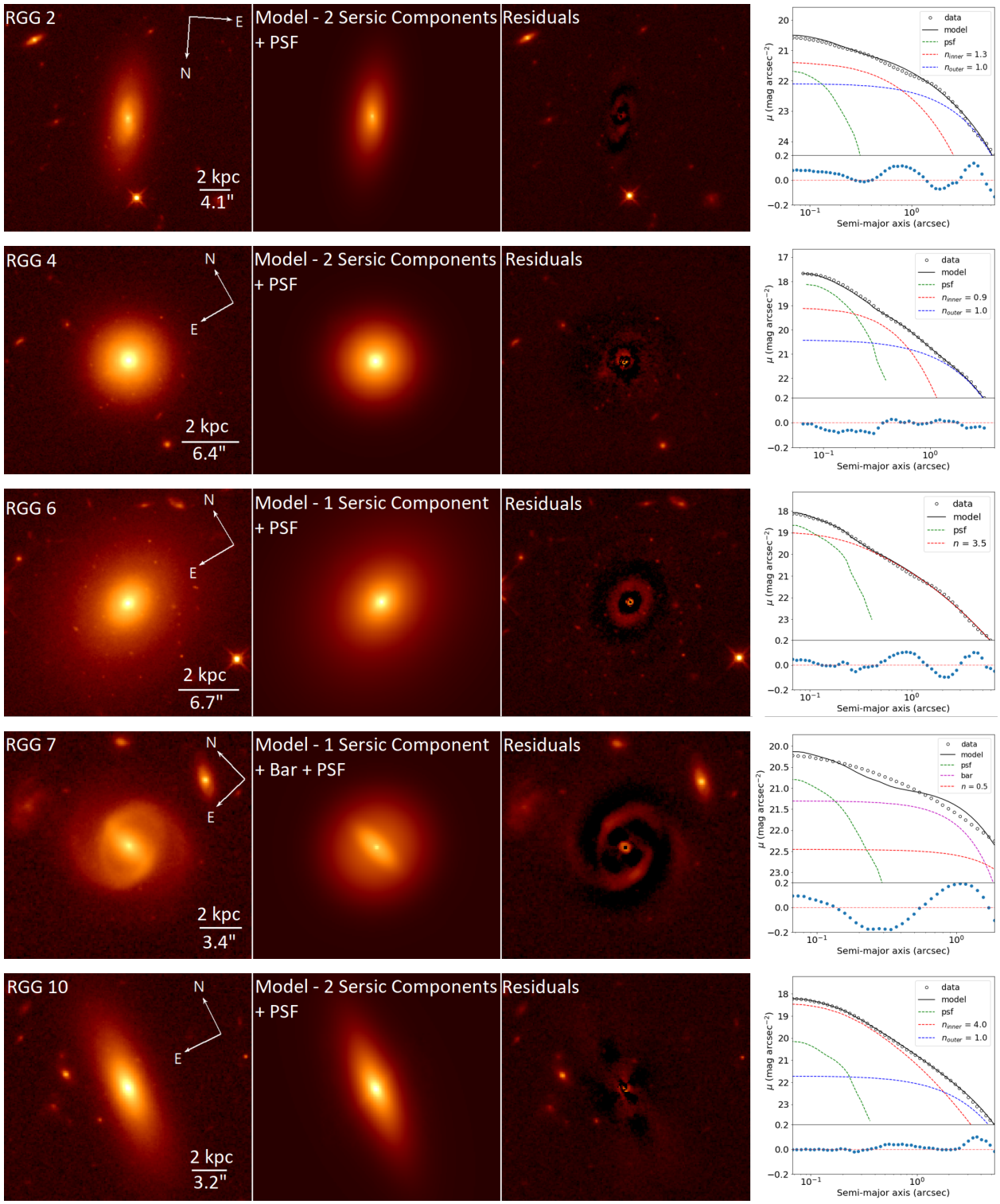

Figure 2.13: Left three panels: *HST* image, GALFIT model, and the residuals after subtracting the model from the image. Images are shown on a stretched log scale to show faint details in the residuals. Right: Surface brightness profiles. The data are shown as black circles and the model is shown as a black line. The individual model components are shown as colored dashed lines. The residuals are shown in the bottom panel.

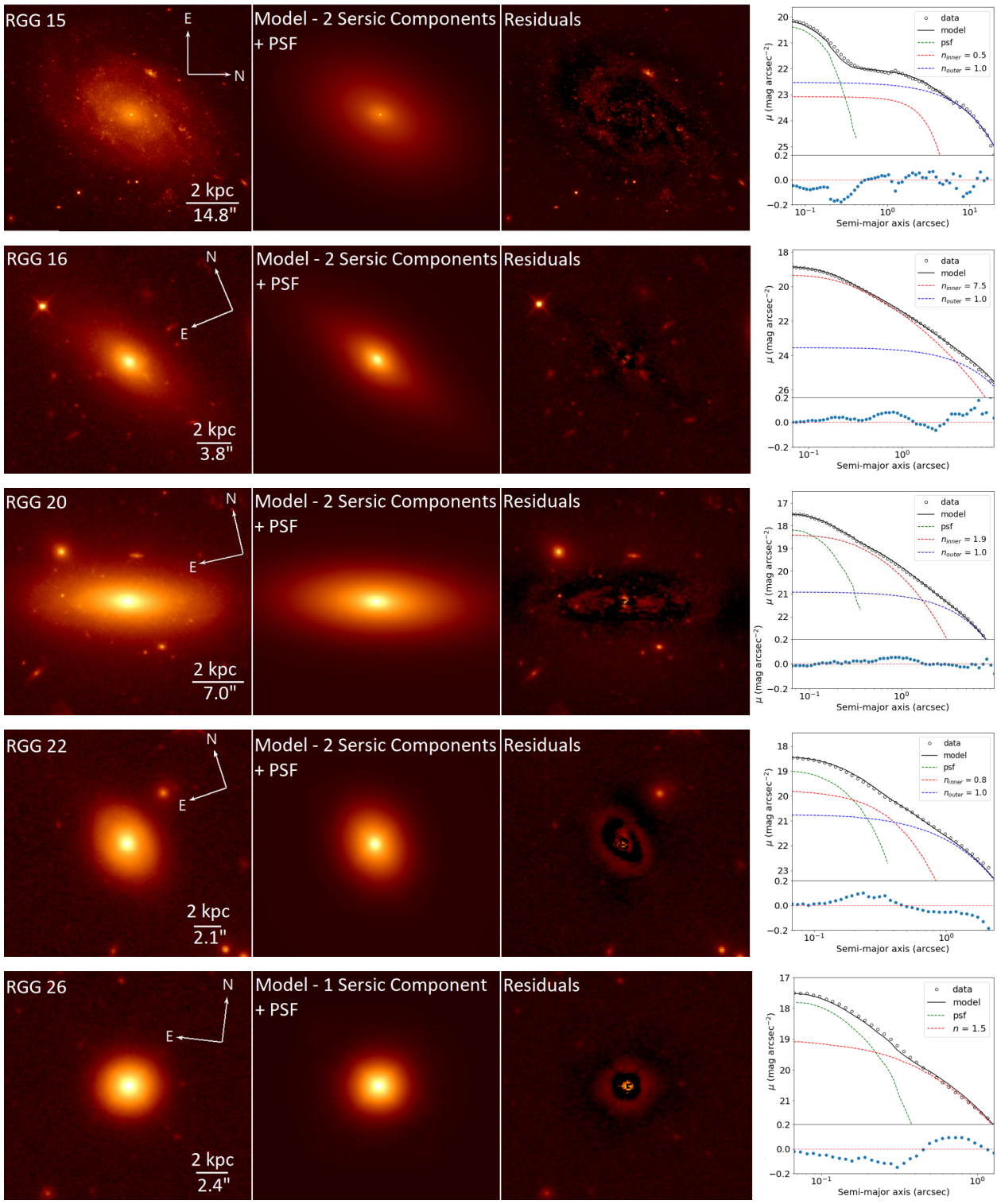

Figure 2.14: Left three panels: *HST* image, GALFIT model, and the residuals after subtracting the model from the image. Images are shown on a stretched log scale to show faint details in the residuals. Right: Surface brightness profiles. The data are shown as black circles and the model is shown as a black line. The individual model components are shown as colored dashed lines. The residuals are shown in the bottom panel.

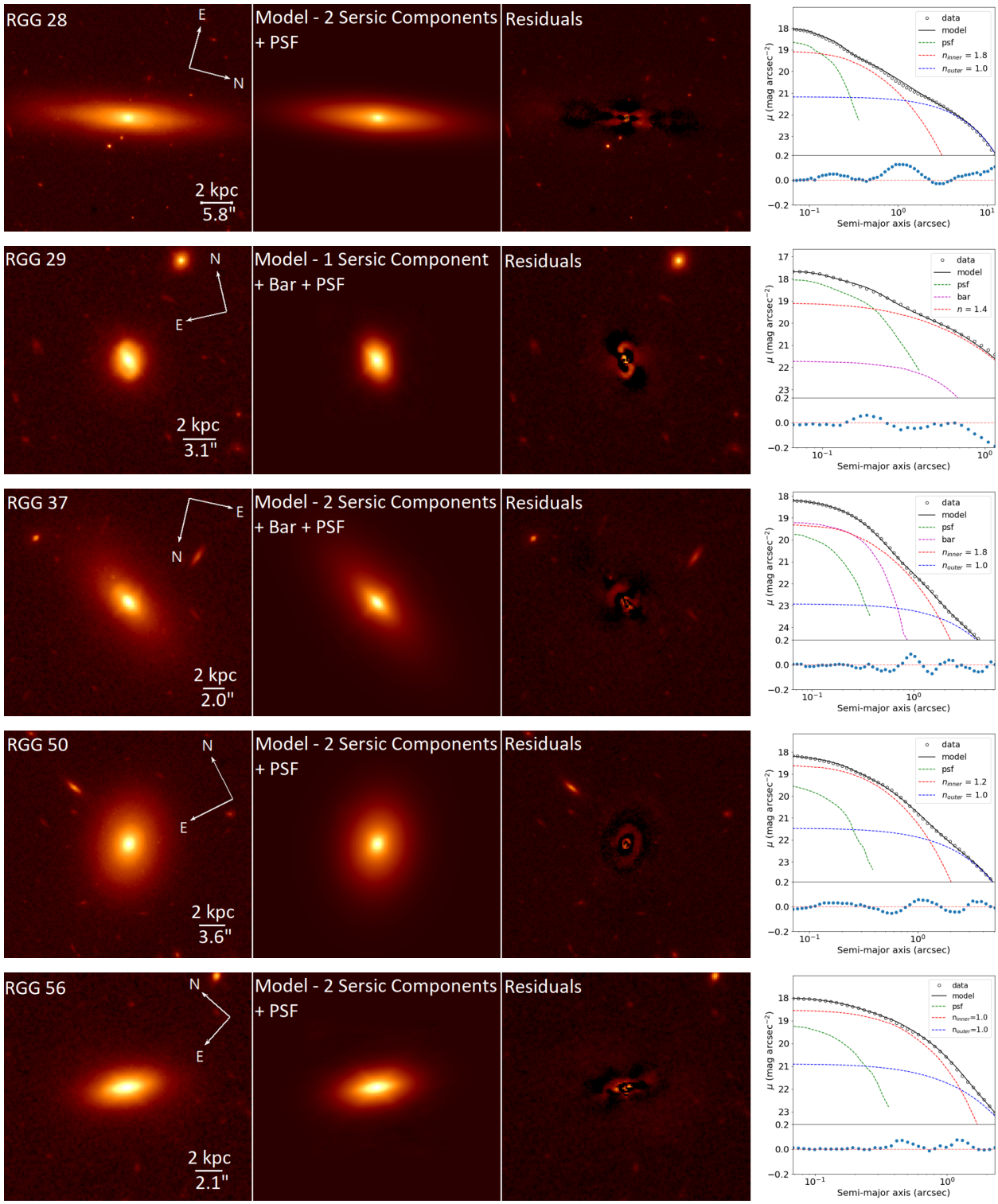

Figure 2.15: Left three panels: *HST* image, GALFIT model, and the residuals after subtracting the model from the image. Images are shown on a stretched log scale to show faint details in the residuals. Right: Surface brightness profiles. The data are shown as black circles and the model is shown as a black line. The individual model components are shown as colored dashed lines. The residuals are shown in the bottom panel.

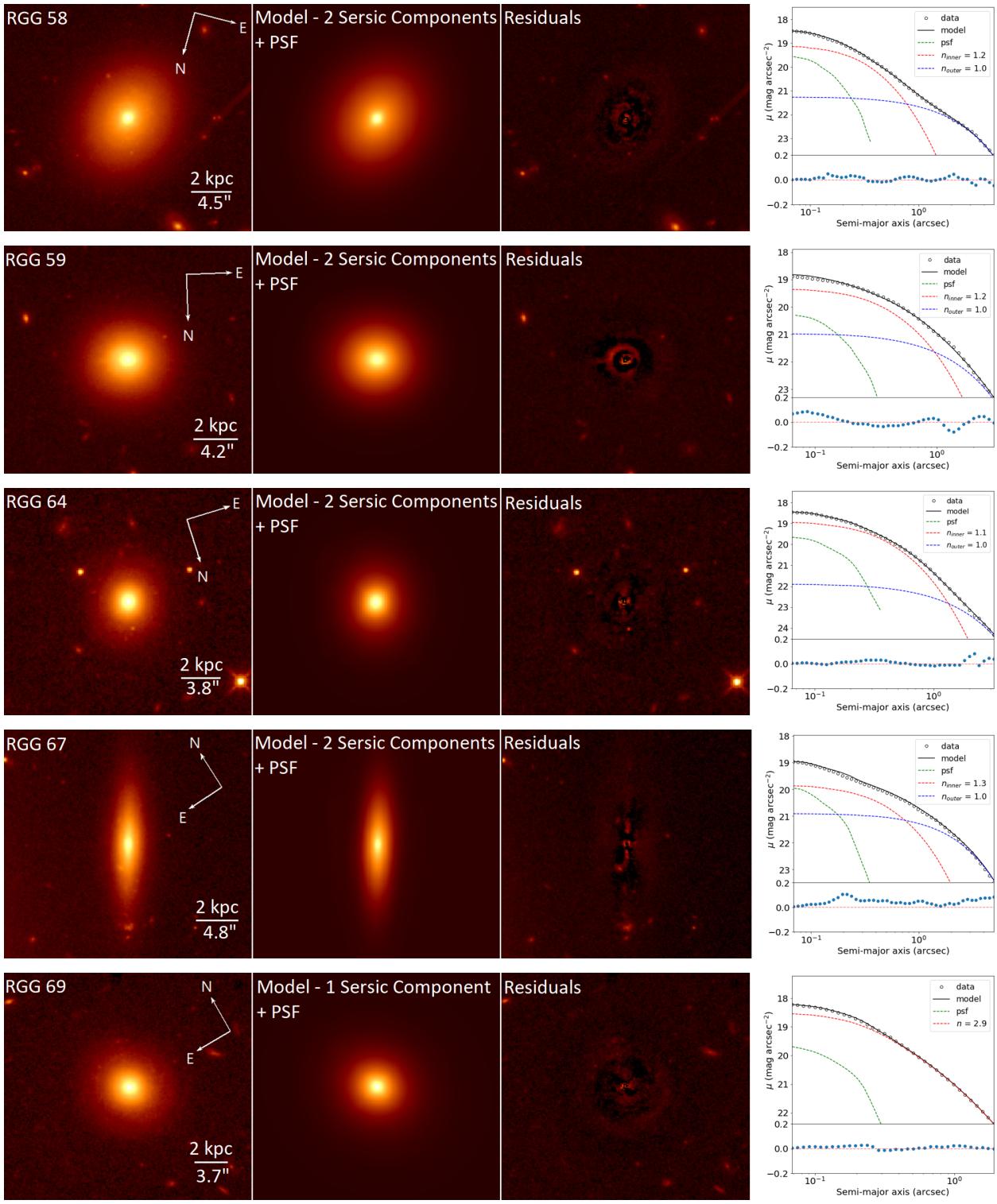

Figure 2.16: Left three panels: *HST* image, GALFIT model, and the residuals after subtracting the model from the image. Images are shown on a stretched log scale to show faint details in the residuals. Right: Surface brightness profiles. The data are shown as black circles and the model is shown as a black line. The individual model components are shown as colored dashed lines. The residuals are shown in the bottom panel.

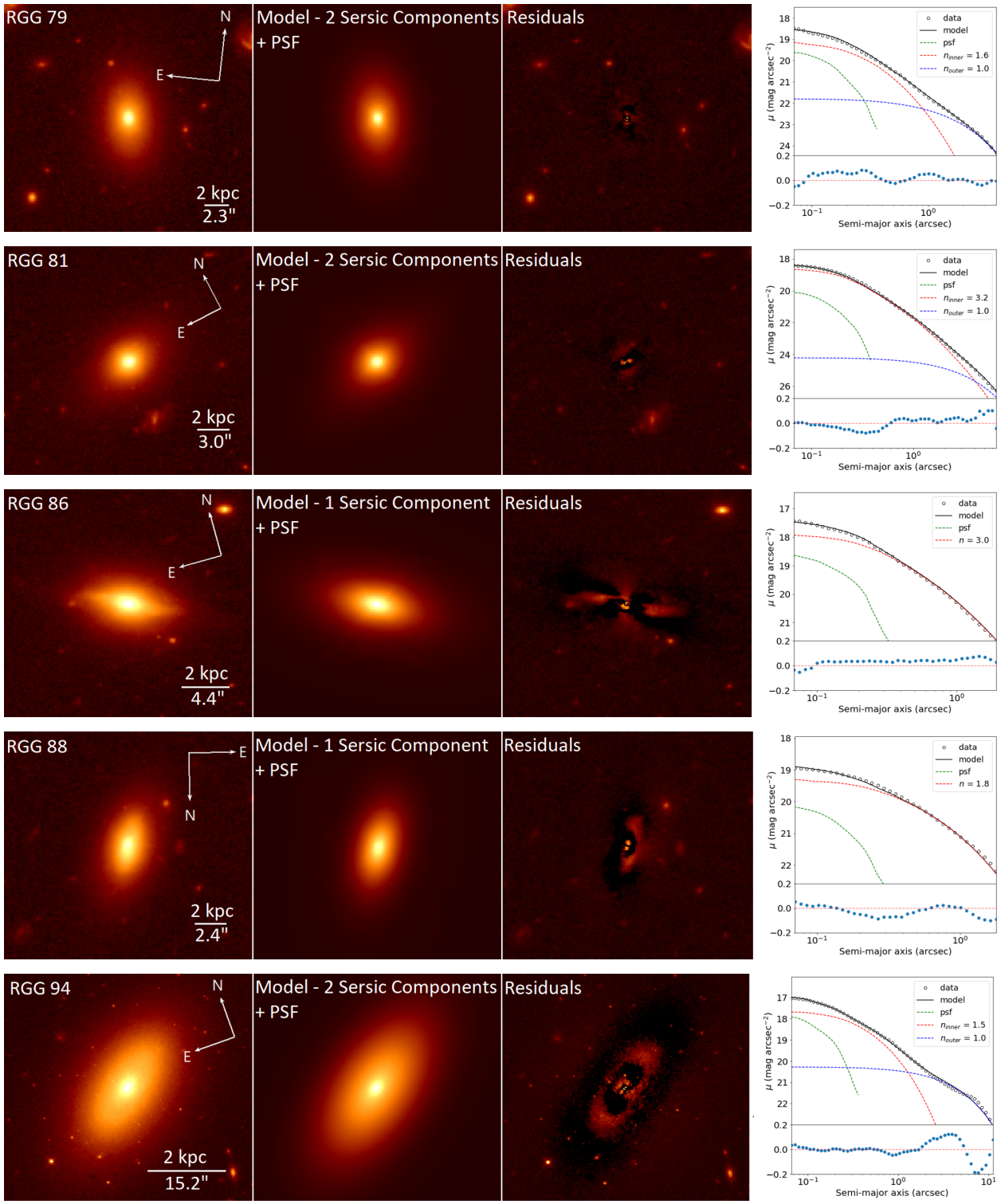

Figure 2.17: Left three panels: *HST* image, GALFIT model, and the residuals after subtracting the model from the image. Images are shown on a stretched log scale to show faint details in the residuals. Right: Surface brightness profiles. The data are shown as black circles and the model is shown as a black line. The individual model components are shown as colored dashed lines. The residuals are shown in the bottom panel.

Table 2.2. Fitting Results for Galaxies With Regular Morphologies

RGG ID	Component	m_{F110W}	n	R_e (kpc)	q	Additional Components
(1)	(2)	(3)	(4)	(5)	(6)	(7)
	PSF	21.86 ± 0.02	-	-	-	
RGG 1[a]	Inner Sérsic	19.52 ± 0.23	0.32 ± 0.09	0.71 ± 0.03	0.51	
	Outer Sérsic	17.41 ± 0.06	0.83 ± 0.13	1.61 ± 0.03	0.72	
	PSF	23.9 ± 0.01	-	-	-	
RGG 2	Inner Sérsic	20.3 ± 0.15	1.31 ± 0.01	0.73 ± 0.01	0.44	-
	Outer Sérsic	18.78 ± 0.10	1.00	2.16 ± 0.01	0.41	-
	PSF	20.41 ± 0.01	-	-	-	
RGG 4	Inner Sérsic	19.22 ± 0.06	0.87 ± 0.01	0.13 ± 0.01	0.95	
	Outer Sérsic	17.67 ± 0.03	1.00	0.68 ± 0.01	0.99	
	PSF	20.99 ± 0.05	-	-	-	
RGG 6	Sérsic	17.05 ± 0.10	3.52 ± 0.06	1.32 ± 0.04	0.81	
	PSF	23.07 ± 0.01	-	-	-	
RGG 7	Sérsic	18.93 ± 0.02	0.52 ± 0.01	1.41 ± 0.01	0.96	Bar ($m_{F110W} = 20.09$)
	PSF	21.86 ± 0.02	-	-	-	
RGG 9[a]	Sérsic	17.01 ± 0.04	2.30 ± 0.11	1.21 ± 0.26	0.86	
	PSF	22.39 ± 0.05	-	-	-	
RGG 10	Inner Sérsic	18.51 ± 0.01	3.97 ± 0.78	0.72 ± 0.15	0.48	
	Outer Sérsic	19.13 ± 0.05	1.00	2.21 ± 0.09	0.29	

Table 2.2 (cont'd)

RGG ID	Component	m_{F110W}	n	R_e (kpc)	q	Additional Components
(1)	(2)	(3)	(4)	(5)	(6)	(7)
	PSF	19.61 ± 0.03	-	-	-	
RGG 11[a]	Inner Sérsic	18.40 ± 0.23	2.40 ± 0.18	0.13 ± 0.02	0.96	
	Outer Sérsic	16.22 ± 0.18	1.69 ± 0.09	2.57 ± 0.30	0.78	
	PSF	22.54 ± 0.02	-	-	-	
RGG 15	Inner Sérsic	19.8 ± 0.17	0.48 ± 0.01	0.33 ± 0.01	0.70	
	Outer Sérsic	16.3 ± 0.01	1.00	1.96 ± 0.01	0.64	
	PSF	22.17 ± 0.01	-	-	-	
RGG 16	Inner Sérsic	18.52 ± 0.15	3.32 ± 0.22	0.98 ± 0.08	0.68	
	Outer Sérsic	19.50 ± 0.07	1.00	3.88 ± 0.04	0.30	
	PSF	20.45 ± 0.01	-	-	-	
RGG 20	Inner Sérsic	17.94 ± 0.15	1.86 ± 0.01	0.33 ± 0.02	0.46	
	Outer Sérsic	16.87 ± 0.07	1.00	1.93 ± 0.02	0.36	
	PSF	21.18 ± 0.01	-	-	-	
RGG 22	Inner Sérsic	20.55 ± 0.09	0.83 ± 0.05	0.28 ± 0.01	0.83	
	Outer Sérsic	18.9 ± 0.04	1.00	1.45 ± 0.03	0.78	
	PSF	20.08 ± 0.01	-	-	-	
RGG 26	Sérsic	18.54 ± 0.01	1.54 ± 0.09	0.68 ± 0.01	0.91	

Table 2.2 (cont'd)

RGG ID	Component	m_{F110W}	n	R_e (kpc)	q	Additional Components
(1)	(2)	(3)	(4)	(5)	(6)	(7)
	PSF	20.86 ± 0.02	-	-	-	-
RGG 28	Inner Sérsic	18.54 ± 0.03	1.77 ± 0.02	0.38 ± 0.01	0.56	
	Outer Sérsic	17.24 ± 0.02	1.00	2.83 ± 0.02	0.21	
	PSF	20.32 ± 0.01	-	-	-	
RGG 29	Sérsic	18.97 ± 0.01	1.40 ± 0.06	0.47 ± 0.01	0.61	Bar ($m_{F110W} = 22.26$)
	PSF	18.45 ± 0.03	-	-	-	
RGG 32[a]	Inner Sérsic	17.77 ± 0.25	1.62 ± 0.20	0.29 ± 0.02	0.90	
	Outer Sérsic	16.07 ± 0.10	0.74 ± 0.03	2.03 ± 0.01	0.95	
	PSF	21.96 ± 0.08	-	-	-	
RGG 37	Inner Sérsic	19.50 ± 0.01	1.79 ± 0.16	0.66 ± 0.01	0.53	Bar ($m_{F110W} = 20.66$)
	Outer Sérsic	19.60 ± 0.28	1.00	4.27 ± 0.15	0.47	
	PSF	21.55 ± 0.01	-	-	-	
RGG 48[a]	Inner Sérsic	19.75 ± 0.07	0.61 ± 0.08	0.29 ± 0.06	0.42	
	Outer Sérsic	16.64 ± 0.06	0.29 ± 0.01	2.12 ± 0.30	0.48	
	PSF	21.70 ± 0.10	-	-	-	
RGG 50	Inner Sérsic	18.66 ± 0.21	1.24 ± 0.03	0.30 ± 0.01	0.77	
	Outer Sérsic	18.09 ± 0.17	1.00	1.86 ± 0.01	0.75	

Table 2.2 (cont'd)

RGG ID	Component	m_{F110W}	n	R_e (kpc)	q	Additional Components
(1)	(2)	(3)	(4)	(5)	(6)	(7)
	PSF	21.42 ± 0.01	-	-	-	
RGG 56	Inner Sérsic	19.19 ± 0.01	1.04 ± 0.06	0.48 ± 0.01	0.26	
	Outer Sérsic	19.49 ± 0.02	1.00	1.48 ± 0.08	0.44	
	PSF	21.77 ± 0.01	-	-	-	
RGG 58	Inner Sérsic	19.45 ± 0.07	1.19 ± 0.01	0.19 ± 0.01	0.85	
	Outer Sérsic	17.82 ± 0.04	1.00	1.49 ± 0.01	0.81	
	PSF	22.53 ± 0.01	-	-	-	
RGG 59	Inner Sérsic	19.15 ± 0.15	1.19 ± 0.02	0.30 ± 0.01	0.83	
	Outer Sérsic	18.44 ± 0.07	1.00	0.96 ± 0.02	0.92	
	PSF	21.87 ± 0.02	-	-	-	
RGG 64	Inner Sérsic	19.05 ± 0.14	1.13 ± 0.01	0.26 ± 0.01	0.87	
	Outer Sérsic	19.36 ± 0.20	1.00	1.13 ± 0.04	0.82	
	PSF	22.24 ± 0.01	-	-	-	
RGG 67	Inner Sérsic	19.74 ± 0.15	1.29 ± 0.06	0.36 ± 0.01	0.66	
	Outer Sérsic	18.58 ± 0.07	1.00	1.38 ± 0.01	0.26	
	PSF	21.85 ± 0.01	-	-	-	
RGG 69	Sérsic	17.89 ± 0.15	2.88 ± 0.13	0.69 ± 0.01	0.90	

Table 2.2 (cont'd)

RGG ID	Component	m_{F110W}	n	R_e (kpc)	q	Additional Components
(1)	(2)	(3)	(4)	(5)	(6)	(7)
	PSF	21.84 ± 0.02	-	-	-	
RGG 79	Inner Sérsic	19.78 ± 0.18	1.61 ± 0.01	0.35 ± 0.01	0.66	
	Outer Sérsic	19.23 ± 0.09	1.00	2.17 ± 0.04	0.60	
	PSF	22.44 ± 0.13	-	-	-	
RGG 81	Inner Sérsic	18.74 ± 0.13	3.17 ± 0.14	0.49 ± 0.01	0.87	
	Outer Sérsic	20.90 ± 0.01	1.00	2.99 ± 0.05	0.40	
	PSF	20.79 ± 0.22	-	-	-	
RGG 86	Sérsic	17.68 ± 0.10	2.97 ± 0.15	0.56 ± 0.01	0.49	
	PSF	22.36 ± 0.22	-	-	-	
RGG 88	Sérsic	18.70 ± 0.10	1.79 ± 0.05	0.98 ± 0.01	0.87	
	PSF	21.72 ± 0.01	-	-	-	
RGG 89	Inner Sérsic	19.49 ± 0.02	1.39 ± 0.03	0.31 ± 0.01	0.88	
	Outer Sérsic	19.30 ± 0.02	1.00	1.42 ± 0.04	0.86	
	PSF	20.23 ± 0.01	-	-	-	
RGG 94	Inner Sérsic	17.47 ± 0.02	1.45 ± 0.02	0.09 ± 0.01	0.68	
	Outer Sérsic	15.71 ± 0.02	1.00	0.94 ± 0.01	0.54	

Table 2.2 (cont'd)

RGG ID	Component	m_{F110W}	n	R_e (kpc)	q	Additional Components
(1)	(2)	(3)	(4)	(5)	(6)	(7)
	PSF	24.26 ± 0.03	-	-	-	
RGG 118[b]	Inner Sérsic	20.55 ± 0.09	0.80 ± 0.10	1.57 ± 0.22	0.45	
	Outer Sérsic	18.66 ± 0.14	1.00	6.51 ± 1.72	0.69	
	PSF	18.94 ± 0.07	-	-	-	
RGG 119[a]	Inner Sérsic	19.36 ± 0.21	2.55 ± 0.47	0.17 ± 0.01	0.46	
	Outer Sérsic	17.23 ± 0.05	0.91 ± 0.06	1.02 ± 0.01	0.78	
	PSF	20.00 ± 0.2	-	-	-	
RGG 123[c]	Sérsic	17.53 ± 0.11	1.00	1.41 ± 0.09	-	
	PSF	19.94 ± 0.01	-	-	-	
RGG 127[a]	Inner Sérsic	20.40 ± 0.01	0.95 ± 0.48	0.09 ± 0.02	0.53	
	Outer Sérsic	18.13 ± 0.05	0.70 ± 0.23	1.25 ± 0.02	0.68	Bar ($m_{F110W} = 17.75$)

Note. — Column 1: identification number given in Reines et al. (2013). Column 2: Components in best-fit GALFIT model. Column 3: Total apparent ST magnitude reported by GALFIT. Column 4: Sérsic index reported by GALFIT. Column 5: Effective radius reported by GALFIT, converted to kpc. Column 6: Axis ratio (b/a) reported by GALFIT. Column 7: Any additional component included in the best-fit model.

Acknowledgements

We thank the anonymous referee for their helpful comments and questions during the review process. SJK acknowledges support for this project provided by a fellowship from the Montana Space Grant Consortium. Support for Program number HST-GO-14251.004A was provided by NASA through a grant from the Space Telescope Science Institute, which is operated by the Association of Universities for Research in Astronomy, Incorporated, under NASA contract NAS5-26555. AER gratefully acknowledges support for this paper provided by NASA through EPSCoR grant number 80NSSC20M0231.

A COMPARISON BETWEEN THE MORPHOLOGIES AND STRUCTURES OF DWARF GALAXIES WITH AND WITHOUT ACTIVE MASSIVE BLACK HOLES

Contribution of Authors and Co-Authors

Manuscript in following chapter

Author: Seth Kimbrell

Contributions: Analyzed the data, wrote the first draft of the manuscript.

Author: Amy Reines

Contributions: Provided edits and comments on the manuscript, advised on performing scientific analysis.

Author: Jenny Greene

Contributions: Provided scientific comments and edits on the manuscript

Author: Marla Geha

Contributions: Provided scientific comments and edits on the manuscript

Manuscript Information

Seth Kimbrell, Amy Reines, Jenny Greene and Marla Geha

The Astrophysical Journal

Status of Manuscript:
____ Prepared for submission to a peer-reviewed journal
_X_ Officially submitted to a peer-reviewed journal
____ Accepted by a peer-reviewed journal
____ Published in a peer-reviewed journal

IOP Publishing
March 10, 2023

Introduction

It is known that supermassive black holes (BHs) with masses up to $\sim 10^{10}$ $M_\odot$ reside in the center of massive galaxies (Kormendy & Richstone, 1995; Kormendy & Ho, 2013). This includes Saggitarius A*, the BH that lives in the center of the Milky Way, with a mass of 4 $\times$ 10^6 $M_\odot$ (Ghez et al., 2008). What is not nearly as well understood is the mechanism that led to the formation of the initial seeds of supermassive BHs (Greene et al., 2020; Volonteri, 2010; Inayoshi et al., 2020; Volonteri et al., 2021).

We know that BH seeds must have formed at very early cosmic times, since quasars are observed at redshifts as high as 7.5 (Mortlock et al., 2011; Vito et al., 2017; Bañados et al., 2018). This indicates that BH seeds existed and grew to enormous masses within the first Gyr after the Big Bang. While several distinct mechanisms have been advanced as possible formation channels (e.g., Loeb & Rasio, 1994; Madau & Rees, 2001; Begelman & Rees, 1978), we still do not know which, if any, reflect what happened in the earlier Universe.

While current technology does not allow us to observe and directly study seed BHs at high redshifts, dwarf galaxies in the local Universe that host the smallest supermassive (or just "massive") BHs give us an opportunity to study BHs that have not grown much compared to their more massive counterparts in giant galaxies. Studies regarding the demographics of BHs in dwarf galaxies (e.g., the BH occupation fraction) also facilitate constraints on the formation mechanisms of seed BHs (Volonteri, 2010; Habouzit et al., 2017; Greene, 2012; Miller et al., 2015; She et al., 2017). Dwarfs come in a wide variety of shapes and sizes, with structures ranging from very irregular galaxies to ellipticals and late-type spirals (McConnachie, 2012; Kormendy, 2015), and therefore understanding whether BHs appear preferentially in a particular type (or types) of dwarf galaxies is crucial as attempts are made to estimate the occupation fraction of BHs in dwarf galaxies (Reines, 2022).

To gain insight into what types of dwarf galaxies can host massive BHs, we previously

studied the morphologies and structures of 41 dwarf galaxies ($M_\star \leq 3 \times 10^9 M_\odot$) hosting optically-selected active galactic nuclei (AGNs) using *Hubble Space Telescope (HST)* near-infrared imaging (Kimbrell et al., 2021). Specifically, these objects were selected as AGN hosts using optical emission-line diagnostic diagrams (e.g., the BPT diagram; Baldwin et al. 1981). In this work, we refer to these as "optically selected," but we differentiate these from galaxies selected as AGN hosts via optical variability searches (see, e.g., Baldassare et al. 2020; Burke et al. 2023). Of these AGN-hosting dwarf galaxies, 85% have regular morphologies. Most of these regular galaxies are disk-dominated with small pseudobulges, although there are also a handful of bulge-like/elliptical galaxies. The remaining 15% of the sample are irregulars, including Magellanic-types and dwarf galaxies showing signs of interactions/mergers. Ideally, we would like to probe dwarf galaxies hosting both inactive and active BHs, however the vast majority of massive BHs known in dwarf galaxies come from samples of AGNs (for a review, see Reines, 2022).

In this work, we study the morphologies and structures of a sample of *non*-AGN-hosting dwarf galaxies for a comparison to the AGN sample presented in Kimbrell et al. (2021). We aim to determine if/how AGN-hosting dwarf galaxies differ from the dwarf galaxy population in general, and place AGN-hosting dwarf galaxies in the broader context of galaxy and BH evolution.

We describe our sample in Section 2. We present our analysis and results in Sections 3 and 4, respectively. A summary of our conclusions is in Section 5.

Observations and Sample Selection

We utilize ground-based near-infrared observations from the UKIRT Infrared Deep Sky Survey (UKIDSS) Large Area Survey (Lawrence et al., 2007) for our sample of non-AGN-hosting dwarf galaxies. UKIDSS utilizes the United Kingdom InfraRed Telescope (UKIRT), a 3.8m infrared telescope located at Mauna Kea in Hawai'i. The survey provides images in

the Z, Y, J, H, and K broadband filters.

We use the Y-band images with a central wavelength of 1.03 μm for comparison to Kimbrell et al. (2021), as this closely matches the *HST*/WFC3 F110W IR filter with an effective wavelength of 1.15 μm used in that work. The depth of the UKIDSS data is well-matched to our *HST* observations with a surface brightness sensitivity of $\mu_Y \sim 22.7$ mag arcsec^{-2} (Kelvin et al., 2012).

We construct our control sample of nearby dwarf galaxies that do not host optically-selected AGNs using version 0.1.2 of the the NASA Sloan Atlas (NSA), which is a catalog built from Sloan Digital Sky Survey (SDSS) observations (York et al., 2000; Blanton et al., 2011). We first impose a distance cut of ≤ 20 Mpc, corresponding to a redshift of ~ 0.005. By imposing this distance cut, we ensure that the ground-based images (with an angular resolution of $\sim 1''$) have a linear resolution comparable to the *HST* observations (Kimbrell et al., 2021) of the AGN-hosting dwarf galaxies that have a median distance of 111 Mpc (linear resolution of ~ 100 pc in both cases).

Imposing this requirement on distance left us with 2,404 objects. Stellar mass cuts were also placed such that $8.9 \leq \log(\mathrm{M}_*/\mathrm{M}_\odot) \leq 9.5$, so that we explore a mass range comparable to the dwarf galaxies hosting AGNs in Kimbrell et al. (2021). This leaves 229 objects.

Of the 229 objects selected in the NSA, 82 had images in the UKIDSS Large Area Survey. However, upon inspection of the data, 22 galaxies did not have sufficient image quality for our analysis. Often this was because the galaxy was on the edge of the image. In other cases, there were large numbers of bad pixels in the image, or the galaxy had too low S/N to accurately analyze. In the end, we were left with 60 dwarf galaxies with high-quality images in UKIDSS. None of these galaxies were selected as AGNs by Reines et al. (2013), which used the same parent sample of dwarfs; however, two of these 60 were selected as BPT composites and so were excluded from this work. In addition, one of the dwarfs has an X-ray detection in the Chandra Source Catalog (Evans et al., 2010), and so we exclude this source

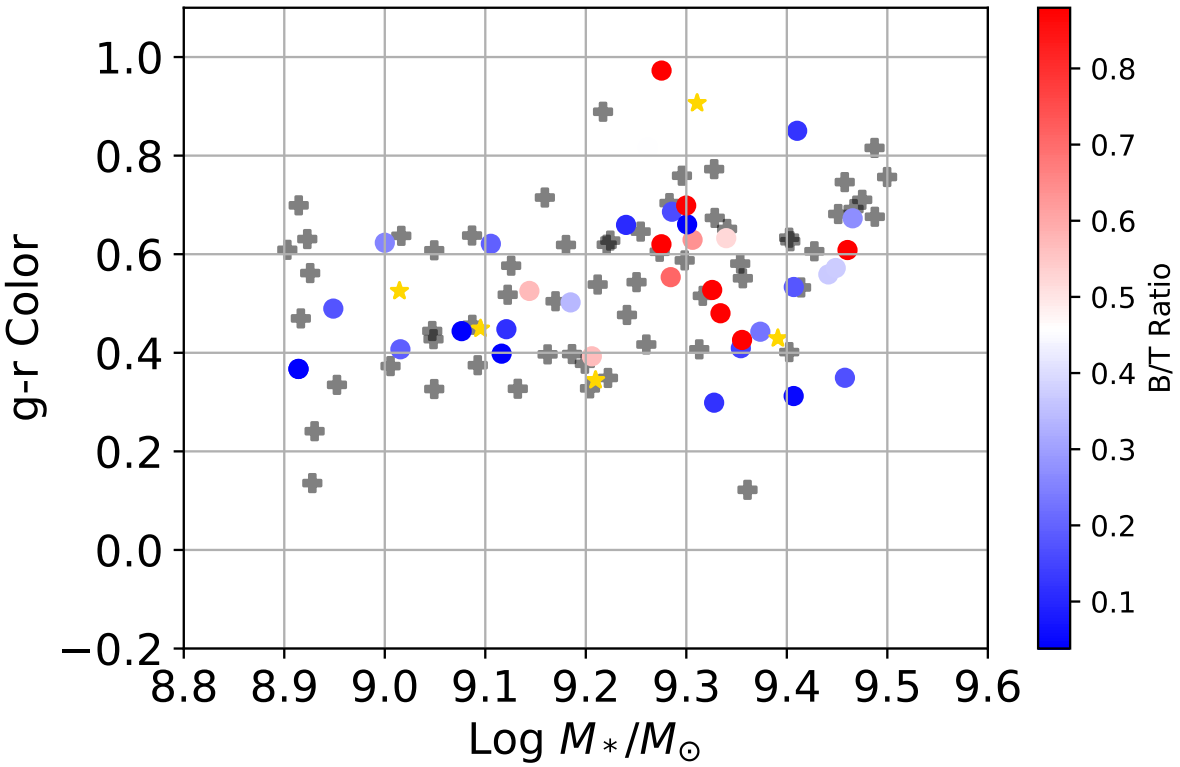

Figure 3.1: Color-mass diagram for our sample of dwarf galaxies analyzed in this work that *do not* host an AGN (grey crosses) and those analyzed in Kimbrell et al. (2021) that *do* host an AGN, demonstrating that both samples span a similar mass and color range. The AGN sample of Kimbrell et al. (2021) is color coded by bulge-to-total (B/T) light ratio. Yellow stars indicate the irregular galaxies in the AGN sample.

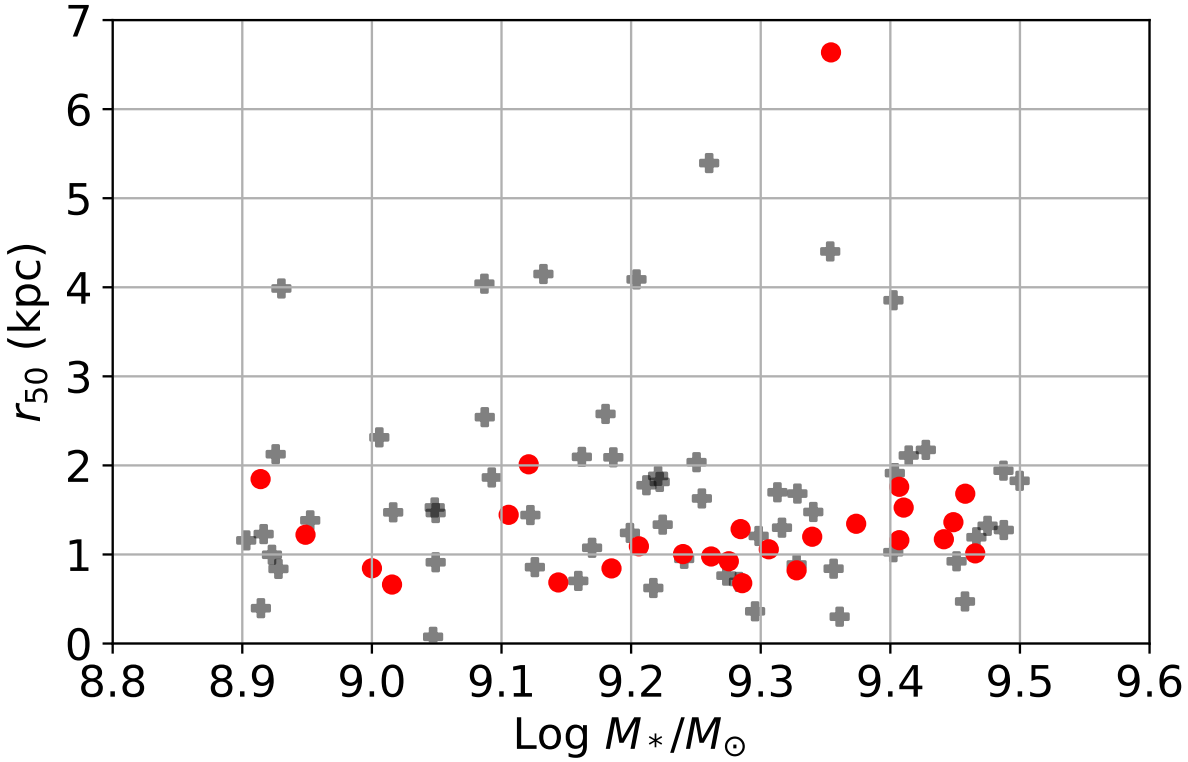

Figure 3.2: Size-mass diagram for our sample of dwarf galaxies analyzed in this work that do not host an AGN (grey crosses) and those analyzed in Kimbrell et al. (2021) that do host an AGN (red dots), demonstrating that both samples span a similar mass and size range.

as well, leaving 57 dwarf galaxies which do not exhibit evidence for AGNs. To demonstrate that these galaxies have similar physical properties as the comparison AGN hosts, Figure 3.1 shows the $g - r$ color-mass diagram of this sample, as well as the Kimbrell et al. (2021) sample for comparison. Figure 3.2 shows the size-mass diagram, using the Petrosian 50% light radius reported by the NSA, of the two samples for comparison.

Analysis

The aim of this work is to analyze the structures of dwarf galaxies that do not show evidence of hosting an active massive BH, so that we may compare these results to those of galaxies that do show evidence of hosting an active massive BH. We are especially interested in finding how often these galaxies possess an inner (pseudo)bulge component in addition to a disk, and whether the (pseudo)bulge or disk dominates the total galaxy light. Irregular galaxies make up 14% (8/57) of our sample and their structures can not be accurately modeled in GALFIT (Peng et al., 2010). For the 49 dwarf galaxies in our sample with regular morphologies, we model each galaxy with four models using one or two Sèrsic components with and without point spread functions (PSFs). The PSFs may represent nuclear star clusters (NSCs), which are known to be common in galaxies in this mass range (Carlsten et al., 2021; Sánchez-Janssen et al., 2019; Neumayer et al., 2020). The inner Sèrsic component of a two component model can be interpreted as the (pseudo)bulge, with the outer component fixed as an exponential disk. For galaxies that are viewed edge-on in our imaging, we replace the Sèrsic model representing the disk with an edge-on disk model.

PSF Construction

An important step in modeling these galaxies is construction of an accurate PSF, which models the detector response to a point source of light. An inaccurate PSF risks inaccurate modeling of the galaxy as a whole. The variability of seeing conditions requires a PSF to

be created for each galaxy. For each galaxy, we selected an isolated star and cut out a $\sim 20 \times 20$ pixel square centered on the star. We then created a model of the star in GALFIT using as many Sérsic components as necessary until the residuals showed only random noise. This is a standard method for PSF creation using GALFIT[1]. We do not attempt to model physical parameters of the starlight, so the number of Sérsic components and their values are not important. We simply require an analytic model that accurately captures the shape of the star. We subtract the estimated sky background in order to create a model of the star with a very high signal-to-noise ratio, as required of PSFs. Figure 3.3 shows an example of a star image, the corresponding PSF model and the residuals.

We performed fitting on each galaxy with inaccurate PSFs as well, testing the PSF fitting as a whole. The use of an inaccurate PSF will lead to systematic structures in the residuals of every attempted model. This will most often occur if the background of the PSF is not perfectly subtracted, or if an improper model (such as a pure Gaussian) is used. In the former case, a bright square will appear in the center of the galaxy upon modeling. In the latter case, the residuals will show obvious signs of subtracting a symmetric model rather than a typically somewhat asymmetric star profile.

Galaxy Modeling

We used the galaxy fitting software GALFIT (Peng et al., 2010) to fit analytical two-dimensional models to our images. There are many models that GALFIT can use to fit galaxies, many of which are used for specific morphologies (e.g. the de Vaucouleurs profile which is often used to model classical bulges (de Vaucouleurs, 1948), or the edge-on disk function). For the galaxies in this work, we attempted to use the very general Sérsic profile, which takes the form (Sérsic, 1963):

[1] users.obs.carnegiescience.edu/peng/work/galfit/TFAQ.html

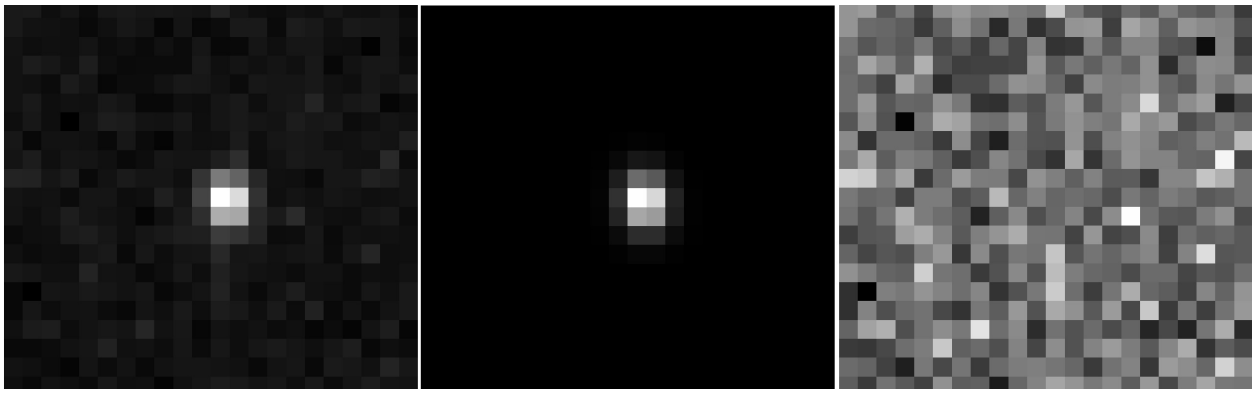

Figure 3.3: Star used for PSF creation for Galaxy UK6 (left); model PSF created using GALFIT (middle); residuals resembling random noise after subtracting the model PSF from the image of the star (right).

$$\Sigma(r) = \Sigma_e \times \exp\left[-\kappa\left(\left(\frac{r}{r_e}\right)^{\frac{1}{n}} - 1\right)\right] \tag{3.1}$$

where r_e is the effective radius such that half of the flux lies within r_e; Σ_e is the surface brightness at the effective radius r_e. The parameter n is the Sérsic index and is coupled to the parameter κ. A higher Sérsic index indicates extended wings and a sharp brightness profile at the center of the galaxy. κ is defined as $\kappa = \Gamma(2n)/2$, with Γ being the complete gamma function. The case of $n = 4$ reduces to the de Vaucouleurs profile, $n = 1$ corresponds to an exponential disk profile, and $n = 0.5$ is a Gaussian profile.

We followed the same fitting process as Kimbrell et al. (2021), recommended by Peng et al. (2010). We began by fitting a single Sèrsic component to a given galaxy, which in some cases was the best fitting model. However, even if it was a poor fit, this model gave us basic structural information about the galaxy (e.g. effective radius, axis ratio) that informed the initial conditions of more complex models. Following the single-Sèrsic model, we added a PSF and re-ran GALFIT, using the results of the previous run as the initial parameters for the Sèrsic component. This PSF could represent a nuclear star cluster, which are known to

be common in galaxies in this mass range (Neumayer et al., 2020).

We proceeded with our modeling by fitting the galaxies with a two-Sèrsic model with no PSF. We let every parameter of the inner Sèrsic component vary while fixing the Sèrsic index n of the outer Sèrsic component at $n = 1$, which is the typical value for an exponential disk. Even in galaxies which clearly have a bright point source at their center, starting with a simpler model without a PSF is important in order to get structural information about the individual components before adding more complexity with a PSF. Finally, we fit a model with an inner Sèrsic component, an exponential disk and a PSF.

Every model previously discussed also includes a sky component. We assume a flat sky with no variations across the whole of each image, and we let GALFIT fit for the brightness of the sky. In principle, a small patch of the sky that is significantly brighter or dimmer than the rest can be masked out, allowing GALFIT to ignore it in the fitting. However, this was never necessary for this work, and a flat sky adequately modeled the background light in every instance.

Unlike the Kimbrell et al. (2021) sample, this sample includes several galaxies with regular morphologies that are not well fit by any of the above models. Some galaxies are edge-on and there are also some spiral galaxies. When possible, these were modeled using the more specific GALFIT components, following the same basic path detailed above: first the simplest model (edge-on disk, spiralled Sèrsic, etc.) was applied without a PSF, then a PSF was included, then any other components were added as necessary (e.g., a bulge inside the disk, a non-spiralled interior component). However, while spirals can be very obvious to the eye, GALFIT can struggle to accurately distinguish a spiral. This will not significantly affect the results of the decomposition that we perform, and so galaxies with spirals that cannot be modeled well by GALFIT were modeled in the same way as galaxies without spirals, with acceptance that some spiral structure will be present in the residuals.

Model Selection

With the analysis completed, we determined which model best fit each galaxy. We simultaneously considered all possible models for each galaxy in order to pick the best one. In 26 of the 49 galaxies we modeled, GALFIT was unable to converge on any two component model, leaving only models including one Sèrsic with or without a PSF. In 13 others, GALFIT would only converge on a two component model with non-physical parameters, such as a (pseudo)bulge that is dominant over the disk everywhere, an unrealistically high Sèrsic index, or an effective radius indicative of the Sèrsic component attempting to fit the sky background. For the 8 galaxies in which GALFIT converged to a high inner Sèrsic index, we re-attempted the modeling with the inner Sèrsic index constrained to $n \leq 5$, but these runs never resulted in a better fit than the non-constrained runs.

For model selection, we followed the process of Oh et al. (2017) to be consistent with Kimbrell et al. (2021). This was a three-step selection process. First, we examined the radii of both components in the two component models. If the exponential disk had an effective radius smaller than that of the inner (pseudo)bulge, that two component model was rejected. Next, we examined the inner component. If a two component model led to the inner Sèrsic being dominant over the disk at all radii, we rejected that two component model. The inner component was also our primary metric when deciding whether or not to include a PSF. A galaxy that requires a PSF, yet one is not included in the model, will often have a high inner Sèrsic component to try to capture the excess of light at the center. Evidence from observations of dwarf galaxies with and without AGNs (see, e.g. Schutte et al. 2019; Jiang et al. 2011; Graham & Guzmán 2003; Kormendy & Ho 2013) supports both dwarf ellipticals and (pseudo)bulges having Sèrsic indices $n \leq 4$. In order to have a conservative rejection criterion, we rejected any PSF-included model that included an inner Sèrsic component $n \geq 5$. Examination of the residuals also helped select for PSF necessity. A Sèrsic component attempting to account for an inner point source leads to telltale concentric

circles in the residuals, alternating light and dark, near the galaxy center. If visual inspection of the residuals show these rings when the PSF is absent, we took this as evidence of the necessity of a PSF component. The final selection metric between the models was the Akaike Information Criterion (AIC). The AIC is a statistical criterion used to select between different models, and can be calculated from χ^2, assuming normally distributed noise, as follows:

$$\mathrm{AIC} = \chi^2 + 2k \tag{3.2}$$

with k being the number of free parameters in a given model. A more complicated model (i.e., one with an additional component) must improve the AIC by at least 10 to be accepted over the less complicated one, to remain consistent with Kimbrell et al. (2021). Of the 49 dwarf galaxies with regular morphologies, 36 were best fit by a single component model, leaving 13 best fit by a two component model. A PSF was required for 41 of the 49 regular dwarf galaxies. These results are further discussed in Section 4.

Results and Discussion

Demographics of Dwarf Galaxy Sample

Of our sample of 57 non-AGN-hosting dwarf galaxies studied here, 49 galaxies have regular morphologies (86%). We modeled these in GALFIT using either one or two Sèrsic components, sometimes with a PSF, or an edge-on disk (and possibly a bulge). Figure 3.4 shows some examples and we report the results of our modeling in Table 3.1. Meanwhile, 8/57 (14%) have irregular/disturbed morphologies and could not be accurately modeled in GALFIT (see Figure 3.6).

The majority (39) of the regular dwarf galaxies are relatively face-on, while 10 are edge-on dwarfs. Of the 39 face-on dwarfs, we have determined that 30 ($\sim$ 78%) are best fit by a single Sèrsic component, while nine ($\sim$ 22%) are best fit by a two-component (pseudo)bulge

+ disk model. For the galaxies best fit by a single Sèrsic component, we differentiate between elliptical/(pseudo)bulge-like galaxies and disk-like galaxies using the Sèrsic index n. A dwarf galaxy fit by a component with $n < 1.5$ is called "disk-like", to retain consistency with Kimbrell et al. (2021). A dwarf fit by a component with $n \geq 1.5$ is called "elliptical" or "(pseudo)bulge-like". Of the 10 edge-on dwarf galaxies, 4 are best fit with a disk + a (pseudo)bulge, while the other six are best fit with a single-component edge-on disk. We find that a PSF component is required in $\sim 84\%$ of these regular galaxies.

In order to gauge how well this sample represents the general population of dwarf galaxies, we compare our results to dwarf galaxy demographics explored by Reines (2022) using the Catalog and Atlas of the Local Volume Galaxies (Karachentsev et al., 2013). Assuming K-band luminosity is a good proxy for stellar mass to first order, Table 1 in Reines (2022) indicates that 63% of galaxies in the mass range $10^9 < M_*/M_\odot < 10^{9.5}$ are late-type spiral galaxies (Sdm, Sd) while 26% are irregular galaxies, Magellanic irregulars and blue compact dwarf galaxies. Reines (2022) quotes a total of 12% for earlier-type galaxies in this mass range.

While not identical, we find comparable statistics among our sample of dwarf galaxies without evidence of active massive BHs studied here, which spans the mass range given above – $\sim$68% of the galaxies studied here are either pure disks ($\sim 46\%$) or disk-dominated galaxies with fainter (pseudo)bulges ($\sim$22%). Irregular galaxies make up 14% of our sample and $\sim 18\%$ of the galaxies are best fit with elliptical/spheroidal models. Overall, we find a higher proportion of early-type galaxies than reported by Reines (2022) and fewer irregulars, but as a whole our sample is fairly consistent with the general population of nearby dwarf galaxies. We show the comparison in Figure 3.5.

We also compare our sample to that analyzed in Baldry et al. (2012). In that work, a sample of 2711 galaxies in the local universe ($0.025 < z < 0.06$) were selected from the Galaxy and Mass Assembly Survey (GAMA). These galaxies were separated by their morphologies

and binned by total stellar mass. It was found that at low stellar mass, $\log(M_*/M_\odot) \lesssim 10$, the local universe is mostly populated by disk-dominated and irregular galaxies, with a low fraction of elliptical and spheroid-dominated galaxies, further confirming that our sample of inactive galaxies is representative of the local volume of galaxies in this mass range.

Comparison to Dwarf Galaxies with AGNs

First, we note that the fraction of regular (86%) and irregular (14%) galaxies found here for the non-AGN-hosting dwarf galaxies is very nearly the same as for the AGN-hosting galaxies presented in Kimbrell et al. (2021) (85% and 15%, respectively). Below, we focus on the similarities/differences between dwarf galaxies with regular morphologies in the two samples.

The dwarf galaxies in our sample best fit by two Sèrsic components, indicating a (pseudo)bulge + disk, have bulge to total light ratios somewhat lower on average than the AGN hosts studied in Kimbrell et al. (2021). Here, the two-component galaxies have a median bulge-to-total ratio (with PSF subtracted) $\langle B/T \rangle = 0.08$, compared to 0.21 for the AGN hosts. We also find a much smaller proportion of our current sample requiring a two component model; only $\sim 23\%$ of our face-on galaxies are so modeled ($\sim 27\%$ when including edge-on galaxies), while $\sim 76\%$ of galaxies modeled in Kimbrell et al. (2021) had a (pseudo)bulge and a disk. The presence of edge-on galaxies in our sample also differentiates it from the Kimbrell et al. (2021) sample. We report 10 ($\sim 18\%$) of the galaxies in our sample are edge-on. Kimbrell et al. (2021) reported no edge-on galaxies at all. However, this may be a selection effect since low-luminosity AGNs may be more difficult to detect in edge-on galaxies where the light can be more easily obscured.

We apply the two-sample Kolmogorov-Smirnov (K-S) test (Massey, 1951) to the distribution of B/T ratios of this sample of galaxies and the B/T ratios of the AGN hosts modeled in Kimbrell et al. (2021). The two-sample K-S test takes in two samples of data

and returns a statistic which measures the maximum distance between the two empirical cumulative distribution functions. The benefit to the two-sample K-S test is that it can help investigate whether two samples are likely to be drawn from the same underlying distribution without needing to know that distribution. For these two samples of B/T ratios, the two-sample K-S test returns a $\sim 0.8\%$ chance of drawing data as dissimilar as these if they came from the same distribution of B/T ratios. However, we also run the two-sample K-S test comparing just the two-component galaxies in the AGN host sample and our sample. This way, we compare the (pseudo)bulge + disk galaxies that were selected as AGN hosts to the (pseudo)bulge + disk galaxies that were not. In this case, we find that there is a $\sim 4\%$ chance of drawing B/T ratio distributions so dissimilar if they came from the same distribution. It seems that while some difference exists structurally between the AGN hosts in Kimbrell et al. (2021) and the sample presented here, the primary difference between them is the presence (or lack thereof) of a (pseudo)bulge.

We further show this in Figures 3.7 and 3.8. In Figure 3.7 we show the distribution of B/T ratios for strictly the two-component galaxies in each sample. We find a somewhat similar distribution, with the majority of each sample of two-component dwarf galaxies being disk-dominated. In Figure 3.8 we show the number of each morphology type present in each sample. While both the AGN hosts of Kimbrell et al. (2021) and the dwarf galaxies in this sample show similar fractions of dwarf ellipticals, the sample analyzed in this work is dominated by disk-like single-component galaxies, which are hardly present in Kimbrell et al. (2021). This reinforces the notion that the primary structural difference between this sample and the AGN hosts analyzed in the previous work is the presence of a (pseudo)bulge, rather than the relationship between the disk and (pseudo)bulge, when present.

We also show the Sèrsic indices of the inner components of our two-component galaxies in Figure 3.9. We find that the inner (pseudo)bulge components of our sample were structurally similar to the Kimbrell et al. (2021) sample of AGN hosts; our galaxies had

a median inner Sèrsic index $< n >= 1.49$, compared to $< n_{\mathrm{AGNHosts}} >= 1.31$. Performing the two-sample K-S test on the inner Sèrsic indices supports this similarity, finding a $\sim$ 61% chance of drawing data this dissimilar if they came from the same distribution of Sèrsic indices. We reiterate that only nine of the galaxies in our sample possessed a (pseudo)bulge, so this comparison must be taken with extra caution.

Nature of the Point Sources

Despite not being selected as hosts of AGNs, 41 of the 49 ($\sim$ 84%) regular galaxies in our sample are best fit by a model including a point source of light. As shown in the literature (e.g., Neumayer et al., 2020; Sánchez-Janssen et al., 2019; den Brok et al., 2014; Kimbrell et al., 2021), this is entirely consistent with the proportion of galaxies in this mass range which are expected to host nuclear star clusters (NSCs).

We search for any difference between the PSFs of this inactive sample and the PSFs of the AGN-hosting dwarf galaxies of Kimbrell et al. (2021). We show the comparison between the luminosities in Figure 3.10, which shows a large gap between the two samples. On average, the PSFs in the AGN-hosting dwarf galaxies are 310 times more luminous than those in the non-AGN-hosting dwarfs.

While we cannot definitively determine the origin of the point sources in these galaxies, the marked difference between the PSF luminosities in the two samples suggests that the PSFs in the Kimbrell et al. (2021) sample are dominated by AGN light, while the proportion of galaxies in this inactive sample hosting a PSF in the best-fit model is consistent with the proportion of galaxies in this mass range hosting nuclear star clusters (Neumayer et al., 2020).

We compare the 1.03μm luminosities of the PSFs in our sample to the nine nuclear star clusters in late-type dwarf galaxies studied in Georgiev et al. (2009). We use the Python synphot routine to convert the luminosities reported there in the ACS F814W filter to 1.03μm

using Bruzual & Charlot (2003) population synthesis models at a variety of ages, assuming no extinction. We find that the luminosities of our PSFs are consistent with the estimated luminosities of known nuclear star clusters in dwarf galaxies (see Figure 3.11).

We perform a similar comparison between the PSFs of the Kimbrell et al. (2021) AGN hosts and the PSFs of the hosts of low-mass black holes reported by Greene & Ho (2007) and studied by Jiang et al. (2011) in the WFPC2 F814W filter. We use a power law spectrum for an AGN: $f_\lambda \propto \lambda^\alpha$ with $\alpha = -1.56$ when $\lambda \leq 5000$ Åand $\alpha = -0.45$ for $\lambda > 5000$ Å(Vanden Berk et al., 2001). Using this spectrum, we convert the luminosities reported in Jiang et al. (2011) for the PSFs to the F110W (central wavelength 1.15 μm) filter used in Kimbrell et al. (2021). The Greene & Ho (2007) sample are more massive galaxies than the dwarfs studied in Kimbrell et al. (2021) and host more massive BHs than the dwarfs. In addition, most of the dwarfs do not exhibit broad emission lines like the Greene & Ho (2007) sample, which may indicate more obscured AGNs in Kimbrell et al. (2021). For these reasons, we do not expect the Kimbrell et al. (2021) PSFs to be as luminous. We find that the dwarf AGNs hosts have PSF luminosities lower than the Greene & Ho (2007) sample; however, given the considerations above, these are more consistent with the more massive AGNs than the nuclear star clusters found in dwarf galaxies. This suggests that the PSFs found in the sample of non-AGNs studied here are likely NSCs, while the PSFs in Kimbrell et al. (2021) are likely dominated by AGN light. We show the results of both of these comparisons in Figures 3.11 and 3.12, on identical vertical axes for ease of comparison.

Conclusions

We presented a study of the morphologies and structures of 57 dwarf galaxies that do not show signs of hosting an optical AGN. We have compared the demographics of this sample to the study performed on dwarf galaxies that do host AGNs in Kimbrell et al. (2021). We summarize our results below:

1. The sample of non-AGN-hosting dwarf galaxies analyzed in this work, selected to span the same range of stellar mass and physical resolution as the Kimbrell et al. (2021) sample of AGN-hosting dwarfs, is representative of the general population of dwarf galaxies in the local volume (see Figure 3.5).

2. Overall, we find nearly the same fraction of regular (86%) versus irregular (14%) galaxies among the dwarf galaxy samples with and without optically-selected AGNs.

3. Both samples also have similar fractions of regular, early-type/elliptical dwarf galaxies ($\sim 18\%$).

4. The primary morphological difference between the two samples is among the galaxies with disks. A large fraction of the non-AGN hosts are pure disk galaxies with no detectable (pseudo)bulges, while the vast majority of the AGN-hosting dwarfs have detectable (pseudo)bulges (see Figure 3.8).

5. We also find 10 ($\sim 18\%$) edge-on galaxies in our sample here, of which none were found among the AGN hosts. This could be a selection effect since low-luminosity AGNs are likely more difficult to detect in edge-on galaxies where the light can be more easily obscured.

6. A central point source of light is present in $\sim 84\%$ of the best-fit models for the regular, face-on dwarf galaxies in the sample of non-AGN hosts. This proportion is consistent with the expected fraction of galaxies hosting nuclear star clusters in this stellar mass range (Neumayer et al., 2020). We find the luminosities of these point sources to be consistent with estimated luminosities at this wavelength of known NSCs in dwarf galaxies (Georgiev et al., 2009).

7. In contrast, all of the AGN host galaxies require a point source in their best fit model and the average luminosity of the PSFs is more than two orders of magnitude higher

than that of the non-AGN hosts, and are largely consistent with luminosities expected of AGNs in this wavelength (Jiang et al., 2011; Greene & Ho, 2007), suggesting the point sources in the AGN hosts are dominated by AGN light.

We have shown that dwarf galaxies with optically-selected AGNs are overall structurally different from the general population of dwarf galaxies. Primarily, we have found that dwarf galaxies hosting AGNs are more likely to host a central (pseudo)bulge than the general population of dwarf galaxies, which contains a much higher fraction of pure disks. Schutte et al. (2019) demonstrated that scaling relations between BH mass and bulge mass extend down to the dwarf galaxy regime, however the origin of such relations is debated (e.g., Kormendy & Ho, 2013). In any case, our findings suggest that AGNs are likely to be preferentially found in dwarf galaxies containing (pseudo)bulges. These results agree with those of the mid-IR spectroscopic study of Satyapal et al. (2009), who found that AGNs in pure bulgeless galaxies are indeed rare in this mass range.

This work also has implications for the search for BHs in dwarf galaxies, which is important for constraining the BH occupation fraction in low mass galaxies. The BH occupation fraction in dwarfs, in turn, is a key diagnostic for discriminating between possible seeding mechanisms of supermassive black holes (Volonteri, 2010; Greene, 2012; Ricarte & Natarajan, 2018).

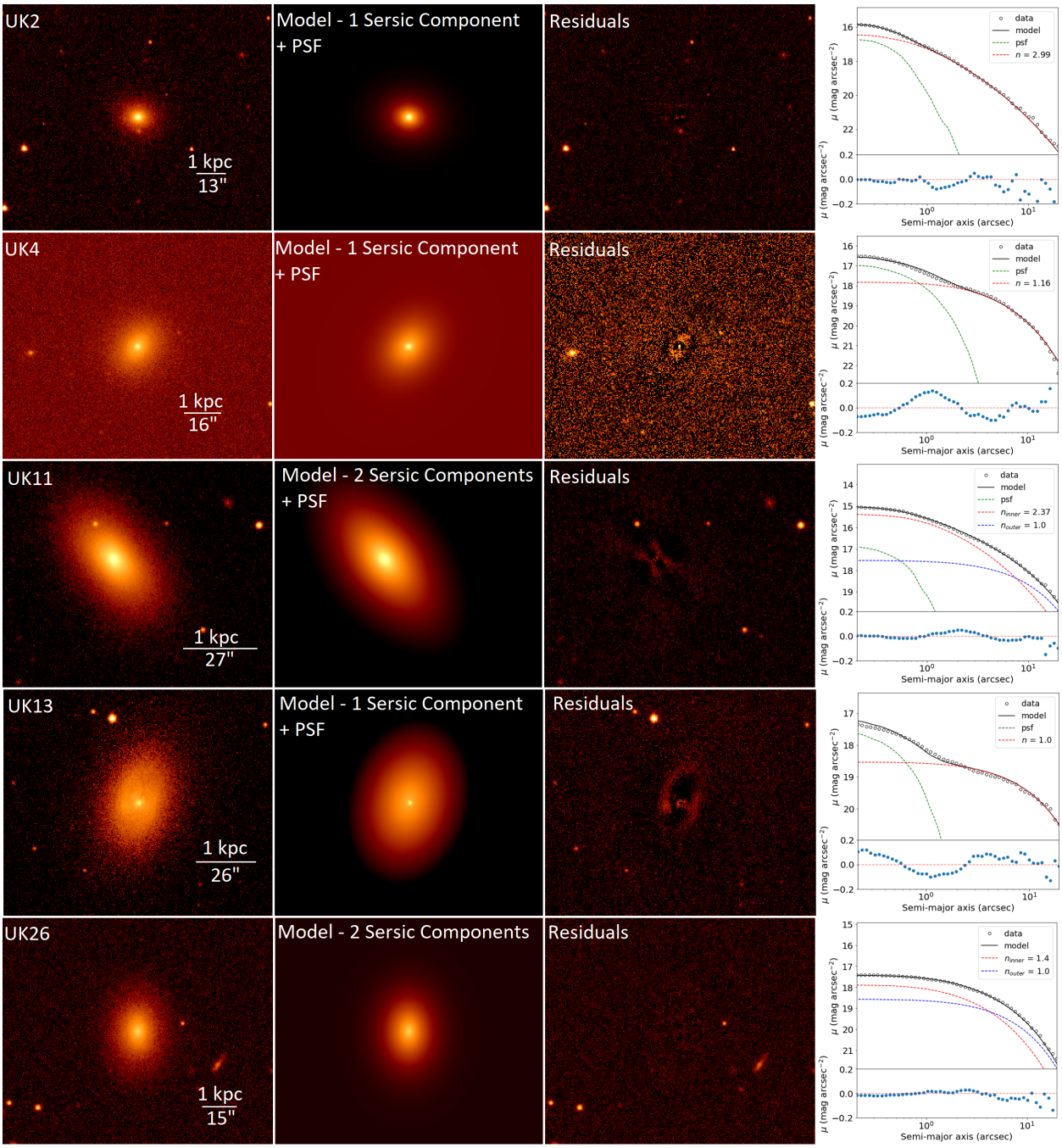

Figure 3.4: Left: UKIRT image, GALFIT model, and the residuals obtained by subtracting the GALFIT model from the image. Images are shown on a log scale, and the residuals are very stretched to show faint details. Right: Surface brightness profiles. Data are black circles and the model is shown as a black line; the GALFIT components are shown as dashed lines in color. The bottom panels contain the radial residuals.

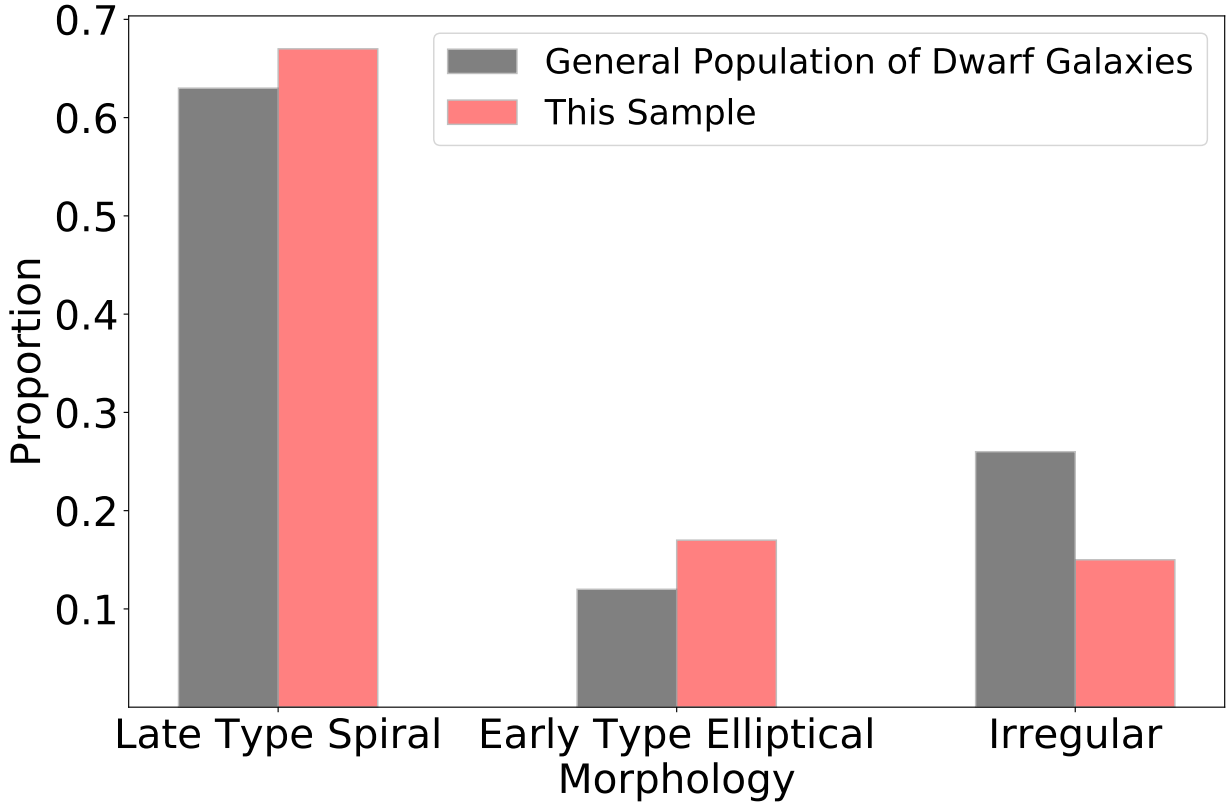

Figure 3.5: Morphologies of the galaxies analyzed in this work (red) compared to the general population of dwarfs in the same mass range ($10^9 < M_*/M_\odot < 10^{9.5}$) discussed in Reines (2022) (black). This demonstrates that our sample of non-AGN hosting dwarf galaxies provides a good representation of the general population of dwarf galaxies.

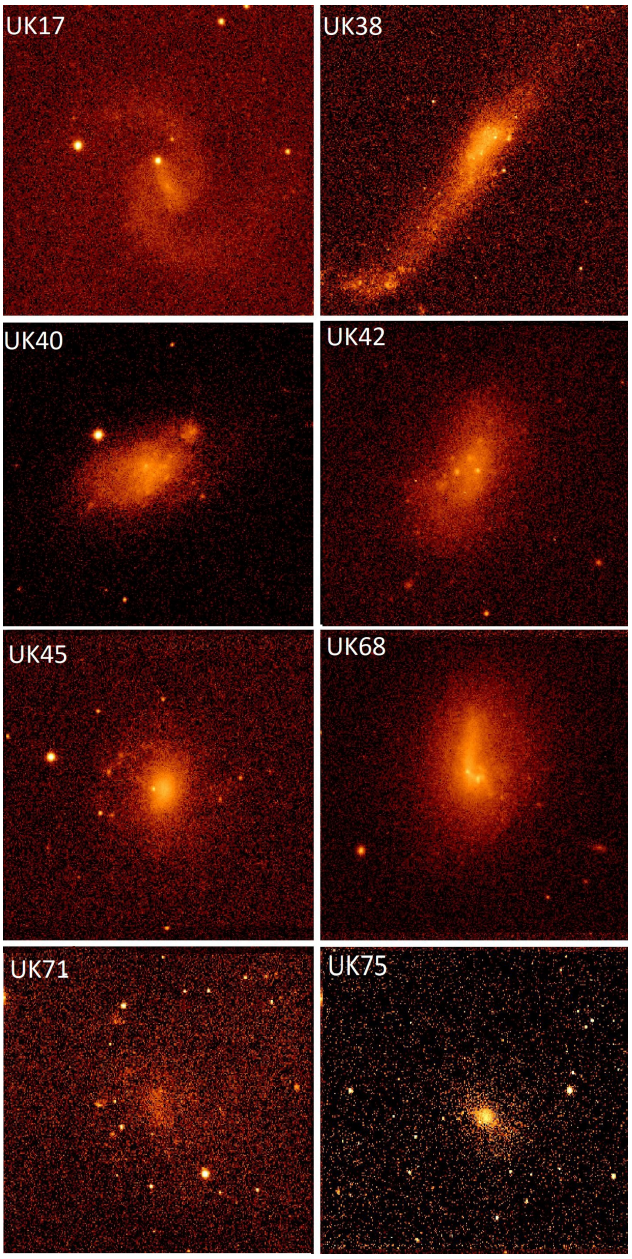

Figure 3.6: UKIRT images of the 8 irregular/disturbed galaxies in our sample. All images are shown on a log scale.

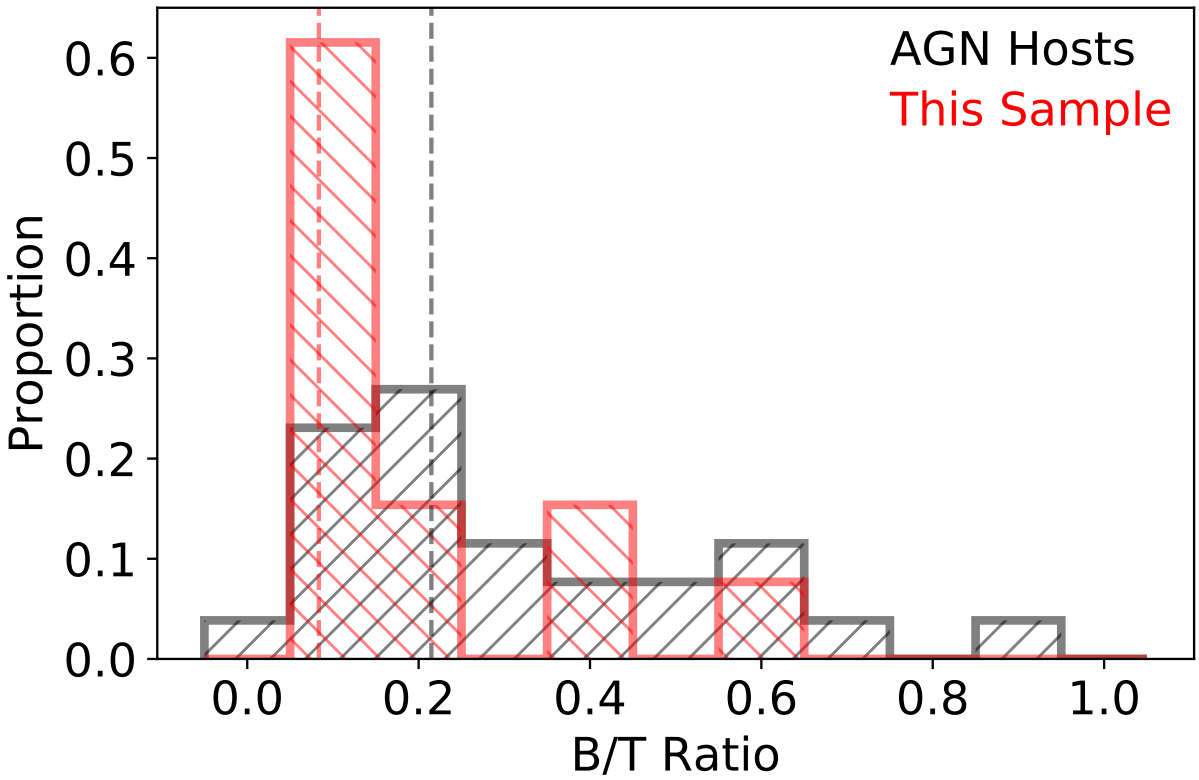

Figure 3.7: B/T ratios of the 2-component galaxies in this work (red) compared to the 2-component AGN hosts analyzed in Kimbrell et al. (2021) (black). Dashed vertical lines indicate median values.

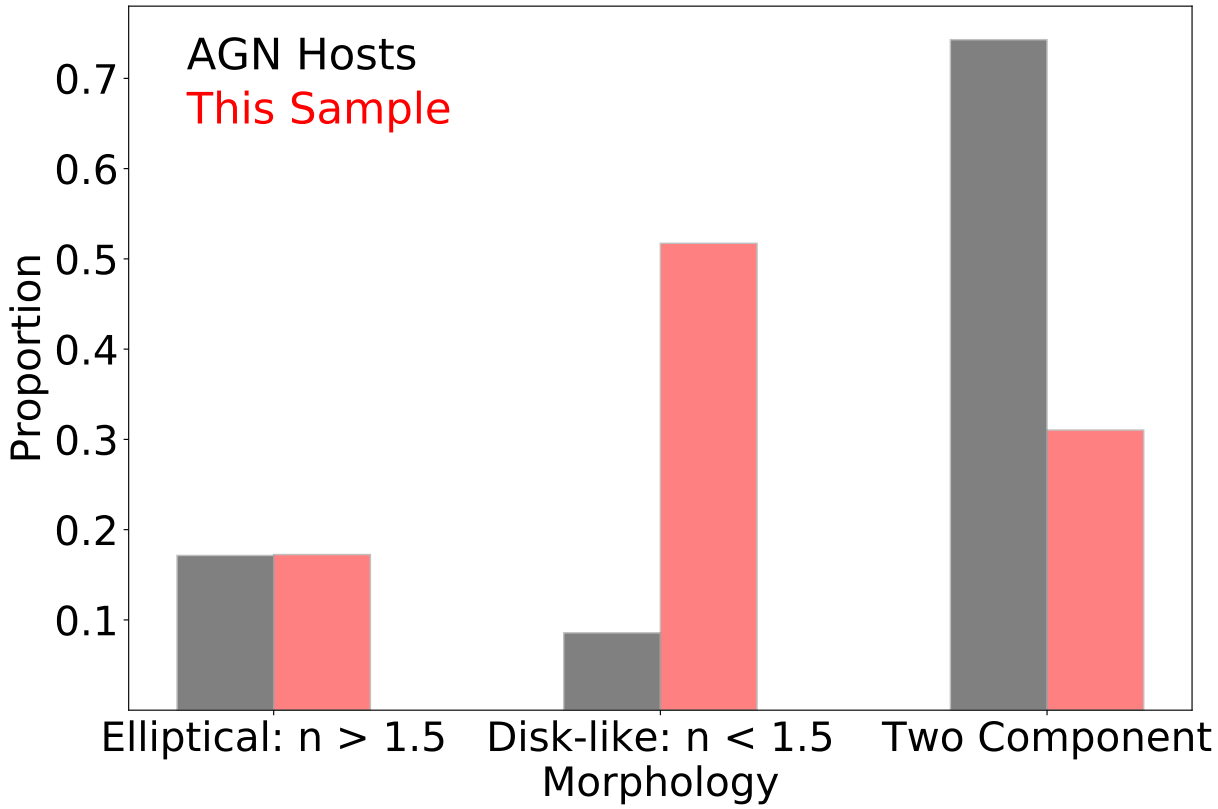

Figure 3.8: Morphologies of the galaxies analyzed in this work (red) compared to the AGN hosts analyzed in Kimbrell et al. (2021) (black). The first and second options indicate a single component galaxy best fit as a dwarf elliptical or a pure disk, respectively. The third option indicates a dwarf galaxy best fit with two Sèrsic components.

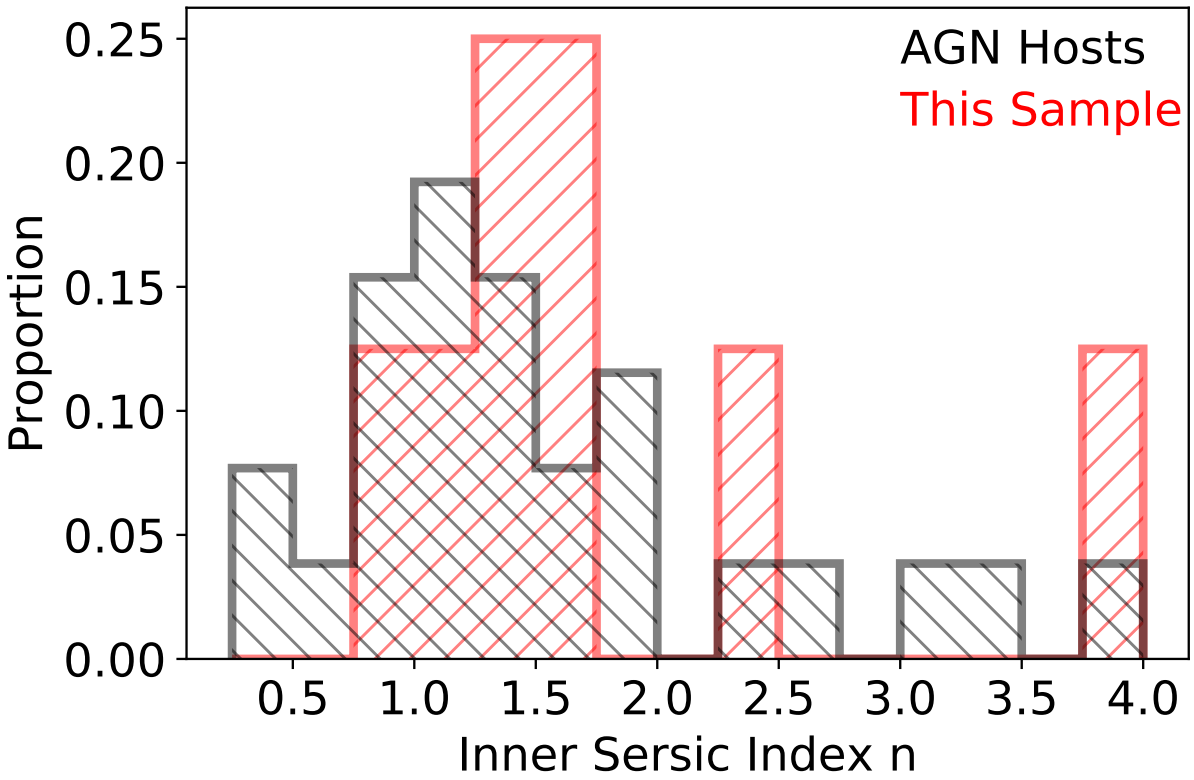

Figure 3.9: Inner Sèrsic indices of all 2-component galaxies studied in this work (red) compared to the AGN hosts analyzed in Kimbrell et al. (2021) (black)

.

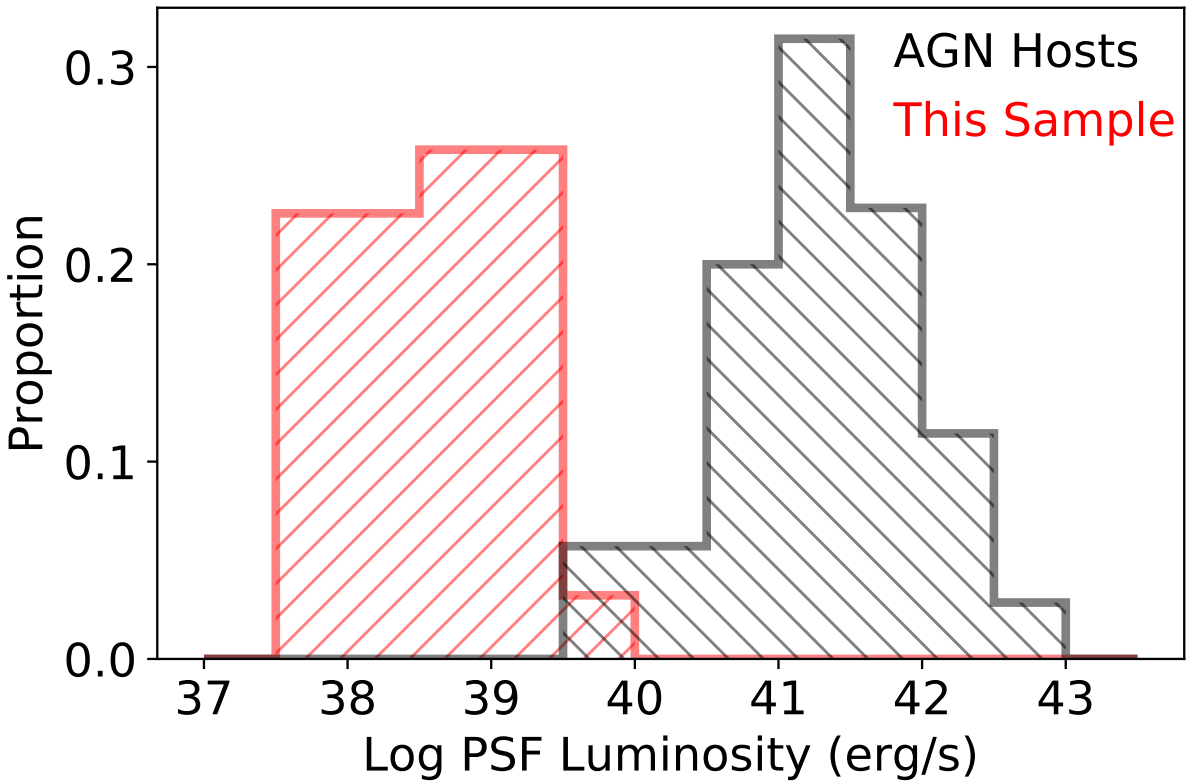

Figure 3.10: Log luminosity in ergs/s of the central PSF components of this sample (red) and the Kimbrell et al. (2021) sample of AGN hosts (black). The PSFs in the AGN hosts are, on average, more than two orders of magnitude more luminous than those in the non-AGN hosts, suggesting the PSFs in the AGN hosts are dominated by AGN light.

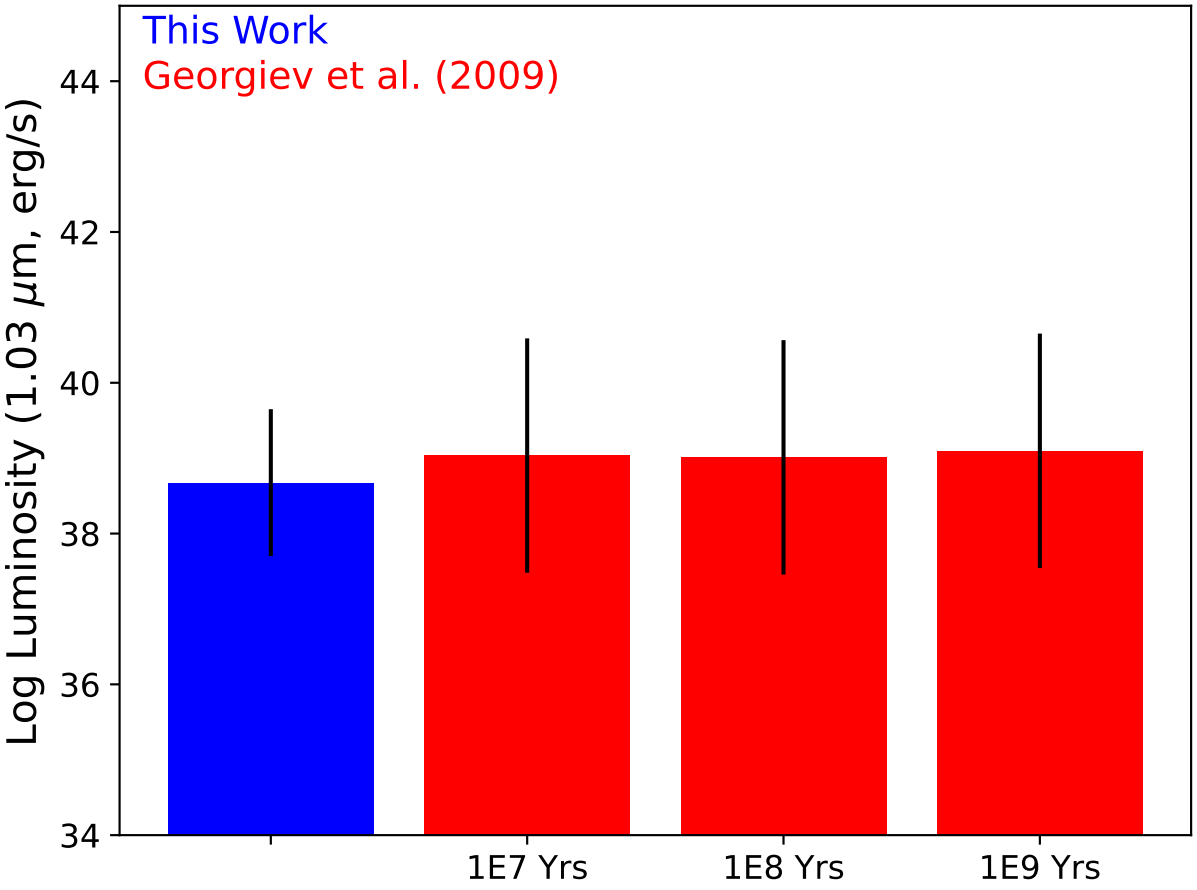

Figure 3.11: Median log luminosity in erg/s for PSFs of this sample (blue bar) and the median predicted 1.03μm luminosity for the PSFs of the Georgiev et al. (2009) sample (red bars) at varying ages. Black lines indicate the range from minimum to maximum luminosity.

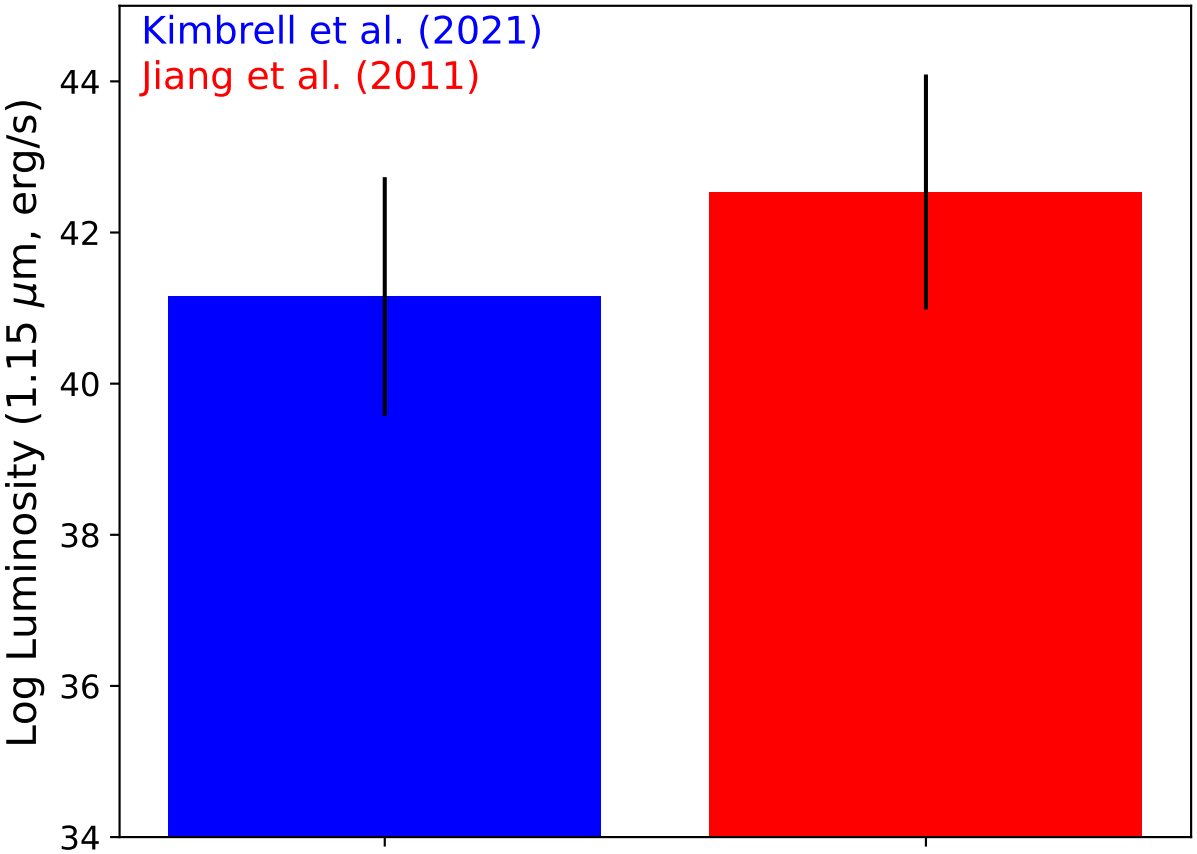

Figure 3.12: Median log luminosity in erg/s for the PSFs of the Kimbrell et al. (2021) (blue bar) and the median predicted $1.15\mu m$ luminosity for the PSFs of the Jiang et al. (2011) sample (red bar). Black lines indicate the range from minimum to maximum luminosity.

Appendix

Table 3.1. Fitting Results for Face-on Galaxies With Regular Morphologies

ID	Component	m_Y	n	R_e (kpc)	q	Additional Components
(1)	(2)	(3)	(4)	(5)	(6)	(7)
	PSF	22.95	-	-	-	
UK1	Sérsic	16.18	1.59	3.50	0.38	
	PSF	20.02	-	-	-	
UK2	Sérsic	16.50	2.99	0.43	0.83	
	PSF	18.99	-	-	-	
UK4	Sérsic	15.64	1.16	0.12	0.78	
	PSF	21.04	-	-	-	
UK6	Sérsic	16.27	1.45	0.61	0.94	
	PSF	20.44	-	-	-	
UK10	Sérsic	15.84	1.01	0.97	0.89	
	PSF	19.70	-	-	-	
UK11	Inner Sérsic	14.43	2.37	0.63	0.73	
	Outer Sérsic	14.79	1.00	1.11	0.47	
	PSF	21.43	-	-	-	
UK12	Sérsic	15.20	1.76	0.88	0.44	
	PSF	20.32	-	-	-	
UK13	Sérsic	15.03	0.96	1.37	0.72	

Table 3.1 (cont'd)

ID	Component	m_Y	n	R_e (kpc)	q	Additional Components
(1)	(2)	(3)	(4)	(5)	(6)	(7)
	PSF	21.94	-	-	-	
UK14	Sérsic	16.71	0.99	0.89	0.64	
	Inner Sérsic	18.33	3.87	0.31	0.91	
UK15	Outer Sérsic	15.38	1.00	2.13	0.89	
	PSF	21.09	-	-	-	
UK19	Sérsic	16.31	1.80	0.97	0.73	
	PSF	20.13	-	-	-	
UK22	Sérsic	14.89	1.38	1.35	0.88	
	PSF	23.36	-	-	-	-
UK23	Inner Sérsic	18.18	0.26	0.54	0.67	
	Outer Sérsic	15.58	1.00	3.20	0.62	
	PSF	24.13	-	-	-	
UK24	Sérsic	17.04	1.66	2.12	0.30	
	Inner Sérsic	16.65	1.37	0.42	0.64	
UK26	Outer Sérsic	15.98	1.00	0.65	0.77	

Table 3.1 (cont'd)

ID	Component	m_Y	n	R_e (kpc)	q	Additional Components
(1)	(2)	(3)	(4)	(5)	(6)	(7)
	PSF	23.01	-	-	-	
UK27	Sérsic	17.29	0.98	1.96	0.76	
	PSF	20.66	-	-	-	
UK28	Sérsic	15.60	0.93	1.60	0.82	
	PSF	23.37	-	-	-	
UK29	Sérsic	17.63	0.66	1.64	0.48	
	PSF	22.53	-	-	-	
UK32	Sérsic	18.34	0.81	0.84	0.52	
UK33	Sérsic	15.24	1.89	1.14	0.46	
	PSF	24.31	-	-	-	
UK34	Sérsic	16.05	1.40	2.69	0.40	Unmodeled Spiral Arms
	PSF	22.62	-	-	-	
UK43	Sérsic	14.93	0.79	3.09	0.72	
UK46	Sérsic	15.51	1.37	0.75	0.76	
UK47	Sérsic	16.56	1.15	0.92	0.89	

Table 3.1 (cont'd)

ID	Component	m_Y	n	R_e (kpc)	q	Additional Components
(1)	(2)	(3)	(4)	(5)	(6)	(7)
	PSF	21.50	-	-	-	
UK49	Sérsic	14.80	1.65	1.82	0.55	
	PSF	21.60	-	-	-	
UK50	Inner Sérsic	16.07	1.51	1.39	0.34	
	Outer Sérsic	14.70	1.00	2.54	0.46	
	PSF	19.65	-	-	-	
UK51	Sérsic	15.00	0.92	1.03	0.45	
	PSF	20.01	-	-	-	
UK52	Sérsic	14.34	1.29	1.64	0.56	
	PSF	19.10	-	-	-	
UK55	Sérsic	14.47	1.18	1.24	0.77	Unmodeled Spiral Arms
	PSF	23.50	-	-	-	
UK59	Inner Sérsic	16.79	1.03	0.85	0.57	
	Outer Sérsic	16.26	1.00	2.64	0.47	
	PSF	22.55	-	-	-	
UK60	Sérsic	15.35	0.47	1.36	0.55	

Table 3.1 (cont'd)

ID	Component	m_Y	n	R_e (kpc)	q	Additional Components
(1)	(2)	(3)	(4)	(5)	(6)	(7)
	PSF	21.71	-	-	-	
UK63	Sérsic	16.52	1.58	1.33	0.56	
UK64	Sérsic	16.67	1.59	0.89	0.82	
	PSF	21.48	-	-	-	
UK67	Inner Sérsic	15.74	1.47	0.87	0.90	Unmodeled Spiral Arms
	Outer Sérsic	12.92	1.00	4.93	0.82	
	PSF	19.82	-	-	-	
UK72	Sérsic	14.58	3.41	1.81	0.62	
	PSF	22.65	-	-	-	
UK74	Inner Sérsic	18.28	0.93	0.47	0.28	
	Outer Sérsic	16.11	1.00	1.24	0.95	
	Inner Sérsic	17.85	1.69	0.70	0.44	
UK77	Outer Sérsic	14.94	1.00	2.31	0.72	Unmodeled Spiral Arms
	PSF	22.29	-	-	-	
UK78	Sérsic	14.79	0.60	1.04	0.55	

Table 3.1 (cont'd)

ID	Component	m_Y	n	R_e (kpc)	q	Additional Components
(1)	(2)	(3)	(4)	(5)	(6)	(7)
UK82	Sérsic	16.12	1.07	3.00	0.38	

Note. — Column 1: Galaxy Identification Number. Column 2: Components in GALFIT model. Column 3: Total apparent magnitude in the UKIRT Y band. Column 4: Best fitting Sérsic index. Column 5: Best fitting effective radius, converted to kpc. Column 6: Best fitting axis ratio (b/a). Column 7: Any additional component included in the best-fit model.

Acknowledgements

A.E.R. gratefully acknowledges support for this paper provided by NASA through EPSCoR grant No. 80NSSC20M0231. This work is based in part on data obtained as part of the UKIRT Infrared Deep Sky Survey. We thank Chien Peng and the GALFIT help forum for helpful discussions on using GALFIT.

A LUMINOUS AGN IN THE DWARF-DWARF MERGER RGG 66

Contribution of Authors and Co-Authors

Manuscript in following chapter

Author: Seth Kimbrell

Contributions: Assisted in proposing for the data, analyzed the data, wrote the first draft of the manuscript.

Author: Amy Reines

Contributions: Proposed for the data, provided edits and comments on the manuscript, advised on performing scientific analysis.

Manuscript Information

Seth Kimbrell and Amy Reines

The Astrophysical Journal Letters

Status of Manuscript:
_X_ Prepared for submission to a peer-reviewed journal
____ Officially submitted to a peer-reviewed journal
____ Accepted by a peer-reviewed journal
____ Published in a peer-reviewed journal

IOP Publishing

Introduction

In recent years, massive black holes (BHs) in dwarf galaxies have been increasingly frequently discovered and studied (Reines, 2022; Birchall et al., 2020). These massive BHs give us an opportunity to study black holes which have not grown much compared to the supermassive black holes which are ubiquitous in more massive galaxies. At the same time, studying the demographics and morphologies of the hosts gives us a chance to understand the environments inhabited by these BHs. Since current capabilities do not allow us to directly view the early universe and observe the formation mechanisms of supermassive black holes, nearby dwarf galaxies hosting massive black holes give our best to chance put constraints on these formation channels (Volonteri et al., 2021; Greene et al., 2020; Inayoshi et al., 2020; Volonteri, 2010).

Dwarf galaxy mergers are expected to be common in the local universe, and they have been shown to trigger periods of intense star-formation, leading to the formation of blue compact dwarf galaxies (BCDs) (Paudel et al., 2018; Stierwalt et al., 2015). Active black holes in dwarf-dwarf mergers are an understudied area; the quintessential AGN in a dwarf-dwarf merger is MRK 709 (Kimbro et al., 2021; Reines et al., 2014), a system in which an AGN has been detected in one of the members of an early-stage merger. Mićić et al. (2023) reported the discovery of strong candidates for the first dual AGN in dwarf-dwarf mergers; systems in which the separation between the two AGNs are great enough to be resolvable. Because there has been no systematic search for AGNs in dwarf-dwarf mergers, and because the starburst triggered by the coalescence of merging galaxies obscures black holes at optical wavelengths (Pfeifle et al., 2019; Hopkins et al., 2008), detected AGNs in late-stage dwarf-dwarf mergers are exceptionally rare.

Kimbrell et al. (2021) studied the morphologies of dwarf galaxies which were selected by Reines et al. (2013) as likely candidates to host active massive black holes. Kimbrell et al.

(2023, IN PRODUCTION) performed a follow-up study on a sample of dwarf galaxies which had not been selected as AGN hosts and which were representative of the general population of nearby dwarf galaxies. In those, we found that the presence of a bulge inside a disk is a differentiating factor between AGN hosts and non-AGN hosts; however, both samples found a similar fraction of irregular/disturbed galaxies which could not be studied due to their morphology, including one late-stage merger system in the AGN hosts. The central point sources of light in Kimbrell et al. (2021) had luminosities consistent with AGNs, but the irregulars remained unstudied, and so the presence of an AGN in these could not be confirmed or ruled out.

While those studies were in the near-infrared, X-ray observations give us the opportunity to search for active massive black holes without much concern for the morphologies of their hosts. In this paper, we present follow-up X-ray observations of four of the irregular/disturbed dwarf galaxies studied in Kimbrell et al. (2021). We report the detection of a very bright X-ray AGN radiating close to its Eddington limit in the late-stage dwarf-dwarf merger RGG 66.

In Section 2 we describe the sample selection for this work. In Section 3 we detail the X-ray observations of our sample. We present our analysis and results in Section 4 and finish with conclusions in Section 5.

Sample of Dwarf Galaxies

Our sample of disturbed/irregular dwarf galaxies comes from Kimbrell et al. (2021). In that work, Kimbrell et al. (2021) analyzed *HST* imaging of a sample of 41 dwarf galaxies which were selected in Reines et al. (2013) as potential AGN hosts. Reines et al. (2013) used BPT emission line ratio diagnostics (Kewley et al., 2006; Kauffmann et al., 2003; Kewley et al., 2001) to select these potential hosts, among others. Of the 41 dwarf galaxies which were studied, six were classified as "irregular/disturbed," broadly referring to the galaxy

Table 4.1. Irregular/Disturbed Dwarf Galaxy Sample

ID	RGG ID	NSAID	obsid	RA (deg)	Dec (deg)	z colhead	r_{50} (kpc	log $M_*/M_\odot$	N_H (10^{20} cm^{-2})	Exposure time (ks)
(1)	(2)	(3)	(4)	(5)	(6)	(7)	(8)	(9)	(10)	(11)
1	RGG 40	82616	25281	117.12165	51.01453	0.0190	3.91	9.1	5.14	8.96
2	RGG 66	55081	25281, 26315	154.44624	39.53551	0.0540	0.40	9.0	1.39	34.87[a]
3	RGG 135	4308	25282	263.01240	59.98194	0.0291	3.06	9.4	3.46	19.79
4	RGG 136	5563	25283	359.03827	-0.40800	0.0256	5.32	9.2	3.40	15.87

Note. — Column 1: Galaxy identification number. Column 2: ID given in Reines et al. (2013) and Kimbrell et al. (2021). Column 3: NSA identification number. Column 4: Chandra Observation ID. Column 5: Right Ascension of the galaxy. Column 6: Declination of the galaxy. Column 7: Redshift taken from the NSA. Column 8: Petrosian 50% light radius, from the NSA. Column 9: Log total stellar mass. Column 10: Galactic neutral hydrogen column density. Column 11: Exposure time in kiloseconds.

[a]RGG 66 was observed twice - one observation of 18.79 ks and one of 16.08 ks, and we merged the observations for analysis

being too asymmetric to be modeled by axisymmetric models. Of those six, three appear to be Magellanic type dwarf irregulars, while two exhibit clear signatures of interactions or mergers; the final galaxy possessed internal spiral structure that made modeling difficult, but it did not fall into either the Magellanic-type irregular or disturbed category.

We excluded the galaxy with an internal spiral, as well as one of the Magellanic type irregulars (RGG 5) which had previously been observed with no X-ray source detected. The four remaining galaxies were three truly irregular dwarf galaxies (RGG 40, RGG 135, and RGG 136) and one late-stage merger system (RGG 66); all were identified as Seyferts in the [OIII/Hβ] vs. [SII]/Hα diagnostic, and all fell into the Composite region of the [OIII]/Hβ vs. [NII]/Hα diagnostic (Figure 4.1). These four made up our sample of irregular galaxies which were observed by Chandra. Our sample and its properties are shown in Table 4.1. Distances are obtained from the NASA Sloan Atlas assuming $H_0 = 73$. Galactic neutral hydrogen column density comes from Dickey & Lockman (1990) and is retrieved from Chandra's

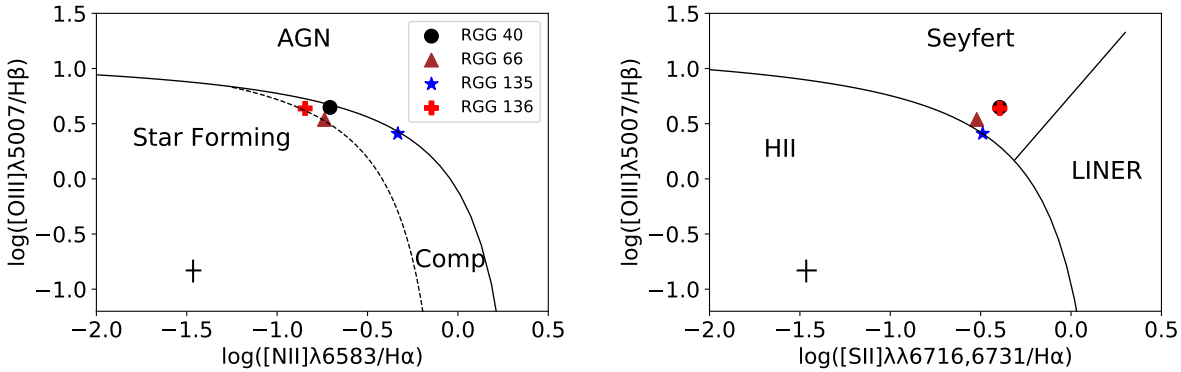

Figure 4.1: Narrow emission line diagnostic diagrams showing the location of our sample of irregular dwarf galaxies, which exhibit optical signatures of active massive BHs (Reines et al., 2013) and were analyzed by Kimbrell et al. (2021). Left: [OIII]/Hβ vs. [NII]/Hα diagnostic diagram. The solid line shows the "maximum starburst" line from stellar photoionization models (Kewley et al., 2001). The dashed line is an empirical separation between galaxies that show some contribution from AGN and galaxies dominated by star formation (Kauffmann et al., 2003). Composite galaxies fall between the dashed and solid lines, and likely indicate contributions from both an AGN and star formation. Right: [OIII]/Hβ vs. [SII]/Hα diagnostic diagram, using the classifications from Kewley et al. (2006). Typical errors are shown in the lower left corners.

Colden Galactic Neutral Hydrogen Density Calculator[1].

Chandra X-ray Observations

We obtained Chandra observations of our four irregular dwarf galaxies taken between November 12, 2021 and January 19, 2023. One galaxy, RGG 66 (ID 2 in Table 4.1), had its observations split into two separate observations; we merged these as part of our analysis, which we discuss in Section 4.

Using version 4.14 of the Chandra Interactive Analysis of Observations software (CIAO) (Fruscione et al., 2006), we reprocessed our data, utilizing the chandra_repro script to follow

[1]https://cxc.harvard.edu/toolkit/colden.jsp

the recommended reprocessing steps[2]. We applied Chandra calibration files (CALDB 4.9.8) for reprocessing and created new event files which were used in our analysis.

We attempted to align our images' astrometry to the SDSS reference frame. We ran the CIAO wavdetect routine[3] on each filtered image, ignoring sources that lie inside the galaxy region of each image. This routine correlates each image with "Mexican Hat" wavelets of varying scale sizes; we use wavelets of size 1.0, 1.4, 2.0, 2.8 and 4.0 pixels for our analysis. We set our significance threshold to be 10^{-6}; this is the threshold at which we should expect roughly one strong background fluctuation to be detected as a source across the entire chip. If any sources were found, we matched them to existing SDSS detections; however, no matching sources were located for our images, and so astrometry correction could not be performed.

Analysis and Results

Searching For Hard X-ray Sources

With our observations taken, we searched for X-ray point sources which could correspond to active massive BHs. We began by filtering our images from 2 to 7 keV and running wavdetect. For our point-spread function map, we created a PSF map using the CIAO fluximage routine with an enclosed energy fraction of 39% at 4 keV. Once wavdetect identified point sources, we filtered by location in the image and only accepted X-ray sources which are within $3r_{50}$ of the center of the galaxy.

A Luminous X-ray Source in RGG 66

Using wavdetect, we detected an X-ray source in each of the two observations of RGG 66. To find the net counts detected for each observation, we drew a circular aperture centered on each detected source with a radius that allows the aperture to enclose 90% of the energy

[2]https://cxc.cfa.harvard.edu/ciao/ahelp/chandra_repro.html
[3]https://cxc.cfa.harvard.edu/ciao/ahelp/wavdetect.html

at 4.5 keV. We then estimated the number of background counts by creating an annulus co-located with the source, with an inner radius equal to the radius of the source aperture and outer radius equal to 12 times the radius of the source aperture. We corrected for the 90% enclosed energy aperture and subtracted the background counts from the source counts to find the net counts. We found net counts of 240.01 ± 27.43 for the first observation and net counts of 209.52 ± 25.63 for the second.

Spectral Analysis Given the large number of counts, we were able to perform spectral analysis on the data for RGG 66. We used the specextract CIAO tool[4] to extract a spectrum from each observation, then merged each spectrum using the combine_spectra CIAO tool[5] (bottom panel of Figure 4.2). We grouped our counts in bins of 25 then used the Sherpa fitting package to model the spectrum with an absorbed power-law model, including a galactic absorption term $n_{H,gal}$ and an intrinsic absorption term $n_{H,target}$. We used Chandra's Colden to calculate the galactic neutral hydrogen column density and froze the value of $n_{H,gal}$ to the calculated value of $1.39 \times 10^{20}\mathrm{cm}^{-2}$. We found that the spectrum was best fit by an absorbed power law with photon index $\Gamma = 2.39 \pm 0.15$ and intrinsic absorption of $n_{H,target} = (1.084 \pm 1.767) \times 10^{21}\mathrm{cm}^{-2}$.

Merging RGG 66 Observations We ran the CIAO merge_obs process[6] on the two observations of RGG 66 to create a new merged event file. We then ran wavdetect on the merged event file from merge_obs, using the same wavdetect settings as on the individual files. At this point, we found an offset of $\sim 0\farcs65$ (~ 1.3 pixels) between the source regions in the images. As this is too much of an offset to trust the results of analysis, we followed the process detailed in the CIAO threads[7] to correct this offset, shifting observation 26315

[4]https://cxc.cfa.harvard.edu/ciao/ahelp/specextract.html
[5]https://cxc.cfa.harvard.edu/ciao/ahelp/combine_spectra.html
[6]https://cxc.cfa.harvard.edu/ciao/ahelp/merge_obs.html
[7]https://cxc.cfa.harvard.edu/ciao/threads/fluxes_multiobi/

to match 25281.

With relative astrometry corrected, we confirmed that the detected source was still within $3r_{50}$ of the galaxy's center. We created a source aperture for this merged file by averaging the 90% enclosed energy radii for each individual event file, centered on the source detected in the merged file. We created the background annulus with an inner radius equal to the radius of the source aperture and an outer radius equal to twelve times the source aperture radius.

We then ran srcflux[8] on the merged product. The routine takes as an input a stack of the individual event files and outputs properties based on the merged product. We used the same srcflux settings that we did for the individual observations: an absorbed power law spectral model with intrinsic absorption modeled and galactic absorption frozen to the Dickey & Lockman (1990) absorption maps. The results of running srcflux on this stack of merged event files are the reported values in Column 7 of Table 4.2.

Because our source has net counts $\gg 10$, we neglected the background when calculating the errors in net counts and use the 90% confidence intervals from Gehrels (1986). For error in position, we used the relations from Hong et al. (2005), which depends on the offset from the aimpoint, D, and the net count number c_n:

$$\begin{aligned} P_{err,\mathrm{arcmin}} = 0\farcs25 + \frac{0\farcs1}{\log(c_n+1)}\left[1+\frac{1}{\log(c_n+1)}\right] \\ +0\farcs03\left[\frac{D}{\log(c_n+2)}\right]^2 + 0\farcs0006\left[\frac{D}{\log(c_n+3)}\right]^4 \end{aligned} \tag{4.1}$$

with an upper limit of the radius of the aperture which encloses 95% of the source's energy at 1.5 keV. We note that, outside of this statistical error, an error could arise from being unable to match astrometry to the SDSS frame. In the worst case scenario, this could lead

[8]https://cxc.cfa.harvard.edu/ciao/ahelp/srcflux.html

to an error of as much as $2\farcs3$, but we expect this error to be $< 1''$[9].

Estimating Mass and Eddington Ratio Since the X-ray luminosity of RGG 66 strongly supports the presence of an AGN, we next examine possible parameters for the BH. We start with the Reines & Volonteri (2015) relation between BH mass and galactic stellar mass:

$$\log(M_{\rm BH}/M_\odot) = \alpha + \beta \log(M_{\rm stellar}/10^{11} M_\odot) \tag{4.2}$$

with $\alpha = 7.45 \pm 0.08$ and $\beta = 1.05 \pm 0.11$. Applying this relation to RGG 66, we predict a BH of mass $10^{5.37} M_\odot$. We proceed to estimate the Eddington ratio of a BH of this mass and luminosity. We first find the bolometric correction from hard X-ray luminosity to bolometric luminosity, such that $L_{bolo} = \kappa L_{2-10keV}$. We use the relation derived in Duras et al. (2020):

$$\kappa(L_x) = a \left[1 + \left(\frac{log(L_x/L_\odot)}{b} \right)^c \right] \tag{4.3}$$

with best-fit values of $a = 15.33 \pm 0.06$, $b = 11.48 \pm 0.01$, and $c = 16.20 \pm 0.16$. Using this relation and our measured X-ray luminosity, we estimate a bolometric correction of $\kappa \sim 15.7$. We then find the Eddington ratio:

$$f_{Edd} = \frac{\kappa \times (L_{2-10keV})}{L_{Edd}} \tag{4.4}$$

where

$$L_{Edd} \sim 1.26 \times 10^{38} \left(\frac{M_{\rm BH}}{M_\odot} \right) \tag{4.5}$$

We find that this BH in RGG 66 with a hard X-ray luminosity of $10^{42.18}$ erg/s is radiating at an Eddington ratio of ~ 0.81.

[9] https://cxc.harvard.edu/cal/ASPECT/celmon/

Comparison to Other Low-Mass AGNs Next, we compare the BH found in RGG 66 to other low-mass AGNs in dwarf galaxies. Two of the most well-studied dwarf galaxies hosting AGNs are NGC 4395 (Filippenko & Ho, 2003) and Pox 52 (Barth et al., 2004). NGC 4395 is variable in the X-ray (Moran et al., 2005; Lira et al., 1999); measurements of its hard X-ray luminosity have generally found $L_{2-10\mathrm{keV}}$ on the order of 10^{40}erg/s (Dewangan et al., 2008; Vaughan et al., 2005; Moran et al., 2005). Pox 52 was found by Dewangan et al. (2008) to have a 2-10 keV luminosity of $\sim 10^{41.61}$ using XMM-Newton observations.

Latimer et al. (2019) performed a combined X-ray and radio search among blue compact dwarf galaxies (BCDs) and located one candidate AGN, in Haro 9. That AGN candidate had a 2-10 keV luminosity of $L_{2-10\mathrm{keV}} = 10^{39.4}$erg/s. In a later work, Latimer et al. (2021) performed an X-ray study of WISE-selected AGN candidates in dwarf galaxies. The five galaxies which they identified as having strong evidence for an accreting central BH had hard X-ray luminosities in the range $10^{40.1} - 10^{41.9}$erg/s, with a median of $10^{40.3}$erg/s.

Birchall et al. (2020) presented a study of 61 X-ray selected AGNs in nearby ($z \leq 0.25$) dwarf galaxies with X-ray luminosities taken in the 2-12 keV band. RGG 66's measured X-ray luminosity of $10^{42.18}$ erg/s is at the very high end of the range measured there; Birchall et al. (2020) found a maximum X-ray luminosity of 5.35×10^{42} erg/s, with the modal group between 5×10^{39} and 1×10^{40} erg/s (see Figure 4 of that work). In fact, RGG 66 has a higher hard X-ray luminosity than all but one dwarf galaxy reported in Table B1 of that work.

In fact, the BHs in dwarf galaxies which are most similar to RGG 66 are those found in Mićić et al. (2023). In that work, two dwarf-dwarf merger systems were identified in which candidate dual AGNs - AGNs which are separated by enough to be resolvable as two separate sources - were identified. In particular, the AGNs in the galaxies that work names Elstir and Vinteuil have broad-band luminosities of $\log(L_{0.5-8\mathrm{keV}}) = 41.96$ and 42.71. Using the spectrum of RGG 66, we find a broad-band of luminosity of $\log(L_{0.5-8\mathrm{keV}}) = 42.23$, comparable to those found by Mićić et al. (2023).

Confirming that RGG 66 is a Dwarf-Dwarf Merger We examine the properties of RGG 66 using the NASA-Sloan Atlas (NSA) to confirm its classification as a dwarf-dwarf merger. To begin, its Petrosian 50% light radius of $r_{50} = 0.4$ kpc speaks to a compact system. We also compare the absolute magnitudes of RGG 66 and compare them to those found in literature for known dwarf galaxies. As previously mentioned, the prototypical dwarf-dwarf merger system is MRK 709, which has absolute g, r and i band magnitudes of ~ -20. For comparison, RGG 66 has absolute magnitudes of $\sim -18.2, -18.7$ and -18.5 in the g, r and i band. The g band magnitude of RGG 66 is comparable with the rest of the Reines et al. (2013) sample of dwarf galaxies from which it was drawn; these parameters allow us to confidently describe RGG 66 as a dwarf.

We use visual inspection of RGG 66 in classifying it as a merger. The *HST* image (top panel of Figure 4.2) shows tidal features running left to right in the image. These tidal tails are indicators of a galaxy merger/interaction. The presence of these features without a companion galaxy in the vicinity leads us to classify RGG 66 as a late-stage merger at the point of coalescence.

Placing Upper Limits on Non-Detections

For the other three galaxies, in which no sources were detected by wavdetect, we placed an artificial source region at the center of the galaxy and ran srcflux on this region. We took an absorbed power-law spectral model for the source with a photon index $\Gamma = 1.8$, a typical value for low-luminosity AGN (Latimer et al., 2021, 2019; Ho, 2009, 2008). Doing this gave us an upper limit on the brightness of a source that would not be detected in our imaging. We summarize our findings and upper limits in Table 4.2, and we show the location of the X-ray source in RGG 66 along with the SDSS fibre used to identify RGG 66 as a possible AGN host by Reines et al. (2013) in the top panel of Figure 4.2.

Star Formation and Expected X-ray Luminosity

We next used far UV and IR luminosity measurements to estimate the star formation rate for our irregular dwarf galaxies:

$$L(FUV)_{corr} = L(FUV)_{obs} + 3.89L(25\mu m) \tag{4.6}$$

$$\log\dot{M}(\mathrm{M}_{\odot}\mathrm{yr}^{-1}) = \log L(FUV_{corr}) - 43.35 \tag{4.7}$$

(Kennicutt & Evans, 2012; Hao et al., 2011). While the Hao et al. (2011) sample utilized $25\mu m$ luminosities using the Infrared Astronomical Satellite (*IRAS*), our galaxies have not all been observed by *IRAS*. Instead, we use $22\mu m$ observations from the Wide-field Infrared Explorer (*WISE*). The luminosity at $22\mu m$ via *WISE* is expected to be similar to the 25 μm luminosity via *IRAS* (see Jarrett et al. (2013)). All of our galaxies have been observed by the Galaxy Evolution Explorer (*GALEX*) and FUV luminosities are obtained via the NASA Sloan Atlas. Applying the above relations, we find the specific star formation rates to range from $-10.45 \leq \log(\frac{\mathrm{SFR}}{\mathrm{M}_*}) \leq -9.46$.

At these specific star formation rates, we expect to see contribution to X-ray luminosity from both high-mass X-ray binaries (HMXB), which scale with star formation rate, and low-mass X-ray binaries (LMXB), which scale with galaxy mass (Mineo et al., 2012; Lehmer et al., 2010; Colbert et al., 2004; Grimm et al., 2003). For the detected source in RGG 66 and the upper limits on non-detections for the other galaxies, we use the following relation from Lehmer et al. (2010):

$$L_{\mathrm{HX}}^{\mathrm{gal}} = \alpha M_* + \beta \mathrm{SFR} \tag{4.8}$$

where $\alpha = (9.05 \pm 0.37) \times 10^{28}$ ergs s$^{-1} M_{\odot}^{-1}$ and $\beta = (1.62 \pm 0.22) \times 10^{39}$ ergs s$^{-1}(M_{\odot}\mathrm{yr}^{-1})^{-1}$. We show the predicted hard X-ray luminosity from X-ray binaries in Column 8 of Table 4.2.

We find at the low estimated star formation rate, the three galaxies without detections could have an X-ray source brighter than the Lehmer et al. (2010) prediction for XRB X-ray luminosity without being detected; we cannot conclusively rule out the existence of an AGN in these galaxies. However, the source detected in RGG 66 cannot be explained by XRB X-ray emission and is likely to be an AGN, having a luminosity ~ 1000 times brighter than predicted by Lehmer et al. (2010).

Table 4.2. Hard X-ray Sources

Name	RA (deg)	Dec (deg)	Pos. Error (arcsec)	Net Counts	$F_{2-10keV}$ (10^{-15} erg s^{-1} cm^{-2})	log $L_{2-10keV}$ (erg s^{-1})	log $L_{2-10keV,XRB}$ (erg s^{-1})
(1)	(2)	(3)	(4)	(5)	(6)	(7)	(8)
RGG 66	154.446334	39.535563	0.31	457.97 ± 37.73	254.82	42.18	38.81
RGG 40	-	-	-	-	< 5.76	< 39.65	38.47
RGG 135	-	-	-	-	< 2.59	< 39.67	38.57
RGG 136	-	-	-	-	< 3.22	< 39.65	38.71

Note. — Column 1: Galaxy ID. Column 2: Right Ascension of the source. Column 3: Declination of the source. Column 4: 95% error in position. Column 5: Aperture-corrected net counts in the 2-7 keV range. Column 6: Absorption-corrected flux. Column 7: Absorption-corrected log luminosity. Column 8: Predicted log luminosity from X-ray binaries, given the galaxy's mass and star formation rate.

Conclusions

We have presented Chandra imaging of four low-mass irregular dwarf galaxies which were optically selected (via BPT diagrams) as hosts of active massive black holes (Kimbrell et al., 2021; Reines et al., 2013). We have detected strong evidence for the presence of an AGN in the late-stage dwarf-dwarf merger RGG 66. Since dwarf-dwarf mergers are a poorly-studied system with conditions which obscure AGN, this is one of the first AGNs detected in such a late-stage merger of dwarf galaxies.

1. The source detected in RGG 66 is likely to be an AGN, as the observed hard X-ray luminosity of $10^{42.18}$ erg s^{-1} is nearly three orders of magnitude higher than that expected by X-ray binaries given the star formation rate estimated for RGG 66.

2. Using the BH mass - stellar mass relation of Reines & Volonteri (2015), we predict a black hole of mass $M_{\rm BH} = 10^{5.37} M_{\odot}$ residing in this dwarf-dwarf merger.

3. The BH living in RGG 66 has an estimated Eddington ratio $f_{Edd} \sim 0.81$.

Further studies of this system could provide the opportunity to study a massive BH in a system which is expected to have been common in the early universe.

Acknowledgements

The authors thank Lily Latimer for being a constant source of assistance with X-ray analysis. This work has made use of software provided by the Chandra X-ray Center (CXC) in the application packages CIAO and Sherpa.

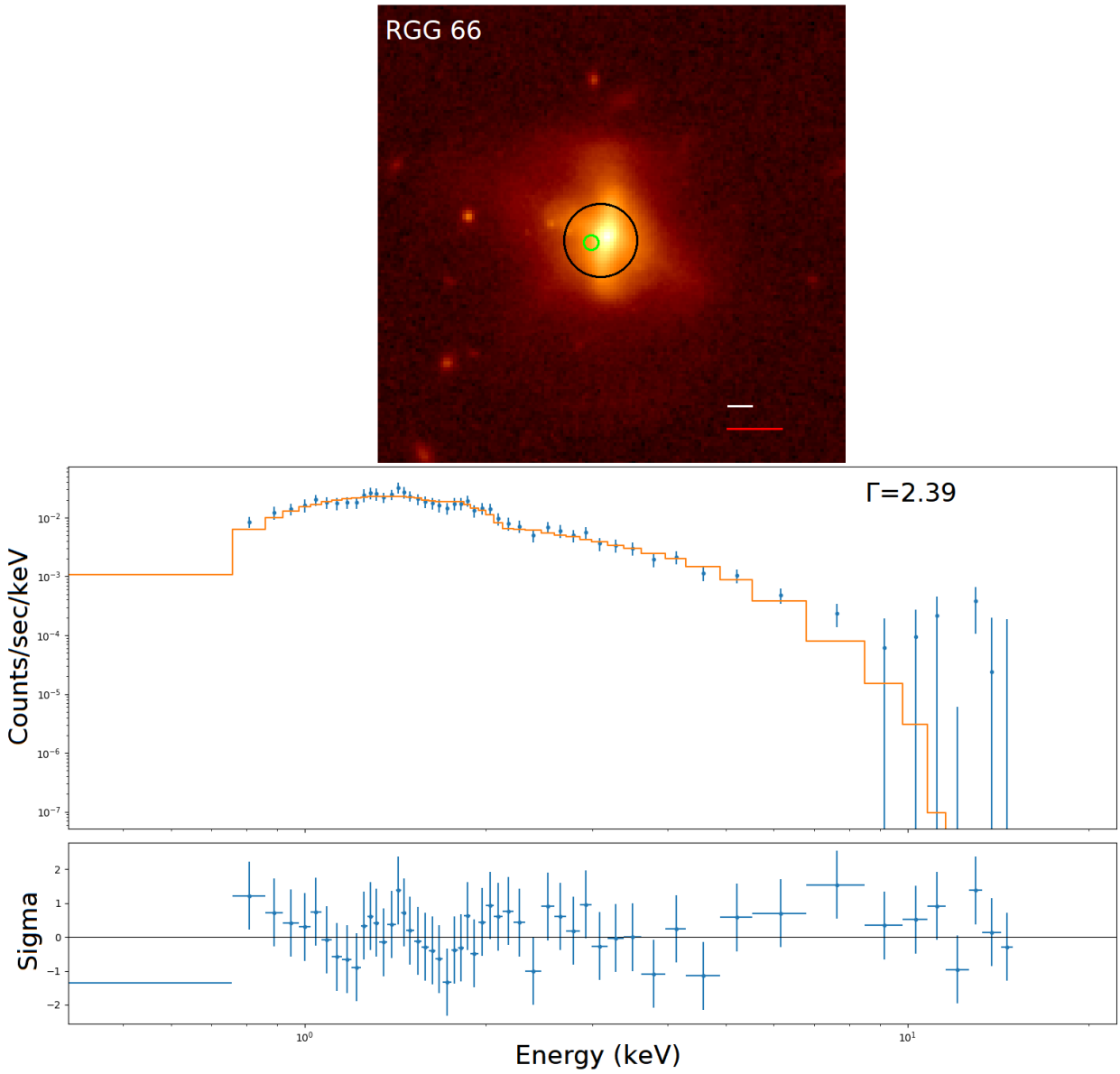

Figure 4.2: **Top:** Infrared *HST* image of RG66 shown on a log scale. The black circle shows the SDSS spectroscopic fibre, while the smaller green circle shows the position and error in position of the detected X-ray source. The expected error of 1″from the astrometry is shown in a white bar in the bottom right, and the maximum error of 2.″3 from the astrometry is shown in a red bar in the bottom right. **Bottom:** X-ray spectrum of RGG 66, with a best-fit photon index of $\Gamma = 2.39$ and counts grouped in bins of 25.

CONCLUSION

Finally, I summarize the work presented throughout this dissertation and look to the future.

In Chapter 2, I presented a morphological study of 41 dwarf galaxies selected as candidate AGN hosts using infrared *HST* imaging. These candidates were identified by Reines et al. (2013) using optical emission-line diagnostics. I performed a 2-dimensional bulge-disk decomposition to study the morphologies of these galaxies; I found that the vast majority of these dwarf galaxies hosting AGNs are dominated by a disk, but most have some (pseudo)bulge component as well. I also placed point sources of light in the centers of these galaxies and found luminosities consistent with AGN light. 15% of this sample was made up of irregular/disturbed galaxies which could not be well-modeled using the techniques of this work and which would later be imaged in the X-ray.

In Chapter 3, I presented the results of an identical study of a sample of dwarf galaxies with no evidence for an AGN. I started by constructing a sample of galaxies which spanned the same range of mass and color as the AGN hosts in Chapter 2. This sample had a distance cut imposed to ensure consistent physical resolutions between the two samples. I removed any galaxies which were identified as possible AGN hosts in other works, and I performed a bulge-disk decomposition on this sample following the same steps as in Chapter 2, for consistency. I found that the dwarfs which do not host AGNs were much less likely to have both a bulge and a disk than the AGN hosts. I also found that many of these galaxies were also best fit by a model including a point source of light in the center, but the luminosities of these were far more consistent with nuclear star clusters than AGNs.

While the results of this comparison already speak to a difference in structure between AGN hosts and non-AGN hosts, future research on this can go further to differentiate the two populations. The James Webb Space Telescope (*JWST*) will provide higher resolution

infrared imaging, which will allow us to probe the structures of dwarf galaxies at signifcantly greater distances. This will allow for a larger and larger set of galaxies to be targeted for morphological studies as AGN hosts are identified.

Identifying dwarf galaxies which host massive black holes is also a rapidly growing field. Hundreds of dwarf galaxies have been identified as AGN hosts using optical variability, rather than emission-line diagnostics. In addition, the Laser Interferometer Space Antenna (LISA) promises exciting results. Dwarf galaxies are the most common type of galaxy in the universe, and black hole mergers stemming from the mergers of low-mass galaxies will be observable by LISA. This is an environment that is under-represented in our current knowledge of AGNs in dwarf galaxies; mergers (especially at the latest stages) tend to obscure the AGNs at optical wavelengths. In addition, the coalescence stage of a merger is marked by a burst of star formation, which can overpower low-mass AGN emission in commonly-used diagnostic exams. Gravitational wave astronomy will give us the ability to counteract these difficulties, and increase the sample of known massive black holes in dwarf galaxies undergoing mergers.

I presented one of the few AGNs found in a dwarf-dwarf merger in Chapter 4. There, I analyzed Chandra X-ray Observatory imaging of four of the irregular/disturbed galaxies from Chapter 2, which were selected via emission-line diagnostics as candidates to host active massive black holes. I did not detect X-ray emission in three of the four; however, I showed that an AGN could still reside in those galaxies while radiating fewer X-rays than the data would have detected. The fourth galaxy was a late-stage dwarf-dwarf merger named RGG66; in this system, I detected significant X-ray emission, with a luminosity of $L_{2-10keV} = 10^{42.18}$ erg/s. The X-ray luminosity observed, combined with scaling relations between black hole and galaxy mass, predict a black hole with a mass of $10^{5.37} M_{\odot}$ radiating at an Eddington ratio of 0.81. Not only is this black hole a rarity for its environment, but it is radiating at an extremely high rate.

In summary, the study of dwarf galaxies which host active massive black holes is a

very young field which provides an exciting chance to constrain the formation channels that led to the SMBHs which we know are ubiquitious in massive galaxies. Studies of the hosts of these active massive black holes allow us to study the environment in which these AGN reside. As telescope technology continues to improve, more and more of these systems will be discovered, and we can continue to learn about black hole formation mechanisms.

REFERENCES CITED

Aird, J., Comastri, A., & Topical Panel 2. 1. 2015, in Exploring the Hot and Energetic Universe: The first scientific conference dedicated to the Athena X-ray observatory, 24

Akaike, H. 1974, IEEE Transactions on Automatic Control, 19, 716

Anglés-Alcázar, D., Faucher-Giguère, C.-A., Quataert, E., et al. 2017, , 472, L109

Antonini, F., Gieles, M., & Gualandris, A. 2019, , 486, 5008

Bañados, E., Venemans, B. P., Mazzucchelli, C., et al. 2018, , 553, 473

Baldassare, V. F., Geha, M., & Greene, J. 2020, , 896, 10

Baldassare, V. F., Reines, A. E., Gallo, E., & Greene, J. E. 2015, , 809, L14

Baldassare, V. F., Reines, A. E., Gallo, E., & Greene, J. E. 2017, The Astrophysical Journal, 850, doi:10.3847/1538-4357/aa9067

Baldassare, V. F., Reines, A. E., Gallo, E., & Greene, J. E. 2017, , 836, 20

Baldry, I. K., Driver, S. P., Loveday, J., et al. 2012, , 421, 621

Baldwin, J. A., Phillips, M. M., & Terlevich, R. 1981, , 93, 5

Barth, A. J., Ho, L. C., Rutledge, R. E., & Sargent, W. L. W. 2004, , 607, 90

Begelman, M. C., & Rees, M. J. 1978, , 185, 847

Birchall, K. L., Watson, M. G., & Aird, J. 2020, , 492, 2268

Blanton, M. R., Kazin, E., Muna, D., Weaver, B. A., & Price-Whelan, A. 2011, , 142, 31

Blanton, M. R., & Roweis, S. 2007, , 133, 734

Bruzual, G., & Charlot, S. 2003, , 344, 1000

Burke, C. J., Shen, Y., Liu, X., et al. 2023, , 518, 1880

Carlsten, S. G., Greene, J. E., Beaton, R. L., & Greco, J. P. 2021, arXiv e-prints, arXiv:2105.03440

Colbert, E. J. M., Heckman, T. M., Ptak, A. F., Strickland, D. K., & Weaver, K. A. 2004, , 602, 231

Conselice, C. J., Yang, C., & Bluck, A. F. L. 2009, , 394, 1956

de Vaucouleurs, G. 1948, Annales d'Astrophysique, 11, 247

den Brok, M., Peletier, R. F., Seth, A., et al. 2014, , 445, 2385

Dewangan, G. C., Mathur, S., Griffiths, R. E., & Rao, A. R. 2008, , 689, 762

Dickey, C. M., Geha, M., Wetzel, A., & El-Badry, K. 2019, , 884, 180

Dickey, J. M., & Lockman, F. J. 1990, , 28, 215

Duras, F., Bongiorno, A., Ricci, F., et al. 2020, , 636, A73

Evans, I. N., Primini, F. A., Glotfelty, K. J., et al. 2010, , 189, 37

Filippenko, A. V., & Ho, L. C. 2003, The Astrophysical Journal, 588, doi:10.1086/375361

Fisher, D. B., & Drory, N. 2008, in Astronomical Society of the Pacific Conference Series, Vol. 396, Formation and Evolution of Galaxy Disks, ed. J. G. Funes & E. M. Corsini, 309

Fruscione, A., McDowell, J. C., Allen, G. E., et al. 2006, in Society of Photo-Optical Instrumentation Engineers (SPIE) Conference Series, Vol. 6270, Society of Photo-Optical Instrumentation Engineers (SPIE) Conference Series, ed. D. R. Silva & R. E. Doxsey, 62701V

Geha, M., Blanton, M. R., Yan, R., & Tinker, J. L. 2012, , 757, 85

Geha, M., Guhathakurta, P., & van der Marel, R. P. 2002, , 124, 3073

Gehrels, N. 1986, , 303, 336

Georgiev, I. Y., Hilker, M., Puzia, T. H., Goudfrooij, P., & Baumgardt, H. 2009, Monthly Notices of the Royal Astronomical Society, 396, 1075

Ghez, A. M., Salim, S., Weinberg, N. N., et al. 2008, , 689, 1044

Graham, A. W., & Guzmán, R. 2003, , 125, 2936

Greene, J. E. 2012, Nature Communications, 3, 1304 EP , review Article

Greene, J. E., & Ho, L. C. 2005, , 630, 122

—. 2007, , 670, 92

Greene, J. E., Strader, J., & Ho, L. C. 2019, arXiv e-prints, arXiv:1911.09678

Greene, J. E., Strader, J., & Ho, L. C. 2020, Annual Review of Astronomy and Astrophysics, 58, 257

Grimm, H. J., Gilfanov, M., & Sunyaev, R. 2003, , 339, 793

Groves, B. A., Heckman, T. M., & Kauffmann, G. 2006, , 371, 1559

Habouzit, M., Volonteri, M., & Dubois, Y. 2017, , 468, 3935

Hao, C.-N., Kennicutt, R. C., Johnson, B. D., et al. 2011, , 741, 124

Ho, L. C. 2008, , 46, 475

—. 2009, , 699, 626

Hong, J., van den Berg, M., Schlegel, E. M., et al. 2005, , 635, 907

Hopkins, P. F., Hernquist, L., Cox, T. J., & Kereš, D. 2008, , 175, 356

Inayoshi, K., Visbal, E., & Haiman, Z. 2020, , 58, 27

Jarrett, T. H., Masci, F., Tsai, C. W., et al. 2013, , 145, 6

Jiang, Y.-F., Greene, J. E., Ho, L. C., Xiao, T., & Barth, A. J. 2011, , 742, 68

Karachentsev, I. D., Makarov, D. I., & Kaisina, E. I. 2013, , 145, 101

Kauffmann, G., Heckman, T. M., Tremonti, C., et al. 2003, Monthly Notices of the Royal Astronomical Society, 346, 1055

Kelvin, L. S., Driver, S. P., Robotham, A. S. G., et al. 2012, , 421, 1007

Kennicutt, R. C., & Evans, N. J. 2012, , 50, 531

Kewley, L. J., Dopita, M. A., Sutherland, R. S., Heisler, C. A., & Trevena, J. 2001, , 556, 121

Kewley, L. J., Groves, B., Kauffmann, G., & Heckman, T. 2006, Monthly Notices of the Royal Astronomical Society, 372, 961

Kimbrell, S. J., Reines, A. E., Schutte, Z., Greene, J. E., & Geha, M. 2021, , 911, 134

Kimbro, E., Reines, A. E., Molina, M., Deller, A. T., & Stern, D. 2021, , 912, 89

Kormendy, J. 2015, in Lessons from the Local Group: A Conference in honor of David Block and Bruce Elmegreen, 323

Kormendy, J., & Ho, L. C. 2013, , 51, 511

Kormendy, J., & Kennicutt, Jr., R. C. 2004, , 42, 603

Kormendy, J., & Richstone, D. 1995, , 33, 581

Latimer, L. J., Reines, A. E., Hainline, K. N., Greene, J. E., & Stern, D. 2021, , 914, 133

Latimer, L. J., Reines, A. E., Plotkin, R. M., Russell, T. D., & Condon, J. J. 2019, , 884, 78

Lawrence, A., Warren, S. J., Almaini, O., et al. 2007, , 379, 1599

Lehmer, B. D., Alexander, D. M., Bauer, F. E., et al. 2010, , 724, 559

Leitherer, C., Schaerer, D., Goldader, J. D., et al. 1999, , 123, 3

Lemons, S. M., Reines, A. E., Plotkin, R. M., Gallo, E., & Greene, J. E. 2015, , 805, 12

Lira, P., Lawrence, A., O'Brien, P., et al. 1999, , 305, 109

Loeb, A., & Rasio, F. A. 1994, , 432, 52

Madau, P., & Rees, M. J. 2001, , 551, L27

Massey, F. J. 1951, Journal of the American Statistical Association, 46, 68

McConnachie, A. W. 2012, , 144, 4

Mićić, M., Holmes, O. J., Wells, B. N., & Irwin, J. A. 2023, , 944, 160

Miller, B. P., Gallo, E., Greene, J. E., et al. 2015, , 799, 98

Mineo, S., Gilfanov, M., & Sunyaev, R. 2012, , 419, 2095

Moran, E. C., Eracleous, M., Leighly, K. M., et al. 2005, The Astronomical Journal, 129, 2108

Moran, E. C., Filippenko, A. V., & Chornock, R. 2002, , 579, L71

Mortlock, D. J., Warren, S. J., Venemans, B. P., et al. 2011, , 474, 616

Neumayer, N., Seth, A., & Böker, T. 2020, , 28, 4

Nguyen, D. D., Seth, A. C., Neumayer, N., et al. 2019, The Astrophysical Journal, 872, 104

Oh, S., Greene, J. E., & Lackner, C. N. 2017, , 836, 115

Ordenes-Briceño, Y., Puzia, T. H., Eigenthaler, P., et al. 2018, , 860, 4

Paudel, S., Smith, R., Yoon, S. J., Calderón-Castillo, P., & Duc, P.-A. 2018, , 237, 36

Peng, C. Y., Ho, L. C., Impey, C. D., & Rix, H.-W. 2010, , 139, 2097

Pfeifle, R. W., Satyapal, S., Secrest, N. J., et al. 2019, , 875, 117

Reines, A. E. 2022, Nature Astronomy, 6, 26

Reines, A. E., & Comastri, A. 2016, Publications of the Astronomical Society of Australia, 33, e054

Reines, A. E., Condon, J. J., Darling, J., & Greene, J. E. 2020, , 888, 36

Reines, A. E., Greene, J. E., & Geha, M. 2013, , 775, 116

Reines, A. E., Plotkin, R. M., Russell, T. D., et al. 2014, , 787, L30

Reines, A. E., Sivakoff, G. R., Johnson, K. E., & Brogan, C. L. 2011, , 470, 66

Reines, A. E., & Volonteri, M. 2015, , 813, 82

Ricarte, A., & Natarajan, P. 2018, , 481, 3278

Riffel, R. A. 2020, , 494, 2004

Rong, Y., Dong, X.-Y., Puzia, T. H., et al. 2020, , 899, 78

Sánchez-Janssen, R., Côté, P., Ferrarese, L., et al. 2019, , 878, 18

Satyapal, S., Böker, T., Mcalpine, W., et al. 2009, , 704, 439

Schutte, Z., Reines, A. E., & Greene, J. E. 2019, , 887, 245

Sérsic, J. L. 1963, Boletin de la Asociacion Argentina de Astronomia La Plata Argentina, 6, 41

Seth, A., Agüeros, M., Lee, D., & Basu-Zych, A. 2008, , 678, 116

She, R., Ho, L. C., & Feng, H. 2017, , 842, 131

Shlosman, I., Frank, J., & Begelman, M. C. 1989, Nature, 338, 45

Stierwalt, S., Besla, G., Patton, D., et al. 2015, , 805, 2

van der Marel, R. P., Alves, D. R., Hardy, E., & Suntzeff, N. B. 2002, , 124, 2639

Vanden Berk, D. E., Richards, G. T., Bauer, A., et al. 2001, , 122, 549

Vaughan, S., Iwasawa, K., Fabian, A. C., & Hayashida, K. 2005, Monthly Notices of the Royal Astronomical Society, 356, 524

Vito, F., Brandt, W. N., Yang, G., et al. 2017, Monthly Notices of the Royal Astronomical Society, 473, 2378

Volonteri, M. 2010, The Astronomy and Astrophysics Review, 18, 279

Volonteri, M. 2012, Science, 337, 544

Volonteri, M., Habouzit, M., & Colpi, M. 2021, Nature Reviews Physics, 3, 732

Volonteri, M., Lodato, G., & Natarajan, P. 2008, , 383, 1079

Volonteri, M., & Reines, A. E. 2016, , 820, L6

Yang, H., Malhotra, S., Rhoads, J. E., & Wang, J. 2017, , 847, 38

York, D. G., Adelman, J., Anderson, John E., J., et al. 2000, , 120, 1579

Zakamska, N. L., Schmidt, G. D., Smith, P. S., et al. 2005, , 129, 1212